A NUMERICAL APPROACH FOR PREDICTING HEMODYNAMIC CHARACTERISTICS OF 3D AORTA GEOMETRY UNDER PULSATILE TURBULENT BLOOD FLOW CONDITIONS USING FLUID-STRUCTURE INTERACTION

by

Ahmet Saat

B.S., Naval Architecture and Marine Engineering, Istanbul Technical University, 2016

Submitted to the Institute for Graduate Studies in
Science and Engineering in partial fulfillment of
the requirements for the degree of
Master of Science

Graduate Program in Mechanical Engineering
Boğaziçi University
2022

This thesis is dedicated to my father Hüseyin Saat..

ACKNOWLEDGEMENTS

Firstly, i would like to express my sincere gratitude to my thesis supervisor, Prof. Kunt Atalık for his support, motivation, willingness to help and kind patience to increase my academic development and scientific vision.

Then, i should appreciate my family. This thesis study could not have been completed without their endless support and encouragement. Especially i would like to thank my mother and my twins Haktan and Hakan during this journey.

I feel so lucky to have great friends through all my life. Specially i would like to thank Onur, Batuhan, Can, Gizem, Ali, Tanju, Abdullah, Canberk, Coşkun Bilgi and Emre Ak for their precious helps, efforts and encouragements from my graduate interview to thesis defence. I would also like to show my appreciation to both my managers and teammates who i worked with, at FİGES and TEI for their supports.

Once and for all, it is impossible to put my gratitude thanks into words for my dear love, Hazal. I am pretty fortunate for all of her understanding, patience, wholehearted support and love. This thesis would not have been possible without her.

ABSTRACT

A NUMERICAL APPROACH FOR PREDICTING HEMODYNAMIC CHARACTERISTICS OF 3D AORTA GEOMETRY UNDER PULSATILE TURBULENT BLOOD FLOW CONDITIONS USING FLUID-STRUCTURE INTERACTION

Cardiovascular diseases are the leading cause of death all around the world and harm the society in terms of economically, socially, and psychologically. Hence diagnosing cardiovascular diseases as early as possible has become vital circumstance. Since clinicians need reliable and fast numerical approaches for their urgent pre-surgery decisions, individualised risk prediction and virtual treatment planning, CFD has become widespread in biomedical especially in cardiovascular medicine. The main aim of current study is to provide insight to hemodynamic characteristics of 3-D aorta geometry with pulsatile turbulent blood flow. In line with this purpose, blood and vessel mechanism has been evaluated through numerical fluid-structure interaction (FSI) analysis that couples computational fluid dynamics (CFD) and finite element analysis (FEA). Besides, effects of turbulence modelling, viscous effects and solid domain parameters such as artery thickness, elastic modulus and Poisson's ratio on hemodynamic characteristics have been investigated. The investigations are carried out by using twelve turbulence models, two Non-Newtonian models and different solid domain values to compare output parameters such as oscillatory shear index, velocity field characteristics, von-Mises stress and displacement. Results have shown that SST k-omega with low-Re corrections model seem to be better capable of predicting hemodynamic characteristics. Proposed computational model can be considered as an initial work for the digital twin of cardiovascular system which is described as the realistic virtual model.

ÖZET

SIVI-YAPI ETKİLEŞİMİNİ KULLANARAK PULSATİL TÜRBÜLANSLI KAN AKIŞI KOŞULLARINDA 3B AORT GEOMETRİSİNİN HEMODİNAMİK KARAKTERİSTİKLERİNİ ÖNGÖRMEK İÇİN SAYISAL BİR YAKLAŞIM

Dünya genelindeki ölüm nedenleri arasında ilk sırada yer alan kardiyovasküler hastalıklar topluma ekonomik, sosyal ve psikolojik olarak ciddi zarar vermektedir. Bu nedenle kardiyovasküler hastalıkların olabildiğince erken teşhis edilmesi hayati bir durum haline gelmiştir. Klinisyenlerin acil bir ameliyat öncesi karar alma, bireyselleştirilmiş risk tahmini ve sanal tedavi planlaması için güvenilir ve hızlı sayısal yaklaşımlara ihtiyaç duyması; biyomedikal alanında -özellikle kardiyovasküler tıpta- HAD uygulamalarının kullanımını yaygınlaştırmıştır. Mevcut çalışmanın temel amacı, pulsatil türbülanslı kan akışı ile 3-D aort geometrisinin hemodinamik özelliklerine dair bilgi sağlamaktır. Bu amaç doğrultusunda, hesaplamalı akışkanlar dinamiği (CFD) ve sonlu elemanlar analizini (FEA) birleştiren sayısal akışkan-yapı etkileşimi (FSI) analizi ile kan ve damar mekanizması değerlendirilmiştir. Ayrıca türbülans, viskoz ve damar modelleme parametrilerinin hemodinamik özelliklere etkisi araştırılmıştır. Araştırmalar, salınımlı kesme indeksi, hız alanı karakteristikleri, von-Mises stresi ve yer değiştirme gibi çıktı parametrelerini karşılaştırmak için on iki türbülans modeli, iki Newtonian olmayan akış modeli ve farklı damar modelleme parametrileri kullanılarak gerçekleştirilmiştir. Sonuçlar, düşük Reynolds düzeltmeli SST k-omega modelinin hemodinamik özellikleri tahmin etmede daha iyi olduğunu göstermiştir. Önerilen hesaplama modeli, gerçekçi sanal model olarak tanımlanan kardiyovasküler sistemin dijital ikizi için bir başlangıç çalışması olarak düşünülebilir.

TABLE OF CONTENTS

LIST OF FIGURES

LIST OF TABLES

LIST OF SYMBOLS

E	Elastic modulus
n_f	Unit normal vector at the surface of the fluid domain
n_s	Unit normal vector at the surface of the solid domain
p	Fluid pressure
Re	Reynolds number
r	Vessel radius
T	Cardiac Cycle
t	Vessel thickness
$\overrightarrow{u}$	Fluid velocity vector
u_f	Fluid displacement vector
u_s	Solid displacement vector
$\ddot{u}_s$	Local blood vessel acceleration
w	Angular velocity
α	Womersly number
δ	Kronocker delta operator
ε	Young's modulus
ϵ_s	Solid component strain tensor
λ_s	First Lam´e coefficient
μ	Kinematic viscosity
μ_{solid}	Lam´e coefficient for the solid
ρ	Density of the blood
ρ_s	Density of the vessel
σ_s	Solid stress tensor
υ	Poisson's ratio

LIST OF ACRONYMS/ABBREVIATIONS

2D	One Dimensional
3D	Two Dimensional
AAA	Abdominal Aortic Aneurysm
CO	Cardiac Output
CFD	Computational Fluid Dynamics
CVDs	Cardiovascular Diseases
DES	Detached Eddy Simulation
DNS	Direct Numerical Simulation
DOF	Degree of Freedom
FSI	Fluid Solid Interaction
FVM	Finite Volume Method
HOLMES	Highly Oscillatory and Low Magnitude Shear
LES	Large Eddy Simulation
MR	Magnetic Resonance
OSI	Oscillatory Shear Index
RANS	Reynolds Averaged Navier Stokes
RBC	Red Blood Cell
SAS	Scale Adaptive Simulation
TAWSS	Time-Averaged Wall Shear Stress
URANS	Unsteady Reynolds Averaged Navier Stokes
WBC	White Blood Cell
WHO	World Health Organization
WSS	Wall Shear Stress

1. INTRODUCTION

1.1. General Background and Motivation

The cardiovascular system, which consists of the heart, arteries, veins, and capillaries, is responsible for the distribution of the oxygen and nutrition to the body tissues, removing carbon dioxide and other wastes from the body and regulating the temperature in the human body. In this circulatory system the heart can be described as the pump providing blood flowing along cardiac cycle [1]. The cardiac cycle involves contraction phase to pump blood through aorta and relaxation phase to pull the blood from the veins [2]. In a healthy adult the human, cardiac cycle repeats itself nearly 75 times per minute, in other words almost 100000 times per day, 35 million times per year. The heart also called as engine of the cardiovascular system weighs about 300 grams and pump 7000 litres of blood per day. Blood is transported throughout the entire body by the vessels which are complex networks of hollow tubes. This blood flow is equal to about 96000 km which is equivalent to about twice the earth's perimeter [3], [4]. Some visuals related to the cardiovascular system and network of the circulatory system are given Figure 1.1 and Figure 1.2, respectively.

Cardiovascular diseases (CVDs) are a group of disorders of the heart and blood vessels which primarily include high blood pressure (hypertension), coronary heart disease (heart attack), cerebrovascular disease (stroke), peripheral vascular disease. CVDs are the most frequent cause of mortality all around the world and causes economic, social, and psychological problems in society [5]. To give an example according to World Health Organization (WHO) approximate 17 million people died from CVDs in 2016 that means about 1 of every 3 in all global mortality. In 2030, almost 22.2 million people will die from CVDs if this tendency continues at this rate [6].

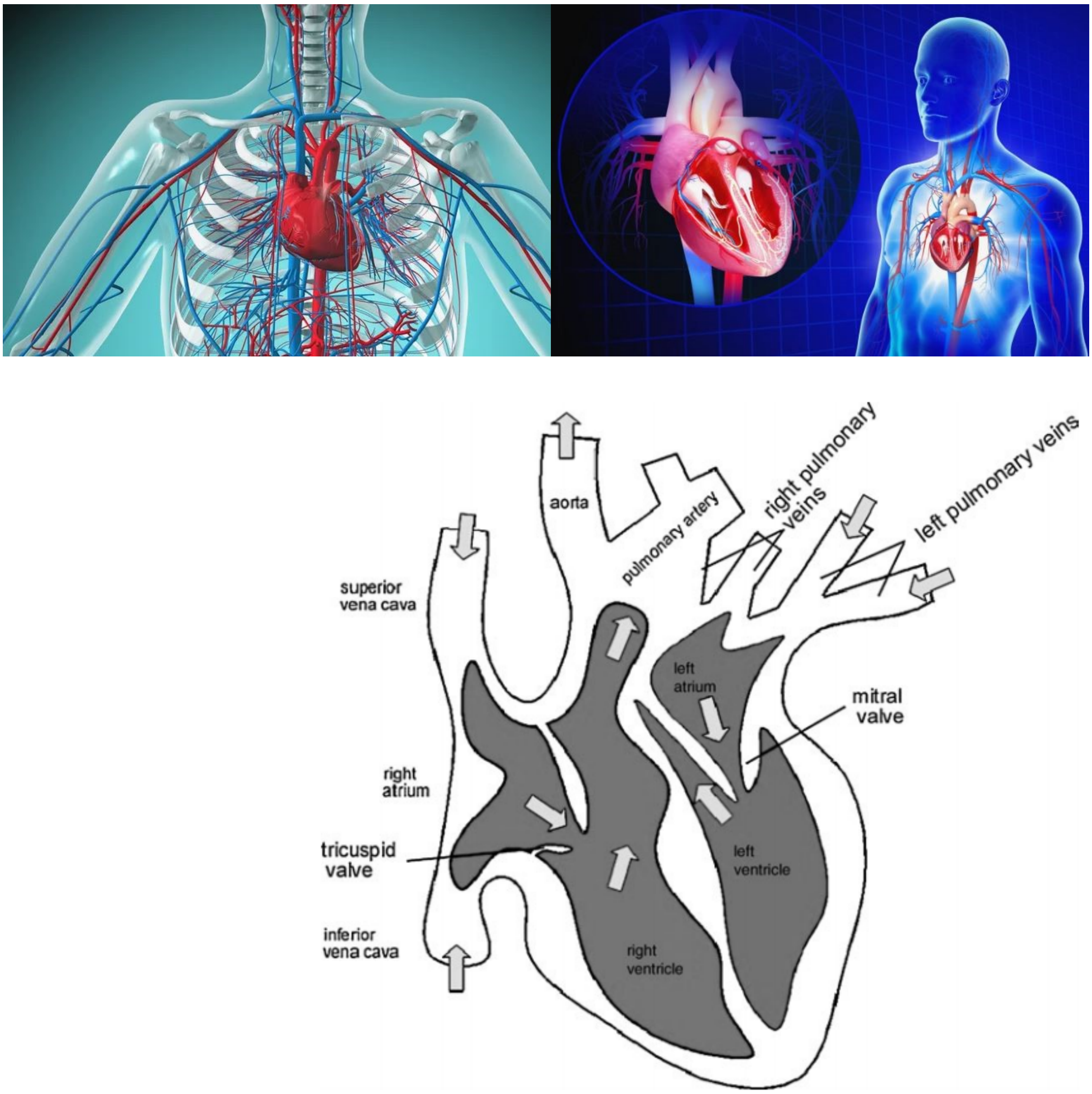

Figure 1.1. Some visuals of the cardiovascular system [1].

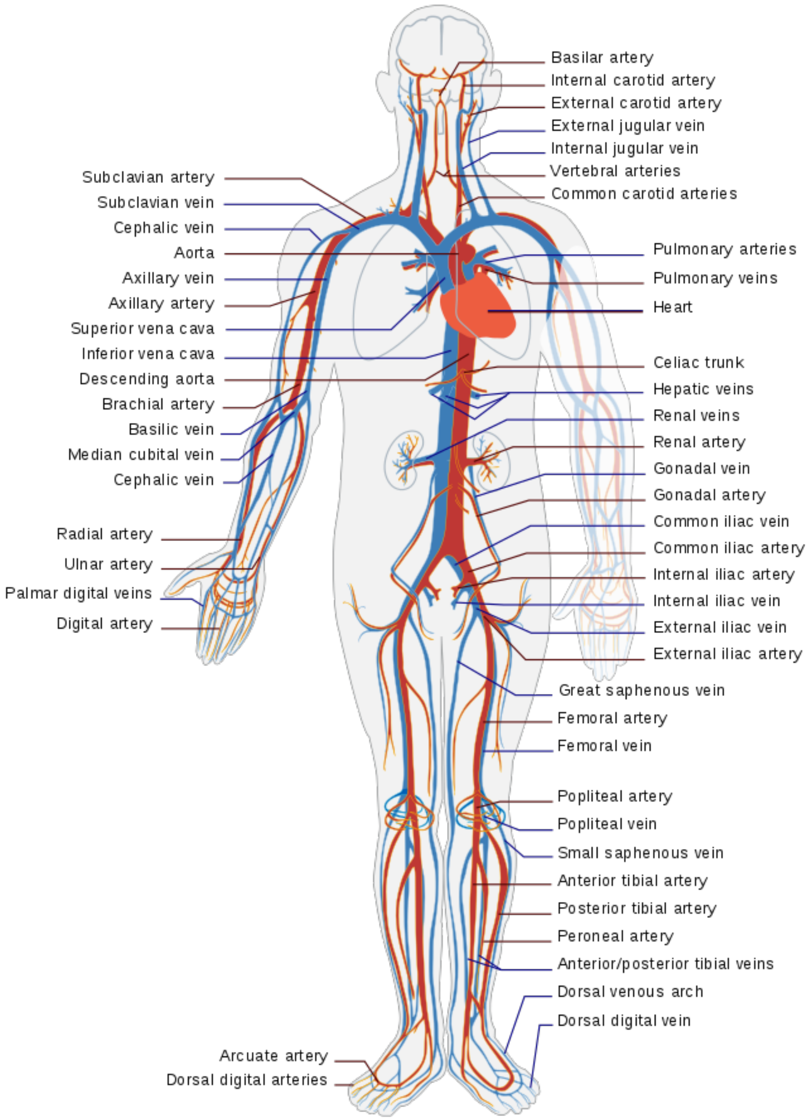

Figure 1.2. The network of the circulatory system [4].

Furthermore, 3.9 million deaths a year, or 45% of all mortality result from CVDs in Europe. Considering the economically, overall CVD is estimated to cost the EU economy €210 billion a year [7]. Besides, CVDs have 14 percent of total health expenditures in 2014-2015 that is more than any major diagnostic group in the USA. If this trend continues, the total direct medical costs of CVD will reach to $749 billion in 2035 [8].

While CVD deaths across the world are given in Figure 1.3; the projected CVD deaths between 2015 and 2030 are given in Figure 1.4. In Figure 1.4; AFR, AMR, EMR, SEAR and WPR represent African Region, American Region, Eastern Mediterranean Region, South-East Asia Region and Western Pacific Region, respectively. Furthermore, ischaemic heart diseases have the highest mortality rate in cardiovascular system for males and females in Europe that illustrated in Figure 1.4. Ischaemic is a condition in which the blood flow (and thus oxygen) is restricted or reduced in a part of the body caused by narrowed heart arteries.

To recognize pathologies or dysfunctions of cardiovascular system it is obvious that discuss the cardiovascular system in detail it becomes a crucial issue for researchers. Considering all of these, cardiovascular medicine study has become quite crucial for world human health for both medical and engineering researchers.

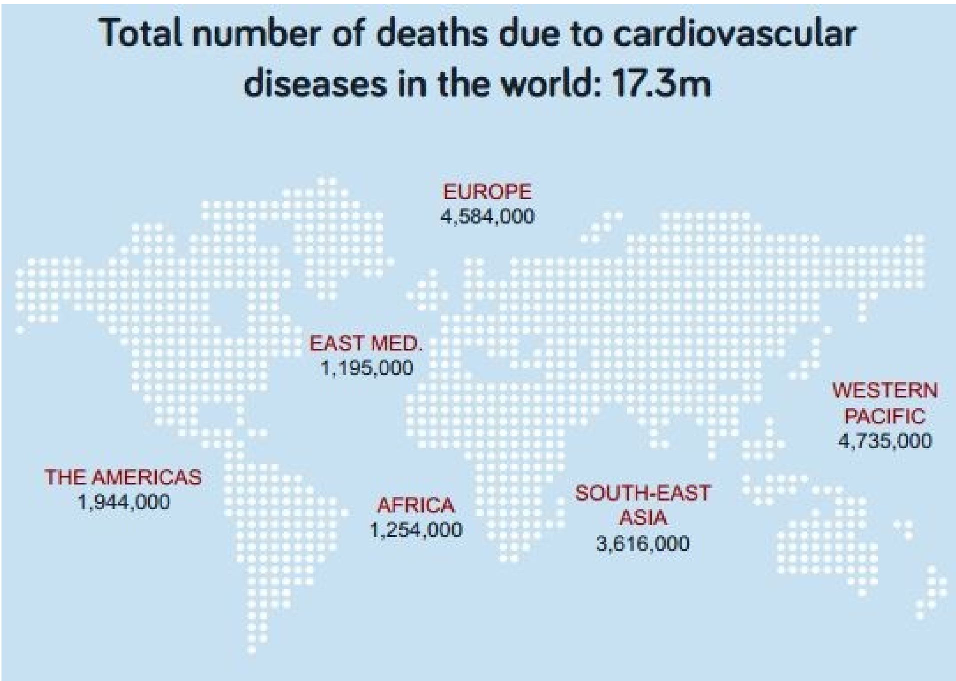

Figure 1.3. CVD deaths across the world [5].

Figure 1.4. Projected CVD deaths 2015-2030 by WHO [6].

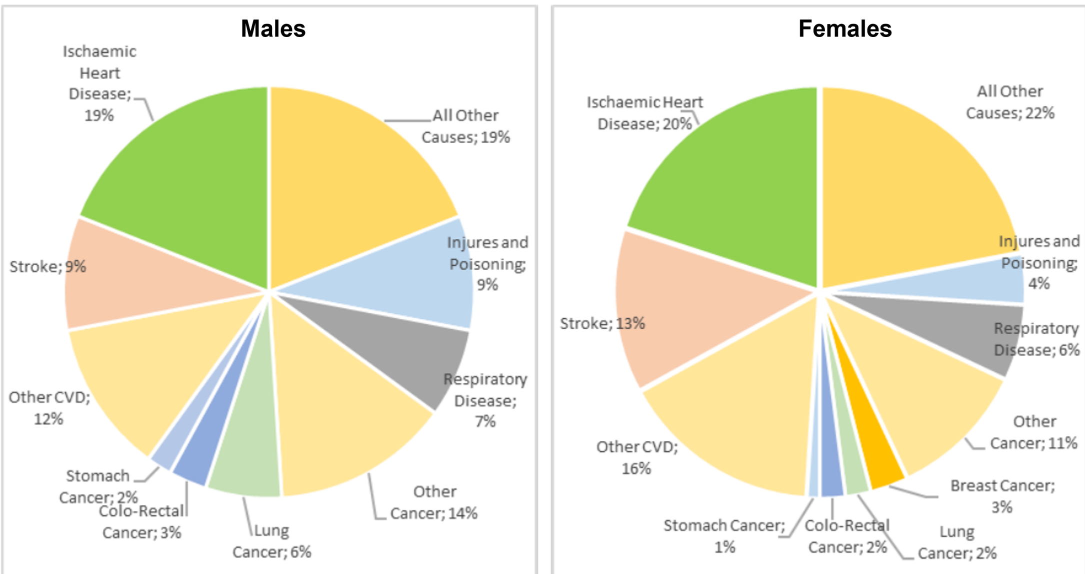

Figure 1.5. Deaths by cause in Europe for males and females [7].

Computational Fluid Dynamics (CFD) is state-of-the-art technology tool which combines mathematics and branch of fluid mechanics where used various range of optimization processes and safety-critical engineering systems mainly including aero-nautical, bio-medical, automotive, watercraft, energy and thermal system. In recent years CFD has become widespread in cardiovascular medicine through providing researchers rapid, economical, and low-risk solutions to research and developed devices such as stents, blood pumps, drug-eluting stents, valve prosthesis, and ventricular assist systems [9]. Furthermore, CFD was effectively carried out for numerous clinical applications, including blood flow studies in major vessels, comparison of rest and exercise conditions, an examination of surgical treatment options [10]. The hybrid model between cardiovascular imaging and CFD analyses give researchers detailed characteristic features of the complex models including physiological pressure, flow fields and wall shear stress which cannot be measured directly [9]. Furthermore, individualised risk prediction and virtual treatment planning can be obtained through patient-specific (individual data) and multi-scale (dimensionless length and time scale) modelling [9]. Therefore, there is a great focus on numerical simulations in biomedical research especially, studying the blood flow in the cardiovascular system to evaluate understanding the hemodynamic phenomena of blood. It can be concluded that CFD application in biomedical is one of the promising research topics with the purpose of the diagnosing and treating the diseases.

1.2. Literature Survey

There is a growing interest, especially on investigating blood flow to obtain phenomena involved cardiovascular diseases. During recent years, numerous valuable studies and investigations were performed. Literature survey was divided into categories to describe physics behind the blood flow efficiently.

1.2.1. General Characteristics of Blood Flow

The blood in the human body is the mixture of about 57 percent plasma components and 43 percent cellular components. Composition of whole human blood with its constituent parts is given in Figure 1.6 [2]. The plasma also called as liquid component of blood is composed of water, protein, and other solutes. The main role of plasma is to take nutrients, hormones, and proteins into the parts of the body. On the other hand, the cellular components also known as solid part of blood consist of the red blood cells

(RBCs) being responsible for carrying oxygen and carbon dioxide and white blood cells (WBCs) being responsible for immune system. In other words, the blood is a complex component where solid and liquid come together in the human anatomy [1].

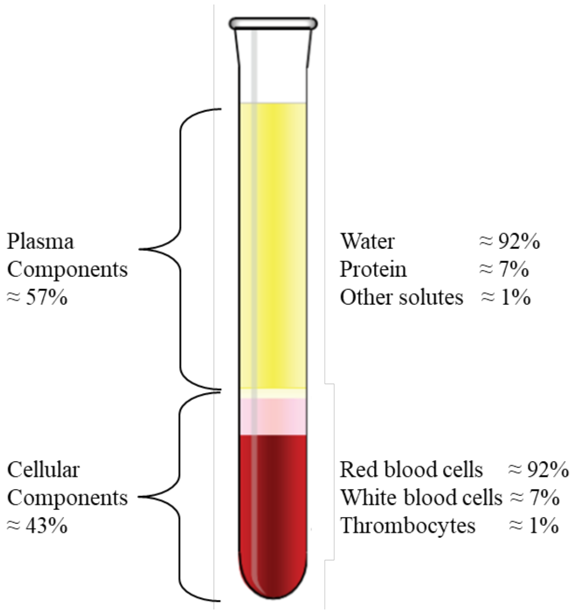

Figure 1.6. Composition of whole human blood [2].

Modelling the blood flow realistically is vital to understand the hemodynamic effects occurring in the circulatory system. To capture and analyse the flow field and the physiological conditions such as flow recirculation, separation, low and oscillating wall shear stress are essential elements of modelling blood flow. As stated previously, the hearth behaves as a pump in the cardiovascular system and causes contractions and relaxations. These contractions and relaxations occur periodic variations in blood flow, which is known as pulsatile flow. The theory of dynamic blood motion in the cardiovascular system embracing changes in the pressure and velocity fields in the circulation system are given in Figure 1.7.

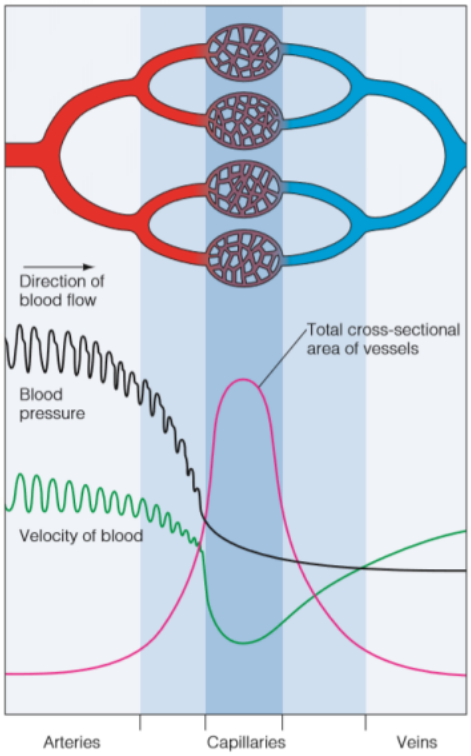

Figure 1.7. Pulsatile blood flow [2].

Indisputably, blood flow has a very complicated flow pattern in humans. Characteristics of blood flow majorly depend on vessel type and pathological conditions of individual which designate characteristics length and velocity. Physical dimensions and velocity parameters in arteries and veins are tabulated in Table 1.1 and Table 1.2, respectively [11]. As it is seen in tables, researchers encounter different blood flow type depending on the type of vessel they are considering. To give an example; generally, in the human body flow is laminar however under conditions of high flow, particularly in the ascending aorta, laminar flow can be disrupted and become turbulent.

Table 1.1. Typical dimensional characteristics of vessels in the human vascular system [10].

Vessel Type	**Internal Diameter [mm]**	**Wall Thickness [mm]**	**Length [mm]**
Ascending aorta	10-24	0.5-0.8	50
Descending aorta	8-18	0.5-0.8	200
Abdominal aorta	5-12	0.4-0.6	150
Femoral artery	2-8	0.2-0.6	100
Carotid artery	2-8	0.2-0.4	100-200
Arteriole	0.01-0.08	0.02	1-2
Capillary	0.004-0.008	0.001	0.2-1
Inferior vena cava	6-15	0.1-0.2	200-400

Table 1.2. Typical flow characteristics of vessels in the human vascular system [10].

Vessel Type	**Peak Velocity [cm/s]**	**Mean Velocity [cm/s]**	**Reynolds number (peak)**	**Pulse Propagation Velocity [cm/s]**
Ascending aorta	20-290	10-40	4500	400-600
Descending aorta	25-250	10-40	3400	400-600
Abdominal aorta	50-60	8-20	1250	700-600
Femoral artery	100-120	10-15	1000	800-1030
Carotid artery	50-150	20-30	-	600-1100
Arteriole	0.5-1	-	0.09	-
Capillary	0.02-0.17	-	0.001	-
Inferior vena cava	15-4	-	700	100-700

1.2.2. Viscous Characteristics of Blood Flow

Studying whether the blood flow behaves as Newtonian fluid or non-Newtonian fluid is one of the crucial researchings. A Newtonian fluid is a fluid in which shear stress and the shearing rate are related by a constant viscosity in other words viscosity does not vary with the shearing rate [1]. Human body temperature, which is the significant factor for viscosity, is almost the same at 37 °C therefore blood viscosity mainly depends on hematocrit, shear rate and vessel diameter. Hematocrit is known as percentage of the red blood cells in the blood in terms of volume. To put it another way, viscous characteristics of the blood flow are mainly related to RBCs volume in blood composition. Shear stress as a function of the rate of shear rate and viscosity as a function of hematocrit for blood flow are given in Figure 1.8. As it is shown in Figure 1.8, blood flow can be modelled as Newtonian fluid in case it flows in tubes which have at least 1 mm diameter and its rates of shearing strain are greater than 100 s^{-1} [1].

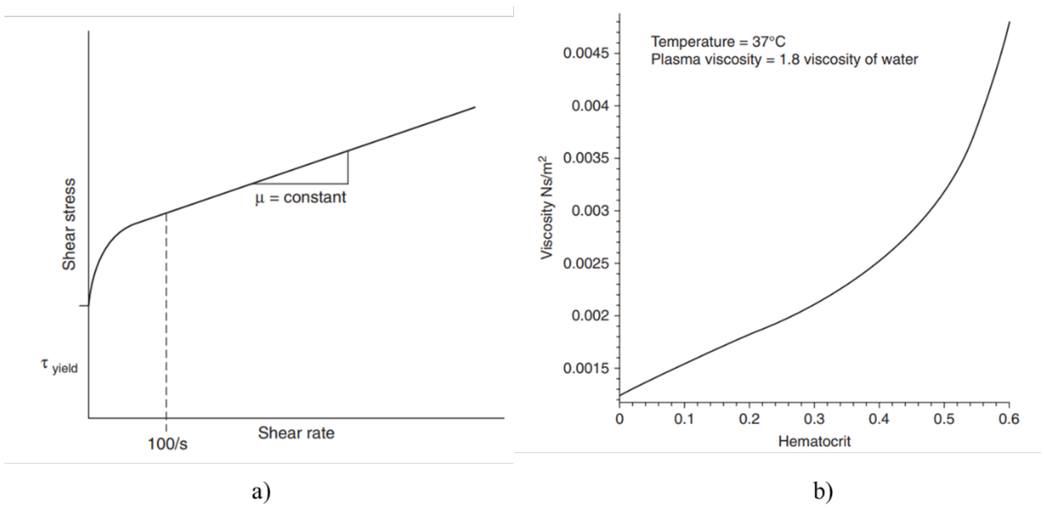

Figure 1.8. The viscosity essentials of the blood flow, (a) Shear stress as a function of the rate of shearing strain (shear rate) for blood, (b) Viscosity as a function of hematocrit for whole blood [1].

Most of the hemodynamic studies blood are assumed to behave as a Newtonian fluid. Perktold et al. [12] seem to be a pioneer of numerical simulation of the non-Newtonian viscosity models for the blood flow. They investigated pulsatile non-

Newtonian blood flow with Casson's relation based on measured dynamic viscosity in three-dimensional carotid bifurcation models. They stated that there is a 10 percent difference between non-Newtonian and Newtonian viscosity models in terms of shear stress magnitudes. In 1993, Budwig et al. [13] presented results in four abdominal aortic aneurysms model over Reynolds number from 500 to 2600 for Newtonian model assumption. In 1998, Taylor et al. [14] developed numerical model for three-dimensional pulsatile flow in the abdominal aorta with Newtonian viscosity approach. They stated that a Newtonian constitutive model for viscosity is the reasonable approximation for the behaviour of the blood flow in large arteries. Furthermore, Waite and Fine [1], Nichols et al. [15] and Leuprecht et al. [16] highlighted that in relatively larger arteries (diameter bigger than 1mm) the viscosity can be modelled as Newtonian and viscoelastic behaviour can be neglected. Scotti and Finol [17] claimed that diameter that is greater than even 0.5 mm, an assumption of Newtonian flow through the aorta is acceptable because blood viscosity is relatively constant at high rate of shear for aorta. Shahcheraghi et al. [18], Tokuda et al. [19] and Afkari [3] have demonstrated realistic results justifying consideration of a Newtonian fluid in the blood flow simulations for human aortic arch.

1.2.3. Fluid-Solid Interaction

Vessel wall mechanisms have an important role in hemodynamic problems and rigid wall assumption of blood flow in CFD calculations are not a realistic situation. Hemodynamic forces cause large deformation at the viscoelastic vascular walls. Consequently, flow volume will change, and this circumstance affects blood flow characteristics [10]. Furthermore, the rigid-wall assumption overestimates the wall shear stress (WSS) up to 50 percent that causes some qualitative and quantitative differences in comparison with flexible wall [10]. Moreover, interaction between vessel and blood flow provides propagation of pressure wave from the heart to whole body for regulating the blood pressure in the body. Therefore, the blood flow and wall deformation should be considered in a coupled, which called as Fluid-Solid Interaction (FSI) model, to obtain physiologically realistic results. FSI problem is a hybrid model which includes blood as the fluid and vascular wall as the structure.

In 2000, the effect of the FSI have been evaluated for right carotid bifurcation model by Zhao et al. [20]. They obtained quantitative results for influence of the vessel wall motion. Gerbeau et al. [21] have presented a feasible strategy for simulating blood flow in large arteries via considering fluid-structure problem in 2005. They explained mathematical theories behind the interaction process in detail. In 2006, Gao et al. [22] studied the complex mechanical interaction between blood flow and wall dynamics in a three-dimensional arch model of an aorta and elaborated computational coupled fluid-structure interaction analysis. Li and Kleinstreue [23] have employed an approved fluid – structure interaction methodology for the coupled blood flow and abdominal aortic aneurysm (AAA) wall dynamics in 2006. They concluded that fluid-structure interaction simulations provide more realistic results to capture blood flow fields and AAA rupture risks. Scotti et al. [17] also stated that FSI simulations predict wall shear stress accurately in 2007. Khanefer et al. [24] found remarkable difference in the structure of flow fields between the flexible and rigid wall for an axisymmetric model of abdominal aneurysm model in 2009. They clearly demonstrated characteristics of the flow field including turbulent kinetic energy and viscous dissipation rate between flexible and rigid wall aneurysm.

1.2.4. Turbulent Characteristics of Blood Flow

Laminar blood flow shows highly organized and smooth characteristics without eddy and swirl. On the other hand, turbulent blood flow is characterized by the disorganized and chaotic property changes. This involves quick change in pressure and flow velocity in space and time. In other words, during laminar flow fluid moves in parallel layers without disruption between the layers while during turbulent flow mixing occurs between the layers creating chaotic flow with variations in gradient [25]. Generally, in the body, blood flow is laminar. However, under conditions of high flow, particularly in the ascending aorta, laminar flow can be discomposed and become turbulent. Turbulent flow also occurs in large arteries at branch points, in diseased and narrowed. Reynolds number, Re $= \rho$.U.D$/\mu$, determines whether the blood flow is laminar or turbulent. It was reported by Reynolds himself that values of Re less than 2000 state will be laminar, whereas values greater than 4000 usually will be fully turbulent [26]. The range of $2000 < Re < 4000$ is known as the transition range that is a mixture of laminar and turbulent flow, with turbulence in the centre of the pipe, and laminar flow near the edges [1]. In brief, when Reynolds number exceeds 4000, turbulence becomes crucial phenomena to realistically obtain a numerical approach for blood flow. The turbulent characteristics of the blood flow is illustrated in Figure 1.9.

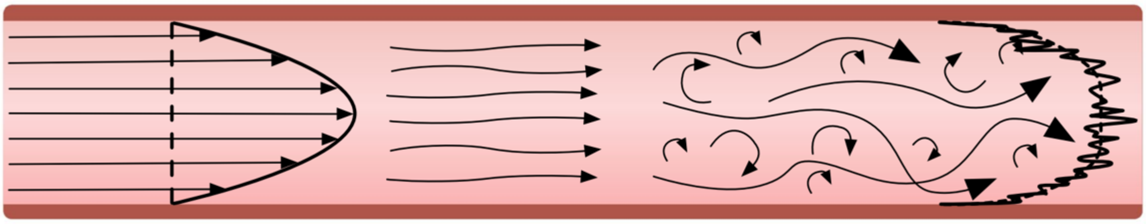

Figure 1.9. The turbulent characteristics of blood flow, (a) Laminar, (b) Transitional, (c) Turbulent [1].

There are several important studies which involve turbulent characteristics of blood flow. Khanafer et al. [27] investigated the influence of the pulsatile turbulent flow on fluid shear stresses and pressure changes under rest and exercise conditions in abdominal aortic aneurysms (AAA). They have found out an increase in turbulence characteristics brings about raised shear stress. The turbulent kinetic energy augments fluid and wall shear stress at the distal aneurysm. Since the fluid shear stress may cause in further dilation and further turbulence, the wall shear stress may give rise to aneurysm growth. They emphasized that turbulence should be considered in numerical models of AAA to better model the dynamics involved in blood flow through aneurysms.

Tan et al. [28] presented flow field and wall shear stress characteristics in thoracic aortic aneurysms using patient-specified data. They compared laminar flow and correlation-based transitional version of Menter's models. They observed high turbulence intensity values in the region outlet of the aneurysms and near the back side of wall that may cause high value of wall shear stress in those regions. They observed that Menter's turbulence models show good agreement than laminar flow simulations according to magnetic-resonance (MR) images. Furthermore, some numerical and experimental studies denoted that a moderate or severe stenosis may lead an increased in vorticity and the possibility of generating turbulence and even with a low percentage of stenosis transient or turbulent flow may occur at a Reynolds number as low as a few hundred [29], [30], [31]. Banks and Bressloff [32] also highlighted that stronger recirculation, higher value of vorticity and negative wall shear stress occur in the flow field in case of the severe stenosis model. Moreover, Jahangiri et al. emphasized that assuming laminar flow will lead to more error than rigid-wall assumption according to their oscillatory shear index for 80 percent stenosis [33]. Recently several valuable studies and investigations were performed about computational turbulence modelling. In some studies (Banks and Bressloff [32], Straatman and Steinman [34], Varghese and Frankel [35] and Xiao and Zhang [36]) it is remarked that transitional k- model provides better agreement with experimental results. Nevertheless, Straatman and Steinman pointed out that while transitional model capture velocity characteristics it was not accurate in predicting turbulence intensity [34]. Both of their studies include Newtonian fluid and rigid-wall assumptions.

1.2.5. Patient-Based Studies

Numerous CFD studies have demonstrated that obtaining the hemodynamic conditions affect the individualised risk prediction and virtual treatment planning. CFD is also used to simulate surgical techniques, which provide for physicians better foresight regarding post-operative flow conditions. With the advance in computational techniques patient-based model has been available. Conti et al. [37] presented patient-specific hemodynamic CFD analysis in the weak form of the governing equations. They compared health model and post-stenting configuration model, which has severe stenosis, for Newtonian blood flow and obtained effect of hemodynamic on endovascular devices. Although their model includes the pulsatile effect, they did not consider deformation of wall by using rigid-wall assumption. In contrast, Mendez et al. [38] and Martino et al. [39] carried out patient-specific computational modelling which include FSI effects for ascending thoracic aortic aneurysm and abdominal aortic aneurysms, respectively. Both of their computational models involve the Newtonian fluid and laminar assumption for blood flow.

1.3. Objective of this Study

As seen in the reviewed studies, there are lots of different concepts that affect the numerical modelling of the blood flow. Therefore, there are lots of interest in this area due to the essentialness of the understanding blood flow characteristics to obtain diagnosing cardiovascular diseases.

The essential objective focuses to describe on the fundamental of physics in blood flow and to identify turbulent and its modelling effect for blood flow which has relatively high Reynolds number. Since blood flow through the aorta is one of the most complex flow situations found in the cardiovascular system, in this study hemodynamic characteristics of the aorta were examined.

In accordance with this purpose, three different validation studies initially carried out that were determined according to related blood flow phenomena. Both study of Budwig et al. [13] and study of Khanafer et al. [40] have been tackled to obtain familiarity for computational modelling of blood flow in case of steady state and laminar flow. To improve turbulence modelling techniques of the blood flow, test case described in study of Stewart et. [41] has been performed. After the validation stages completed; a new methodology about numerical approaches in biomedical for hemodynamic indicator has been primarily put forward. Thus, vessel wall mechanisms through numerical fluid-structure interaction (FSI) analysis that couples computational fluid dynamics (CFD) and finite element analysis (FEA) for 3-D geometry has been tackled. In the first results part, investigations of the turbulence and its modelling in the pulsatile blood flow including FSI for selected 3-D geometry and input parameters have been carried out. In the second part, results of different solid domain parameters have been evaluated. In the last results part, effects of viscous modelling on hemodynamic characteristics are presented.

2. THEORY AND NUMERICAL APPROACH

In this section the model used for the aorta geometry, the formulations describing the fluid and solid domain, as well as the coupling between these domains are explained in detail.

2.1. Aorta Geometry

Modelling the aorta blood flow is the milestone study in terms of computational approach in biomedical engineering. The aorta is the largest artery within the human body that starts as the ascending aorta, turns into the aortic arch, and takes the descending thoracic aorta extending down to the abdominal aorta. In here, the aortic arch is defined as the section of the aorta between the ascending and descending aorta that is shown in Figure 2.1. In literature, there is a huge amount of the aortic arch geometry most of them are based on the patient-specific scan that some of these geometries are illustrated in Figure 2.2.

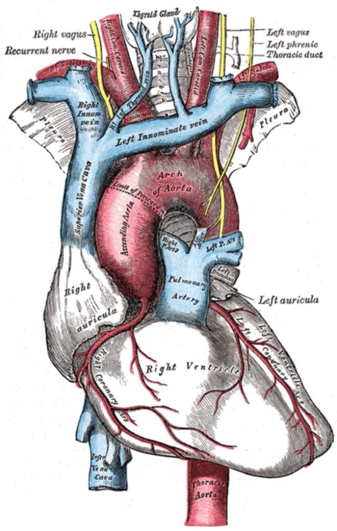

Figure 2.1. The arch of the aorta, and its branches [3].

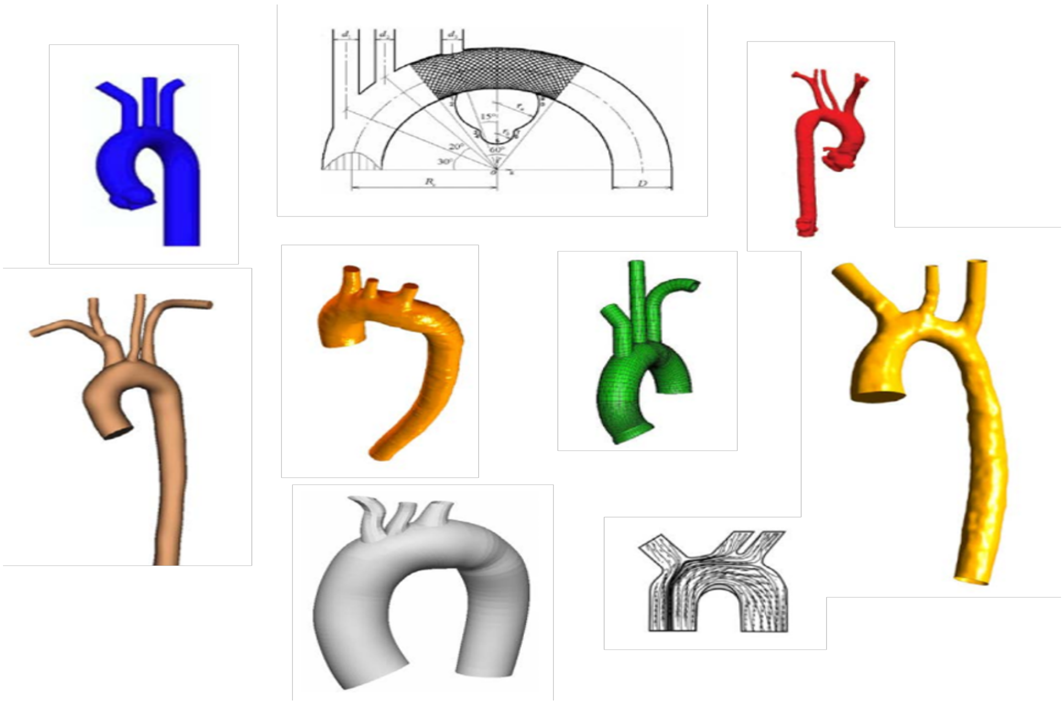

Figure 2.2. Various aorta geometries [3].

Since complex structure of the patient specific aortic arch geometry; determining correct methodology, indicating important parameters for modelling, and establishing digital twin between model and real become quite difficult in computational hemodynamic studies. In order to eliminate these difficulties simplified, idealised and healthy aorta geometry is chosen in this study. The proposed geometry of aorta is given 2.3 whilst its dimensions is detailed in 2.4 [3]. In that geometry, blood flows from ascending aorta to descending aorta including three artery outlets which are brachiocephalic artery, left common carotid artery and left subclavian artery. Whereas ascending and descending aorta have 20 mm diameter; brachiocephalic artery, left common carotid artery and left subclavian artery have 8 mm, 6 mm, and 7 mm diameter, respectively. When we take these into account, they can all be classified as larger arteries [3].

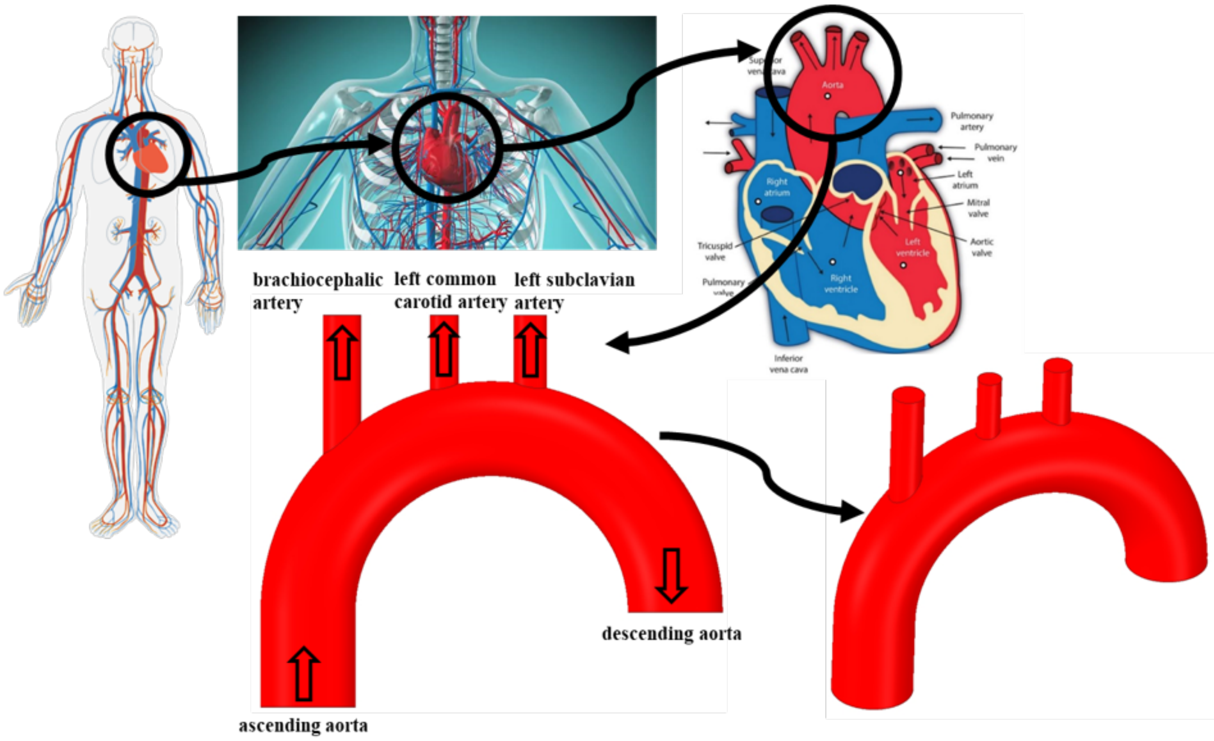

Figure 2.3. The geometry of the modelled aorta [3].

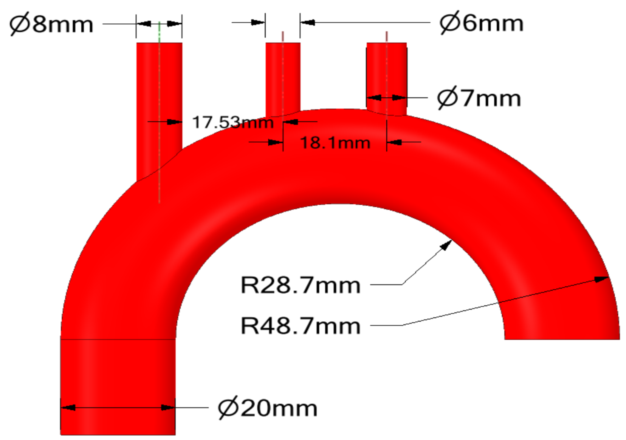

Figure 2.4. The dimensions of the modelled aorta [3].

2.2. Fluid Mechanics

2.2.1. Blood

As mentioned in Chapter 1.2.1. blood flow shows complicated characteristics in hemodynamic. In all analyses the blood flow assumed to be incompressible and turbulent for current proposed geometry flow characteristics. Since current study focalises on the aorta including ascending, descending, and abdominal a Newtonian hypothesis of blood flow may be adequate for realistic calculations. In other words, based on the literature details given in Chapter 1.2.2. blood flow can be modelled as Newtonian fluid in case it flows in tubes which have at least 1 mm diameter and its rates of shearing strain are greater than 100 s^{-1}. Hence, for the proposed geometry and flow characteristics of a constant viscosity and density behaviour have been assigned in the calculations. The dynamic viscosity value of blood flow, μ, is chosen as $\mu = 0.004$ Pa.s, and the density of the blood value, ρ, is chosen as 1000 kg/m^3 throughout the study.

The inlet and outlet characteristics, displayed in Figure 2.5, are imposed during a cardiac cycle for ascending and descending aorta in all calculations. The cardiac cycle of the model is equal to 0.86 s. The waveform of the mass flow or velocity displays the peak at t $\approx$ 0.12 s and trough at t $\approx$ 0.39 s.

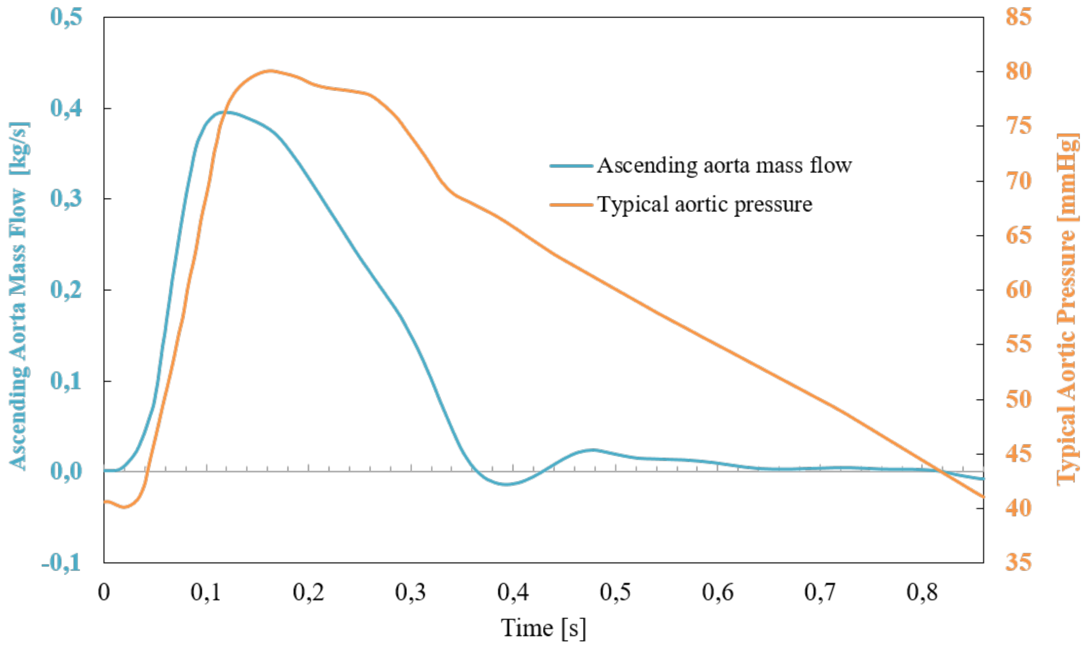

Figure 2.5. In aorta averaged mass flow and pressure conditions during a cardiac cycle.

2.2.2. The Navier-Stokes Equations

The Navier-Stokes equations, developed by Claude-Louis Navier and George Gabriel Stokes in 1822, are the ones which can be used to determine the velocity vector field and pressure field that applies to a fluid. The Navier-Stokes equations can be derived from the basic conservation and continuity equations applied to properties of fluids. A general form of the Navier-Stokes equation for the Newtonian hypothesis and incompressible assumption of the blood flow [42] is

$$\nabla.\overrightarrow{u} = 0, \tag{2.1}$$

$$\rho[\frac{\partial \overrightarrow{u}}{\partial t} + (\overrightarrow{u}.\nabla)\overrightarrow{u}] = \rho\overrightarrow{g} - \nabla p + \mu\nabla^2\overrightarrow{u} \tag{2.2}$$

where $\overrightarrow{u}$,μ, ρ, g and p symbolise the velocity vector, local dynamic viscosity, density, gravity and pressure, respectively.

2.2.3. Turbulence and Its Modelling

In blood flow under conditions of high flow such as flow in the ascending aorta turbulent flow characteristics can be observed. To explain further; according to Table 2, blood flow shows turbulent characteristics in case of aortic vessels like most flows encountered in engineering practice and in nature are turbulent. Turbulent flows illustrate irregular, chaotic, transient, and unpredictable properties that highly have nonlinearity, vorticity, and diffusivity terms. For the proposed geometry and imposed boundary conditions at the inlet Reynolds number distribution was given in Figure 15. From this graph one can conclude that flow can behave as turbulent flow due to Reynolds number exceeding 4000 during cardiac cycle. Furthermore, branch location for the brachiocephalic artery, left common carotid artery and left subclavian artery can become more critical in terms of turbulent flow. Therefore, it is very important to consider turbulence in the analysis phenomena to realistically obtain a numerical approach for blood flow in this study.

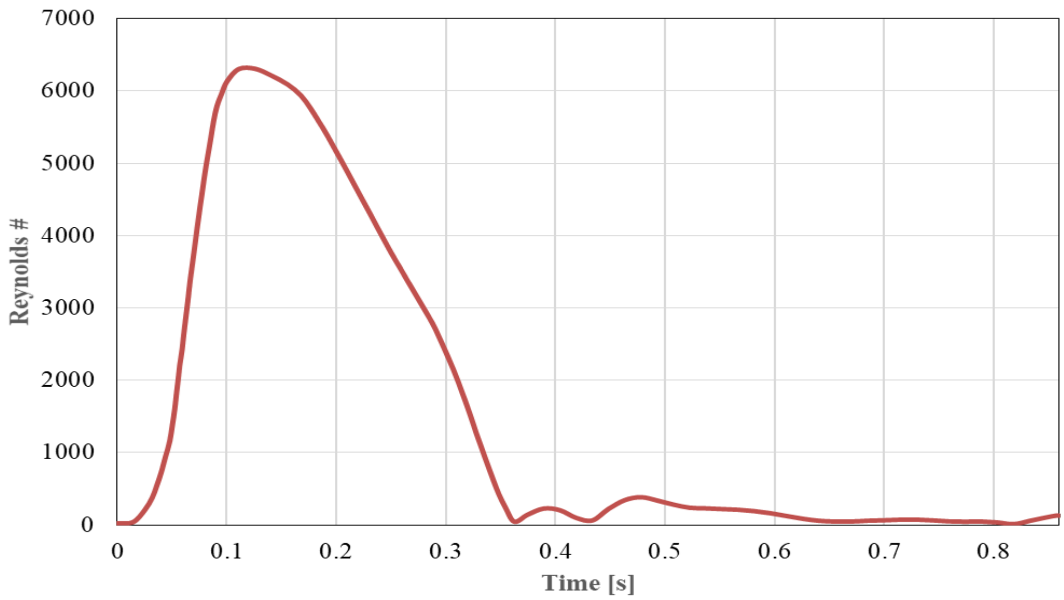

Figure 2.6. Reynolds number distribution for the proposed geometry and the imposed conditions.

Turbulent flow shows unsteady and irregular motion characteristics in which transported quantities (mass, momentum, scalar species) fluctuate in time and space. In here, instantaneous fluctuations are random both in space and time. According to the turbulent energy cascade approach larger eddies transfer energy to smaller eddies via vortex stretching whereas smaller eddies convert kinetic energy into the thermal energy via viscous dissipation [43]. There is a process that larger eddies are continuously forming smaller eddies thereby feeding the smaller eddies energy. Turbulence can be numerically handled by some approaches. Determining true approach is mainly depended on the nature and physics of the problem, and computational cost.

Reynolds averaged Navier Stokes (RANS) technique is carried out to the Navier Stokes equations to transform them into equations for mean flow quantities rather than instantaneous quantities. For the velocity component

$$u_i = \overline{u_i} + u_i^{'} \tag{2.3}$$

equation can be handled where u is the velocity.

Thereafter other quantities are rearranged likewise, and RANS equations are obtained. In case of mean flow quantity is changing with time, the unsteady term will be in the equation and Unsteady Reynolds Averaged Navier Stokes (URANS) are attained as [43]

$$\frac{\partial \rho}{\partial t} + \frac{\partial}{\partial x_i}(\rho u_i) = 0, \tag{2.4}$$

$$\frac{\partial}{\partial t}(\rho u_i) + \frac{\partial}{\partial x_j}(\rho u_i u_j) = -\frac{\partial \rho}{\partial x_i} + \frac{\partial}{\partial x_j}\left[\mu\left(\frac{\partial u_i}{\partial x_j} + \frac{\partial u_j}{\partial x_i} - \frac{2}{3}\delta_i \frac{\partial u_l}{\partial x_l}\right)\right] + \frac{\partial}{\partial x_j}\big(- \rho\overline{u_i' u_j'}\big). \tag{2.5}$$

In here, additional term $-\rho\ \overline{u_i' u_j'}$ known as Reynolds stress tensor that is constituted RANS turbulence modelling, fundamentally.

SAS is an enhanced version of the URANS formulation by adding the von Karman length scale. This approach enables the resolution of the turbulent spectrum in unstable flow conditions. However, for SAS the mesh and time resolution ought to be adequate, otherwise SAS will revert to URANS [43].

The DES approach is the hybrid model including URANS model which is employed in the boundary layer and LES model which is applied to the separated regions. The aim of the DES approach is combining the benefits of RANS and LES while minimizing their disadvantages [43].

In the LES approach, large eddies are resolved directly, whereas small eddies are modelled. Large eddies which are more dependent on the geometry and boundary conditions than small eddies mainly transport momentum, mass, energy, and other scalars. Universal turbulence models are generally stated for small eddies.

In the DNS, the whole spectrum of the turbulent scales is resolved directly without any modelling approach. However, DNS is not feasible in practical engineering problems due to high computational cost. The computational cost is proportional to Re_t^3, where Re_t is the turbulent Reynold number [43]. Illustration of the turbulent modelling approaches is shown in Figure 2.7 [44].

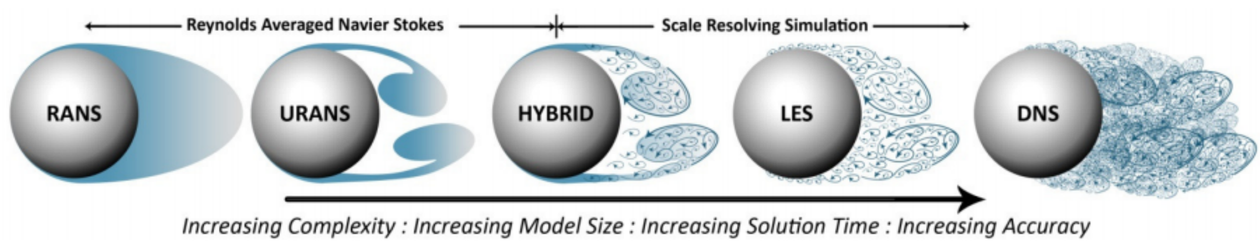

Figure 2.7. Examples of turbulent modelling approaches [44].

2.3. Solid Mechanics

All blood vessels, except for capillaries and venules, are comprised of three main layers: the intima (tunica intima), media (tunica media), and adventitia (tunica adventitia).

- Intima: This is the inner surface of the arterial system that is responsible for absorption and transfusion of the blood ingredients through the arterial walls. A blockage in the blood flow due to the formation of plaque stem from any damage in this layer [3], [45].
- Media: This is the intermediate layer that contains muscle cell, elastic fibres, and collagen. Its main function is the structure strength for arteries [3], [45].
- Adventitia: This is the outer layer of the artery that provides connection between vessels and surrounding tissues. It includes collagen and elastin [3], [45].

It can be said that each layer shows specific biomechanical characteristics such as in the relative thicknesses. The representation for the structure of the artery is shown in Figure 2.8 in detail. As mentioned before elastic and collagen, both are the fibrous protein, are the main components of the vessel. While elastic has linear motion, collagen adds to it nonlinear behaviour. This relation is illustrated in Figure 2.9 [3], [45].

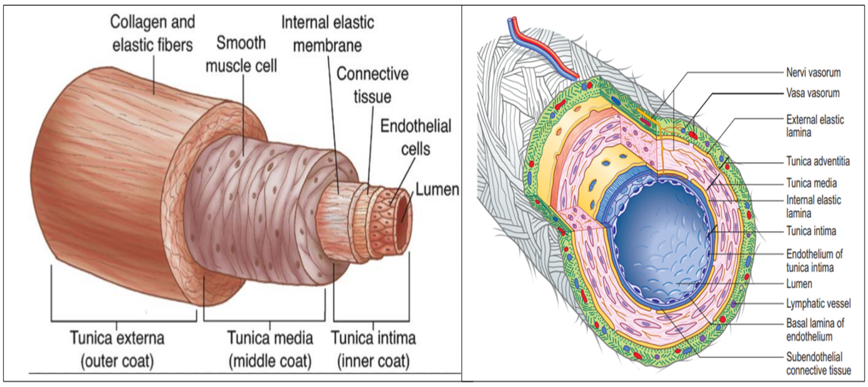

Figure 2.8. General structure of arteries [3,45].

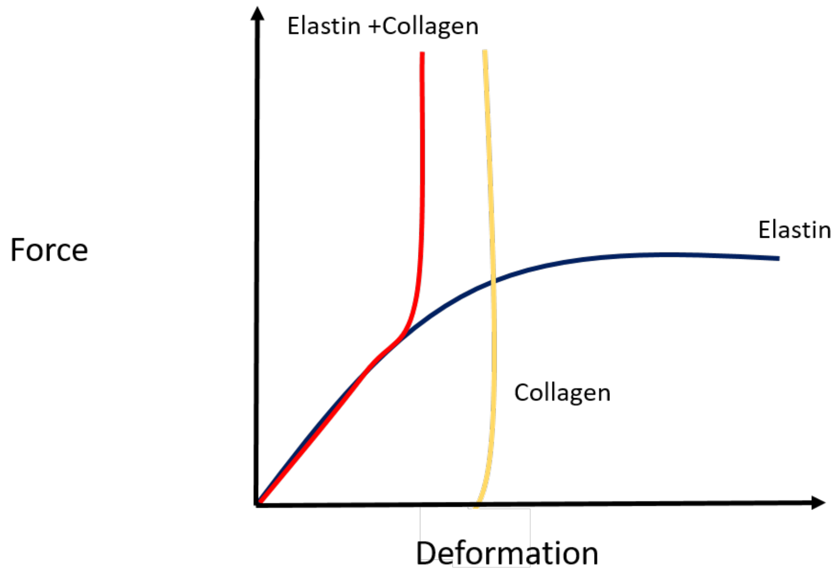

Figure 2.9. Behaviour of elastin and collagen [3,45].

During recent years, numerous valuable studies and investigations were executed about solid mechanics of the vessel. Since blood vessel has three different layer the anisotropic material models have been developed. However single layered, linearly isentropic elastic model has been widely used for the large arteries such as aorta. To give an example Crosetto et al. have modelled aortic wall as a linear elastic structure for FSI simulation of aortic blood flow [46].

The motion of the blood vessel can be expressed via conservation of the momentum equation as

$$\nabla.\sigma_s \ = \rho_s \ddot{u}_s \tag{2.6}$$

where σ_s, ρ_s and $\ddot{u}_s$ are the solid stress tensor, density, and the local blood vessel acceleration, respectively [2]. In this study the artery wall is modelled as elastic and almost incompressible with constant density of ρ_s =1000 kg/m^3. In the linear elastic model, the elasticity of the vessel and the strain rate are the independent of each other. There is an analogy between linearly elastic model approach and Newtonian fluid approach. Similarly, in Newtonian fluid approach fluid viscosity is independent of its shear rate. The solid stress tensor in a linearly elastic model can be written in detail in terms of its tensor and component form as follow, respectively

$$\sigma_s \; = \lambda_s tr(\epsilon_s) I \; + 2\mu_{solid}\epsilon_s. \tag{2.7}$$

In this expression ϵ_s is the solid component strain tensor, λ_s, and μ_{solid} are the Lame coefficients that are calculated by using the material characteristics, Young's modulus, E, and Poisson's ratio, υ. This calculation is described as

$$\mu_{solid} \; = \frac{E}{2(1+\upsilon)}, \tag{2.8}$$

$$\lambda_s \; = \frac{E\upsilon}{(1+\upsilon)(1-2\upsilon)}. \tag{2.9}$$

In this study, while Young's modulus is chosen as 1 Mpa, Poisson's ratio is chosen as 0.49. Furthermore, the solid part of the proposed geometry is given in Figure 2.11. According to data obtained from healthy people, whereas ascending and descending aorta have thickness of 2 mm; brachiocephalic artery, left common carotid artery and left subclavian artery all have thickness of 1.2 mm [3].

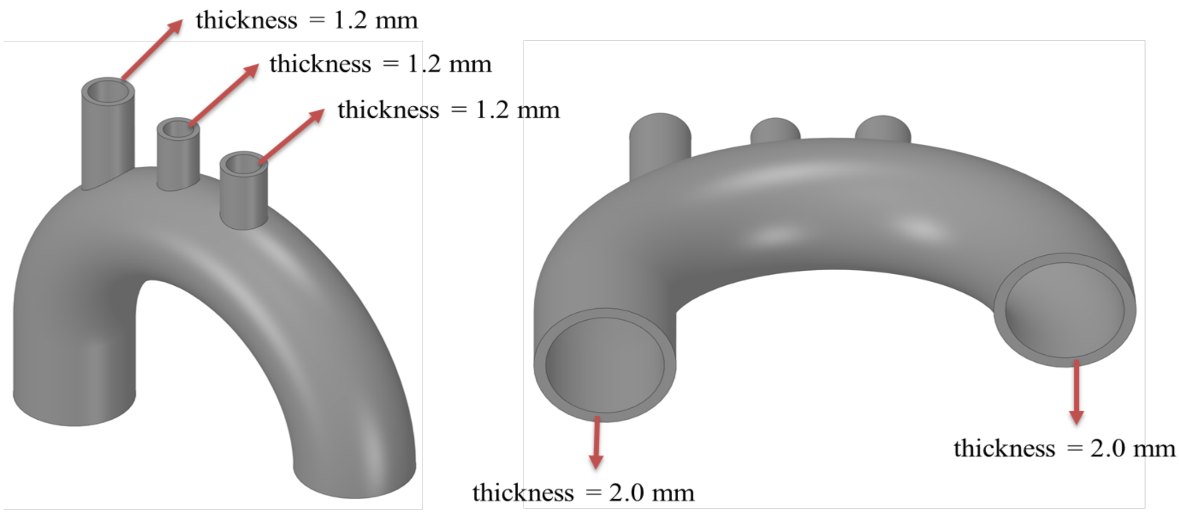

Figure 2.10. Baseline thickness of the modelled aorta.

2.4. Fluid-Solid Interaction

Data exchange of fluid and solid domain at their interface can be the clearest and the most general definition of Fluid-Solid Interaction (FSI) [3]. To reach more realistic hemodynamic characteristics results FSI is used that is coupled Computational Fluid Dynamics (CFD) solutions for fluids and Finite Element Analysis (FEA) solutions for solid. FSI in cardiovascular system is a complicated phenomenon due to required precision and complex biomechanical properties of the vessel interacting with the pulsatile flow [47].

FSI problems in general are quite complex to solve analytically for this reason they must be handled either through numerical approaches that involve the numerical solution of the Navier-Stokes equation with moving boundary conditions and their interactions with structures or experimental studies. In numerical approaches, FEA and CFD solvers exchange force and displacement data between each other. To provide this interchange, a common zone or boundary to be identified and created is required [48]. This field is called as mapping zone in FSI solutions that illustrated in Figure 2.11 [49].

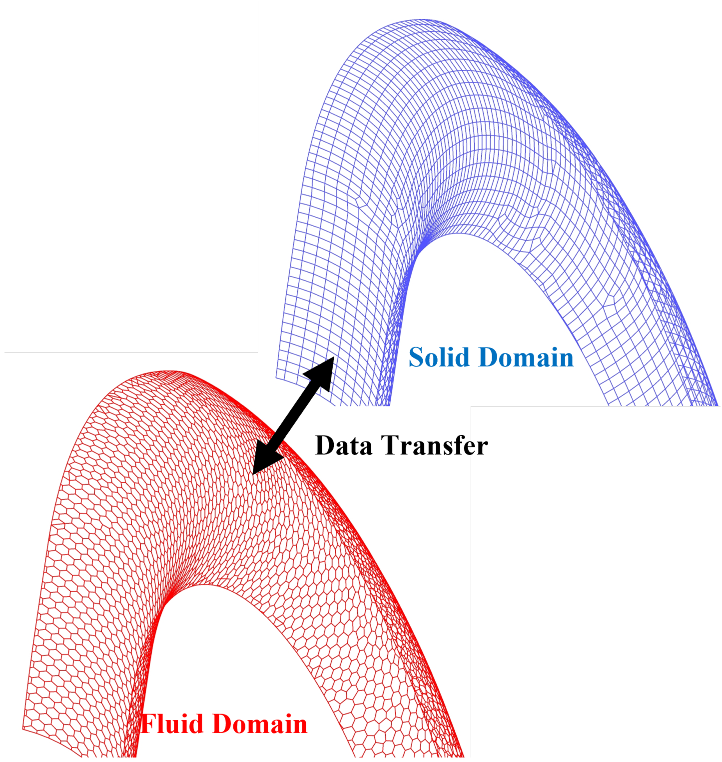

Figure 2.11. Representative fluid and solid domain interface.

CFD tools can solve continuity and momentum in a single matrix in case of coupled solver or separate matrices in case of segregated solver. Other field such as turbulence, heat transfer is solved in a segregated solver. FEA tools usually solves structural field via related equations. Required quantities like force and displacement are transferred between each other by system coupling. Herein iterations can be required to converge the quantities transferred between the CFD and FEA solvers.

The following boundary conditions are applied at the interface of the blood and the vessel to handle coupling between the solid and fluid domains [2]:

$$\overrightarrow{d_f} = \overrightarrow{d_s} \tag{2.10}$$

$$\overrightarrow{u} = \frac{D\overrightarrow{d_s}}{Dt} \tag{2.11}$$

$$\sigma_f.\overrightarrow{n_f} = \sigma_s.\overrightarrow{n_s} \tag{2.12}$$

where $\overrightarrow{d}$ is the displacement vector, $\overrightarrow{u}$ is the fluid velocity vector, $\overrightarrow{n}$ is the unit normal vector at the surface, and the subscripts s and f denote solid and fluid domains, respectively [2].

There are mainly two approaches for the numeric solution of FSI [47]:

- Monolithic approach: the Navier-Stokes equations and the displacement of the structure are solved simultaneously, with a single solver.
- *Partitioned approach:* the Navier-Stokes equations and the displacement of the structure are solved separately, with two distinct solvers.

Furthermore, the partitioned approach can be categorised as one-way FSI and two-way FSI. In one-way FSI a converged solution is obtained for one field, then used as a boundary condition or external load for the second field [43]. On the other hand, in two-way FSI the results of the first model are mapped to the second model and these results are mapped back to the first model [47]. In explicit method, also known as Gauss-Seidel, weak or loose coupling, calculation is performed at a future time from the currently known system status. In implicit method, also known as strong, full weak or iterative coupling, calculation is carried out at a future time from the system statuses at present and future time [47].

2.5. Input and Output Parameters

2.5.1. Input

The Reynolds number represents the relation between the inertial forces and the viscous forces. Additionally, characteristics of the flow whether laminar or turbulent is indicated by the Reynolds number.

Due to the pulsatile inlet waveform conditions, the inlet velocity profile is changing in time. Thereupon, different Reynolds number exists during flow period. In this study a peak Reynolds number calculated from highest velocity of the inlet are determined as critical Reynolds number [50],

$$Re_p = \frac{\rho u_p D}{\mu} \tag{2.13}$$

where u_p is the peak velocity and D is the blood vessel diameter, respectively.

The Womersley number describes the relationship between inertial and viscous force terms. Besides, characteristics of the flow whether pulsatile or oscillatory are indicated by the Womersly number,α [50],

$$\alpha = r\sqrt{\frac{w}{\nu}} = D\sqrt{\frac{\pi\rho}{2\mu T}} \tag{2.14}$$

where r, w, ν and T denotes blood vessel radius, angular frequency, kinematic viscosity and cardiac cycle respectively.

Womersley number is mainly determined by the heart rate because it leans on the frequency or the period of the cardiac cycle.

Length and diameter ratio represent geometrical shape of the aneurysm or vessel to use for simulation. Different patients were investigated to obtain their vessel data using tomographic for many years. [50].

2.5.2. Output

The wall shear stress is the shear stress very close and parallel to the wall and being measure of the tangential stress that the fluid is exerting at the wall (and vice versa) and therefore acts an important parameter in the study of blood flow through arteries [50].

The oscillatory shear index (OSI) represents a numerical parameter for the wall shear stress. It charactarizes the wall shear stress acting in directions in terms of the temporary mean shear stress during pulsatile blood flow [50]. OSI is expressed as,

$$OSI_x = \frac{1}{2}\left(1 - \frac{|\int_0^T \tau_W(x,t)dt|}{\int_0^T |\tau_W(x,t)|dt}\right). \tag{2.15}$$

The turbulent kinetic energy depicts a measure of degree of turbulence and (TKE) can be expressed as the energy associated with turbulent eddies in a fluid flow. It could be defined as the kinetic energy per unit mass related with eddies in turbulent flow [50]. TKE is expressed as,

$$TKE(x,t) = \frac{1}{2}\Big({u_1}'^{\,2}(x,t) \; + {u_2}'^{\,2}(x,t) + {u_3}'^{\,2}(x,t)\Big) \tag{2.16}$$

where u_1, u_2 and u_3 are the velocity components.

3. SOLUTION METHODS

In the current thesis, all the numerical analyses are performed by using the ANSYS Fluent which has finite volume method for fluid domain and the ANSYS Structure which has finite element method for solid domain. This chapters highlights the solution methods, applied boundary conditions and solver settings. The FSI technique, fluid domain solution and solid domain solution are explained in details in the Section 3.1, 3.2, and 3.3 respectively.

3.1. FSI Solutions

All solved equations which were introduced previously are both non-linear and coupled which are handled via FSI method. In fluid domain wall shear stress brings about force related to pressure for the solid model whereas in the solid domain due to the received force deformation is occurred as well as calculated. Since blood flow may significantly apply pressure to blood vessel, remarkable structural deformations can be observed. Besides, this deformation can alter flow domain which known as 2-way interaction. Therefore, based on this basis biomedical applications needs a fully coupled 2-way FSI technique [43].

On this thesis study; whereas system coupling component in ANSYS provides different solvers to be handled to tackle complex multiphysics problem, the FSI technique is given in Figure 3.1 as flowchart data diagram [2, 43, 51].

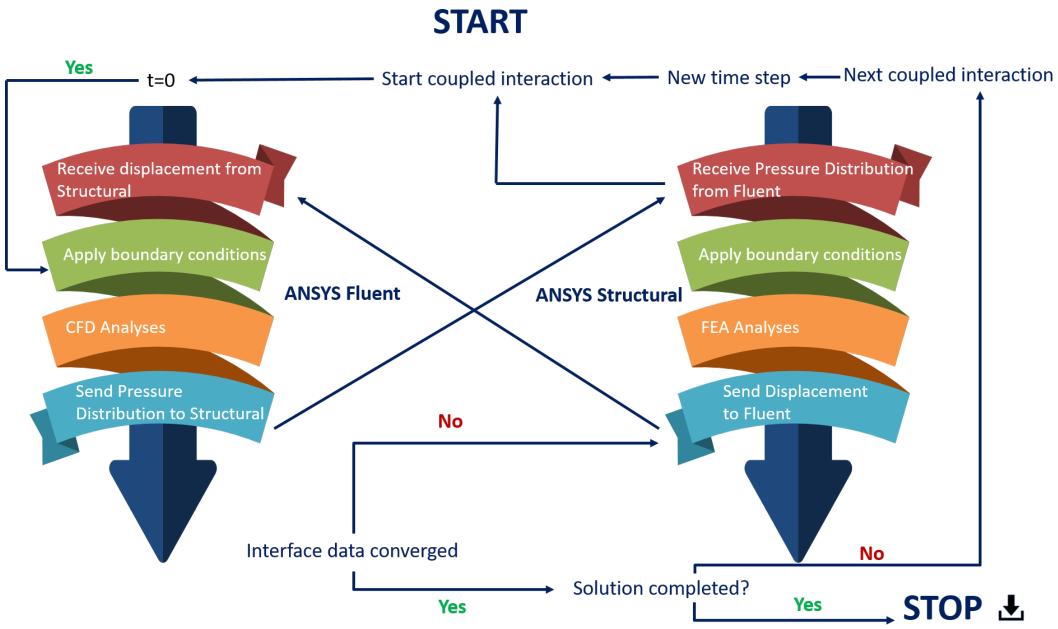

Figure 3.1. FSI technique as flowchart data.

3.2. Fluid Domain Solution

In this thesis study, to understand the hemodynamic characteristics of the blood flow in the arteries, governing conservation equations of mass and momentum were solved computationally. However, due to the complexity of non-linear terms, CFD method is used to solve the governing equations. The basis of almost all CFD involves three issue which are pre-processing (preparing geometry, generating mesh, defining boundary conditions and solver settings), processing (computing solutions, observing convergence criteria) and post (examining results).

During the calculations SpaceClaim was preferred for the drawing and preparing geometry for analyses. To generate mesh Fluent Meshing which is useful for the high-quality polyhedral mesh was chosen. Whilst the CFD computations were performed on the Fluent, CFD-Post was used for the evaluation of the results. All the CFD tools mentioned has been developed by ANSYS.

Finite Volume Method (FVM) that represents and integrates governing equations for solution domain is used in Fluent. Small volume surrounding each mesh is named as finite volume. In this method, integral equations transform into the algebraic equations through divergence approach. Then those algebraic equations are iteratively solved by applying reasonable boundary conditions and approximation techniques [52, 53]. In the FVM, the fluid domain is initially divided into the discrete control volume called as mesh. Afterwards governing equations are integrated for dependent parameters which are unknowns such as velocity, pressure, temperature. Lastly linear equation system is solved iteratively for the revised values of the dependent parameters until converges.

In Fluent there are two available solver type which are pressure-based solver and density-based solver. In both academic and commercial applications, pressure-based solver has been used for low-speed incompressible flow whereas density-based solver has been preferred high-speed compressible flows for many years. Initially, the velocity field has been calculated by using momentum equations in both methods. In the density-based solver, the density field and pressure field are obtained through continuity equation and equation of state, respectively. On the other hand, in the pressure-based solver, the pressure field is acquired through pressure or pressure correction equations thanks to obtained via managing continuity and momentum equations. Despite mesh generation and integrating the governing equations steps are the same for both methods, solving the linear equation system is dissimilar each other. Furthermore, the pressure solver consists of two different algorithms which are segregated and coupled. As the name suggest, the governing equations are solved sequentially to provide converged solution in an iterative loop. In coupled solver a single set of matrixes including momentum and pressure-based continuity equation are jointly solved. Particularly, the momentum and continuity equations are solved in a closed loop that enables better convergence. However, coupled solver has more computational cost in comparison with segregated solver due to its requirement for memory. In this study the governing equations are tackled with pressure-based solver with coupled algorithm [43, 54].

As for the boundary conditions, the blood vessel surface considered as wall that is also data transfer region for FSI calculations. At the inlet, time-dependent mass flow rate of the blood was invoked as a mass-flow inlet boundary condition. In the proposed geometry certain amount of the blood flow passing through in terms of percentage of inlet mass flow descending aorta brachiocephalic artery, left common carotid artery, and left subclavian artery are 80%, 10% 5% and 5%, respectively. Therefore, estimated pressure drop for each outlet show a crucial feature in order to capture intended flow rate. Afkari has executed important study to underline relationship between pressure drop and flow rate for arteries. Based on the data attained from mentioned study, the calculated outlet pressure according to reference pressure was imposed at each boundary. Imposed boundary conditions in this study is illustrated in Figure 3.2

During the CFD analyses, second order discretization scheme was employed for the convective terms of the momentum and turbulence equations. Velocity-pressure coupling was carried by Coupled scheme, whereas Least Square Cell Based method was used for calculation of gradients. Through the numerical calculation, convergence control was controlled via continuity, momentum, and turbulence equations. Since the evaluate effect of the turbulent model on blood flow is one of the important goals of this study different turbulent models have been handled. All details of the present CFD model are given in Table 3.1.

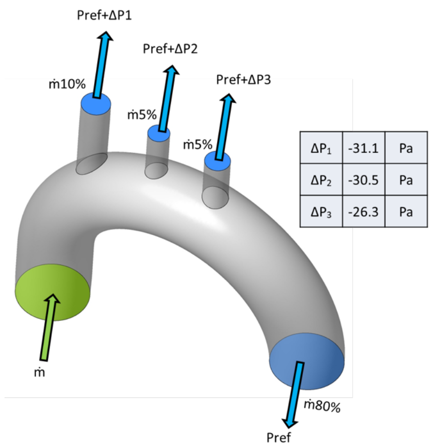

Figure 3.2. The imposed boundary conditions for CFD.

Table 3.1. CFD modelling details.

Parameter	Detail
Solver	Transient, incompressible, system coupling
Blood Density	1000 kg/m3
Blood Viscosity	0.004 kg/ms
Cardiac 0.86	0.86 s
Time-step size	0.005
Pressure-Velocity Coupling	Second Order
Discretization method	Least Square
Discretization order	Second

3.3. Solid Domain Solution

All solid domain solution has been performed in ANSYS Mechanical software through using transient structural analyses. Degrees of freedoms (DOFs) play a fundamental role in the transient analysis solution method. The finite element semi-discrete equation of motion is obtained as follow from the spatial discretization for the principle of virtual work by using finite element method for most structural dynamic problems,

$$[M]\{\ddot{u}(t)\} \ + [C]\{u(t)\} \ + \{F^i(t)\} \ = \{F^a(t)\} \tag{3.1}$$

where $[M]$,[C], $\{\ddot{u}(t)\}$, $\{u(t)\}$, $\{u(t)\}$, $\{F^i(t)\}$ and $\{F^a(t)\}$ are the structural mass matrix, structural damping matrix, nodal acceleration vector, nodal velocity vector, nodal displacement vector, internal load vector and applied load vector, respectively [55].

The standard and well-known three-dimensional element which is Shell181 had been used. The Shell181 is especially effective element for linear, large rotation, and large strain nonlinear applications. Logarithmic strain and true stress measures are the fundamentals for element formulation [56]. And what is more, the Shell181 it supports both full and reduced integration schemes in the element domain. In ANSYS Transient Structural, a direct solver with the Newton-Raphson method is used for solving nonlinear equation that based on the linear approximation technique iteratively [55]. Multiple substeps to ramp the force boundary condition in each time-step lead increased solution time. Therefore, one can concluded that Newton-Raphson approach is enough for efficient convergence [55].

The surface of the aortic inlet was modelled as fixed meaning that model remained stable during inlet pulsatile blood flow conditions. The outer region of the aortic wall was handled as load surface that data come from fluid domain solution. For outlet structure conditions it has been recognized that different boundary conditions have been applied in the other studies. To give an instance, in some studies outlets with branches were fixed in all directions whereas in several studies those outlets were modelled as radially free. Application of the different boundary conditions for numerical modelling is illustrated in Figure 3.3. In this thesis the sensitivity study for the different support types in structural analyses have been performed. This sensitivity study is detailed in Tests and Validations chapter. Based on the result of this study, branch artery outlets brachiocephalic artery, left common carotid artery and left subclavian artery have been extended towards downstream direction as 4 mm, whilst descending aorta has been extended towards downstream direction as 2.5 mm. Then, as can be seen in the Figure 3.2 fixed type supports were imposed to outlets boundaries that restricts any movements in all degrees of freedom. All details of the present FEA model are given in Table 3.2.

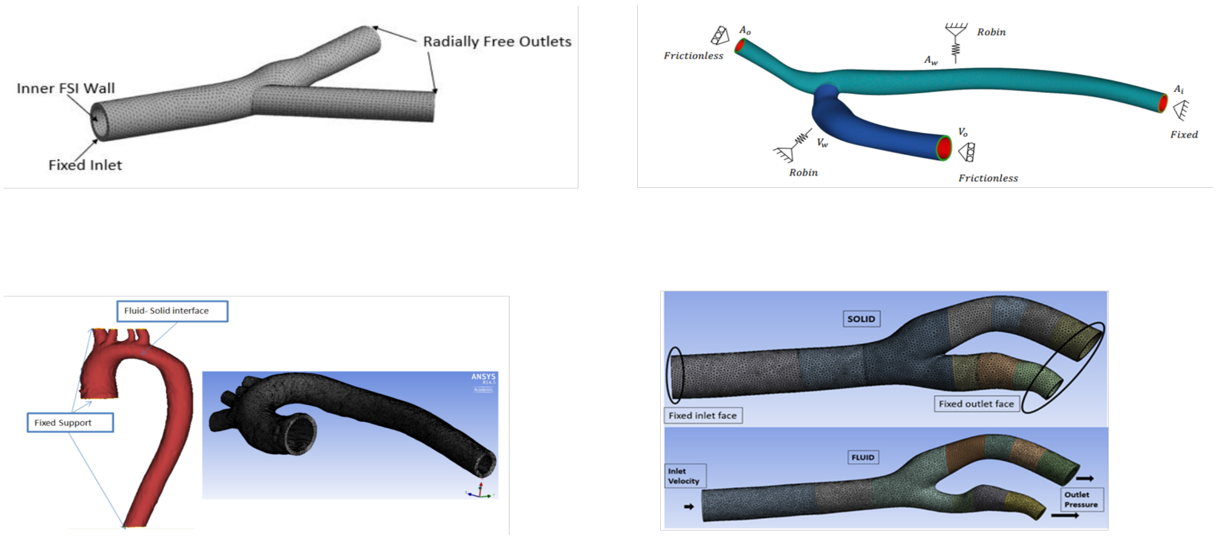

Figure 3.3. The application of the different boundary conditions [49, 51, 57, 58].

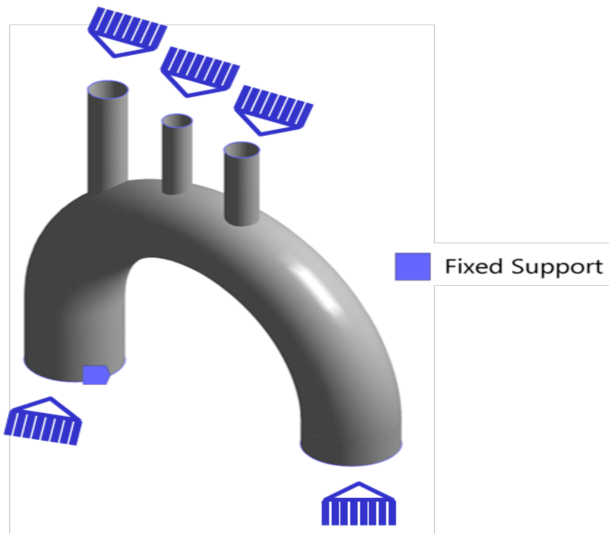

Figure 3.4. The imposed boundary conditions for FEA.

Table 3.2. FEA modelling details.

Parameter	**Detail**
Solver	Transient, system coupling
Artery Density	1000 kg/m^3
Young's modulus	1 MPa
Poisson's ratio	0.49
Bulk Modulus	16.667 MPa
Shear Modulus	0.33557 Mpa
Time-step size	0.005
Large Deflections	On

4. TEST AND VALIDATIONS

In the current thesis, it is aimed to minimize numerical uncertainties. In parallel with this purpose several numerical tests have been employed. Initially generated mesh and mesh dependency study are given in Section 4.1. Afterwards, the cardiac cycle and the time step dependency is mentioned in Section 4.2. Then, the effect of the support type on results for structural dynamics is detailed in Section 4.3. Lastly, benchmark studies have been carried out to compare experimental and numerical results.

4.1. Mesh

In this study, a mesh structure in which both flow and solid domain are dived into small elements to solve numerically related equations was composed of polyhedral elements for fluid domain and hexahedral elements for solid domain. In region where complex flow and solid structured were anticipated such as junction points of artery branches denser mesh algorithms were employed. In order to be able to model boundary layer region a total of 5 layers on inflation cells were formed perpendicular to wall surfaces for fluid solutions. The mesh visuals were illustrated in Figure 4.1 and Figure 4.2 for fluid and solid computational domain, respectively. Moreover, the further quantitative detail of the meshes generated in this study were listed in Table 4.1 for fluid and Table 4.2 for solid. As it can be seen from this table, mesh quality values satisfy software recommendation.

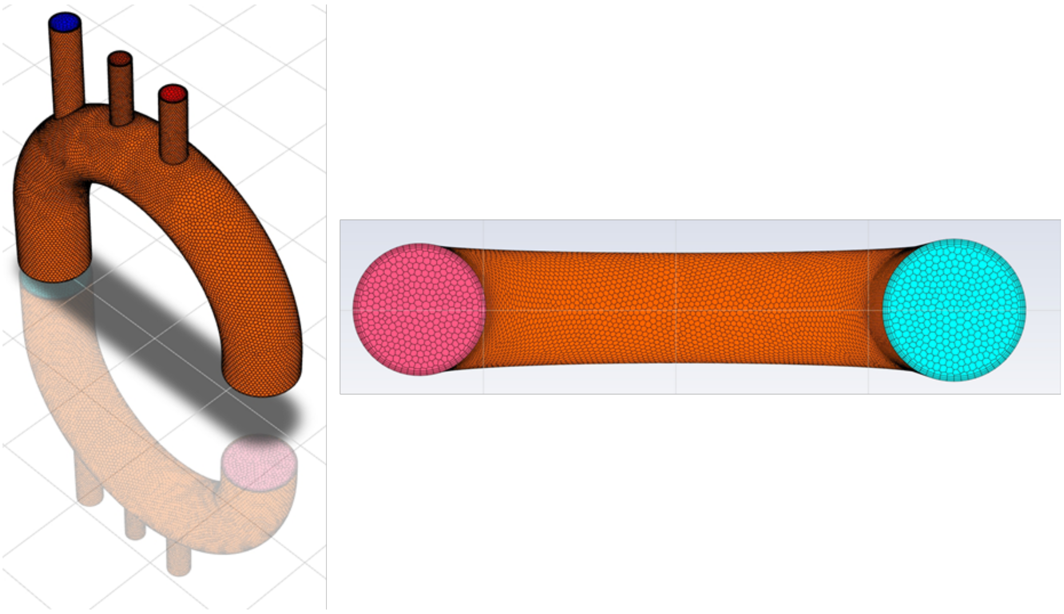

Figure 4.1. Polyhedral mesh of the fluid domain.

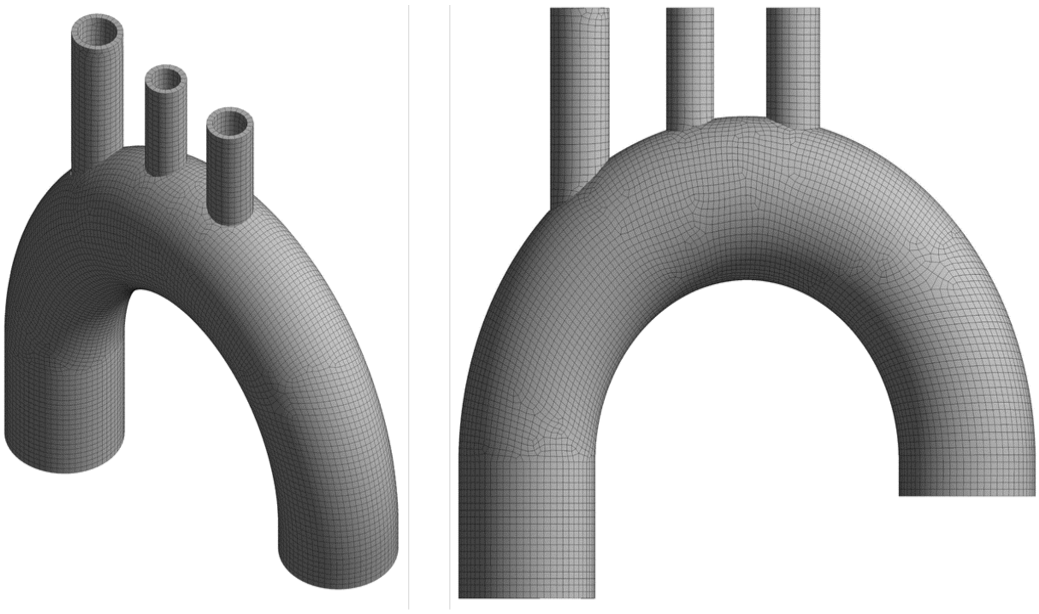

Figure 4.2. Hexahedral mesh of the solid domain.

Table 4.1. Mesh details for fluid domain.

Computational Domain	**Fluid Domain**
Element Type	Polyhedral
Element	104620
Skewness (should be 0.9)	0.75
Orthogonal Quality (should be 0.1)	0.2
Aspect Ratio (should be 35)	17

Table 4.2. Mesh details for solid domain.

Computational Domain	**Solid Domain**
Element Type	Hexahedral
Element	10260
Skewness (should be 30°)	61°
Taper Ratio (should be 0.8)	7
Aspect Ratio (should be 5)	2.11

To eliminate mesh resolution on the results and error in critical system parameters, the sensitivity study has been carried out. This sensitivity study is performed for proposed boundary conditions and geometry under turbulent pulsatile flow. In accordance with this purpose the mesh dependency and numerical error procedure by claimed Celik et al [59] was implemented to cases. In this way different meshes were generated N1 representing fine mesh, N2 representing medium mesh, and N3 representing coarse mesh. The details of the mesh prsented in Table 4.3 , where N1, N2 and N3 denote mesh element count in thousands.

Table 4.3. Mesh details for sensitivity study.

	Fluid Domain	**Solid Domain**
Element Type	Polyhedral	Hexahedral
N1	141.95 k	15.53 k
N2	104.62 k	10.26 k
N3	71.37 k	7.30 k

Herein a deformation probe (mm) for a critical point and calculated wall shear stress (Pa) for fluid-solid interface region were selected as observed variables. In other words, observed variables ensure whether mesh resolution was adequate or not. As can be seen in Figure 4.3, the deformation probe was determined considering to maximum deformation region. Values of selected parameters has been obtained at t $\approx$ 0.12 s which is the peak point for the used pulsatile inlet flow conditions. The outcomes of the test are given in Table 4.4. Here $e^{21}a$ and $e^{21}ext$ are approximate relative error and extrapolated relative error, respectively. $GCI^{21}fine$ is fine Grid Convergence Index; an indicator for numerical error. In this method mentioned error is calculated based on both results for observed variables and average volume of mesh element for each mesh. Therefore, $GCI^{21}fine$ includes effect of all generated mesh error with respect to the medium mesh. As it can be seen from the calculated values, the numerical error in the fine-mesh solution for deformation and wall shear stress are 0.31% and 0.91%, respectively, without accounting for modelling errors.

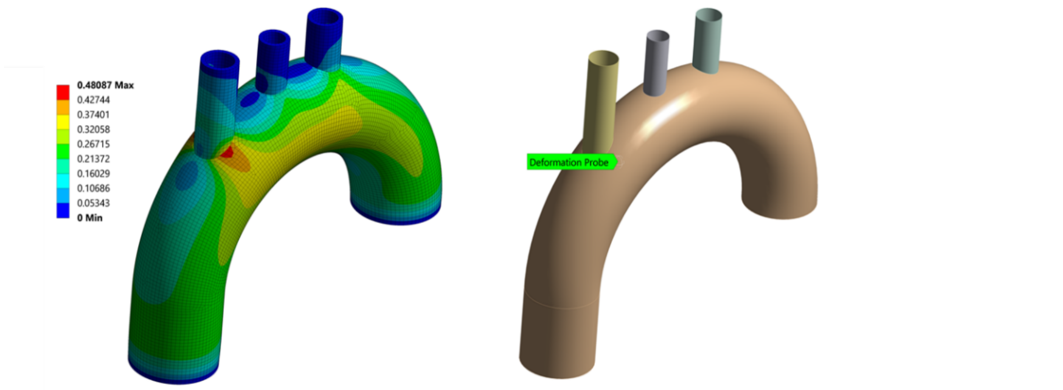

Figure 4.3. Location of the deformation probe.

Table 4.4. Mesh sensitivity and numerical error.

	Deformation	**Wall Shear Stress**
Results for Observed Variable	0.71 mm @ N1 fine 0.70 mm @ N2 medium 0.67 mm @ N3 coarse	106.64 Pa @ N1 fine 106.64 Pa @ N2 medium 106.64 Pa @ N3 coarse
$e^{21}a$	0.15%	1.41%
$e^{21}ext$	0.25%	0.72%
GCI^{21} fine	0.31%	0.91%

In addition to deformation and wall shear stress, variation of velocity magnitude with mesh resolution was also investigated at selected critical locations. Thus, the velocity distribution at the left common carotid artery outlet, which is also described as outlet2, shown in Figure 4.4. In here for t=0.12 s, the average and maximum errors between coarse and medium mesh are calculated as %3.6, and %24.6, respectively. On the other side, between medium and fine mesh average and maximum errors have become 1.6% and 9.8% It can be noticed in Figure 4.4 despite only several points these errors stand outed, there is a similar behaviour for velocity distribution between meshes. As it can be perceived from values given in both Table 4.4 and Figure 4.4, numerical errors associated with mesh resolution and discretization scheme are found to be in acceptable levels in our computational domain. Therefore N2 medium mesh is chosen and used to carried out in all analyses.

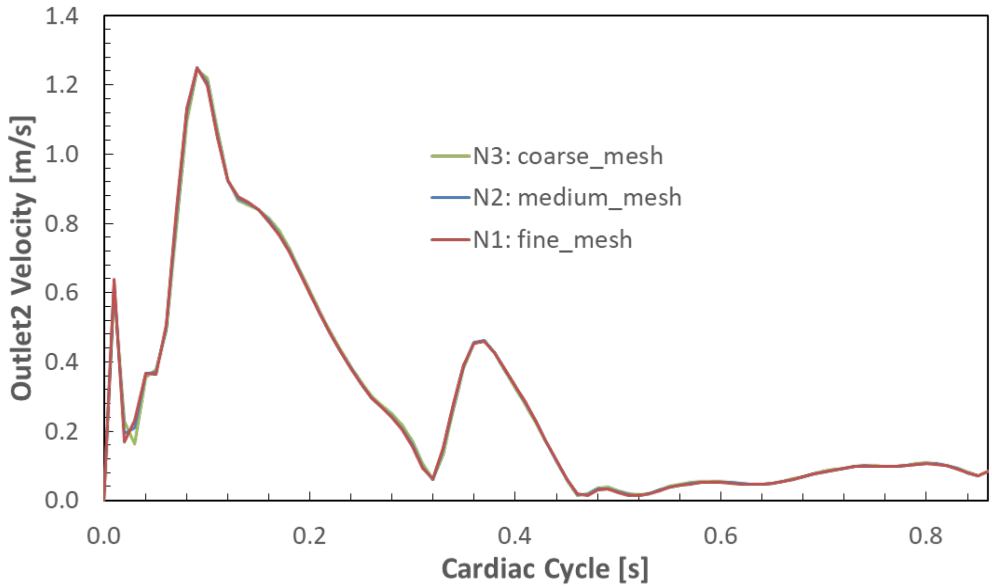

Figure 4.4. The variation of velocity magnitude with mesh resolution.

4.2. Cardiac Cycle and Time Step

In this thesis; cardiac cycle and time-step dependency studies have been carried out to determine acceptable cardiac cycle and time-step for capturing intended hemodynamic characteristics. This sensitivity study is carried out for proposed boundary conditions and geometry under turbulent pulsatile flow. Initially it was determined which cardiac cycle data would be considered. As mentioned in Section 2.2.1. our cardiac cycle is determined as 0.86s. Because both flow and structure characteristics can show undesirable uncertainty due to numerical error. Therefore, four cardiac cycles which are defined below data were obtained:

- I. Cardiac cycle 1: 0s - 0.86s
- II. Cardiac cycle 2: 0.86s - 1.72s
- III. Cardiac cycle 3: 1.72s - 2.58 s
- IV. Cardiac cycle 4: 2.58s - 3.44 s

To compare results, max deformation value at critical location which is shown in 4.3 was handled. To focus incompatible region data obtained at t ≈ 0.03 s and t ≈ 0.08 s, which have maximum difference between results, were tabulated in Table 4.3. According to these results, the results of all the other cardiac cycle except the first cardiac cycle are similar. To give an example, percentage difference in deformation at t ≈ 0.03 s are 40.08%, 1.27% and 0.05% for cycle1-cycle2, cycle2-cycle3, cycle3-cycle4, respectively. In a similar way at t ≈ 0.08 s, percentage difference becomes 2.6%, 0.14% and 0.04% for cycle1-cycle2, cycle2-cycle3, cycle3-cycle4, respectively. In short results given from cardiac cycle 3 which means between 1.72s and 2.58 are quite acceptable.

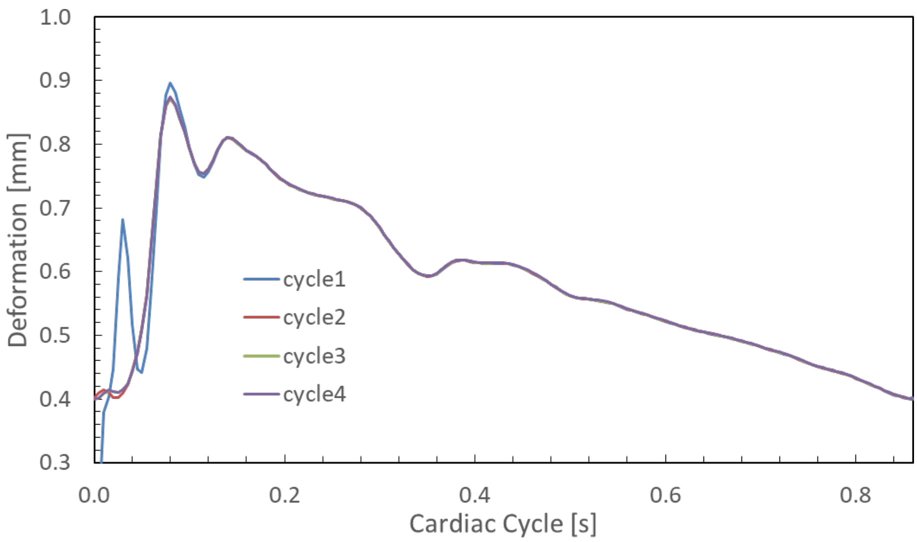

Figure 4.5. Deformation distribution for different cardiac cycle.

Table 4.5. Deformation value for different cardiac cycle.

	Cycle1	**Cycle2**	**Cycle3**	**Cycle4**
deformation @ t=0.03s	0.682mm	0.409mm	0.414mm	0.414mm
error @ t=0.03s (wrt to previous cycle data)	-	40.08%	1.27%	0.05%
deformation @ t=0.08s	0.896mm	0.872mm	0.874mm	0.874mm
error @ t=0.08s (wrt to previous cycle data)	-	2.60%	0.14%	0.04%

After the appropriate cardiac cycle data time frame has been determined transient calculations which have 0.01, 0.005 and 0.001 time-step were executed through 1sec due to computational cost. As illustrated in 4.13, except initial time frame between 0s and 0.15s, there is good agreement between the results. Initialization data between solid and fluid interaction leads this initial mismatch. As mentioned previously, this difference will disappear in following cardiac cycle data. Concisely it is obvious that the time step size used in this study, selected as 0.005s, is acceptably small to provide an acceptable confidence level in the results.

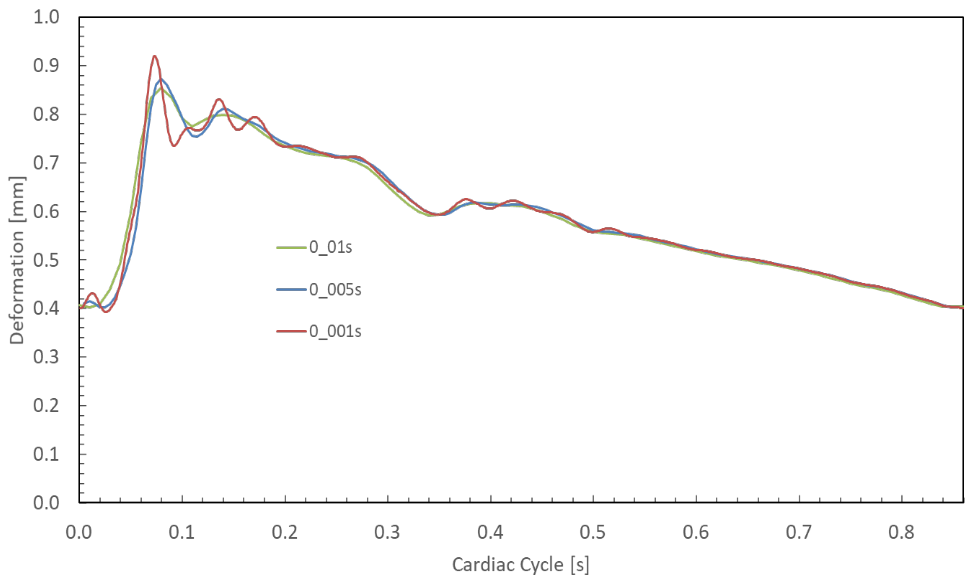

Figure 4.6. The variation of deformation with time-step resolution.

4.3. The Effect of the Support Type

To eliminate effect of support type on the solution two different conditions which are fixed, and displacement were applied to boundaries. In line with this purpose, the initial geometry has been extended along the downstream direction for each outlet to observe effect of support type. All numerical calculations were performed according to boundary conditions given Section 2 and Section 3 and solution method given in Section 3. For branch outlets, in extension1 outlet faces were elongated towards downstream direction by 4 mm from initial position whereas in extension2 outlet faces were elongated towards downstream direction by 6 mm from initial position. On the one hand, in extension1 aorta outlet face was elongated towards downstream direction by 5 mm from initial position whereas in extension2 it was extended as 6 mm. This extension study is described in Figure 4.7. Afterwards, the mentioned previously fixed and displacement support conditions have been imposed for each geometry. In this way six different comparison results have been obtained. To evaluate results von-Mises stress inside the blood vessel wall have been calculated at initial location for all cases. For a numerically remarkable comparison, a difference calculation parameter in terms of percentage was constituted as

$$\%Difference = \frac{VonMisesStress_{fixedsupport} - VonMisesStress_{displacementsupport}}{VonMisesStress_{fixedsupport}} \; x \; 100. \tag{4.1}$$

Thus, fixed support and displacement support were compared for initial, extension1, and extension2 case in terms of percent difference in Von-Mises stress.

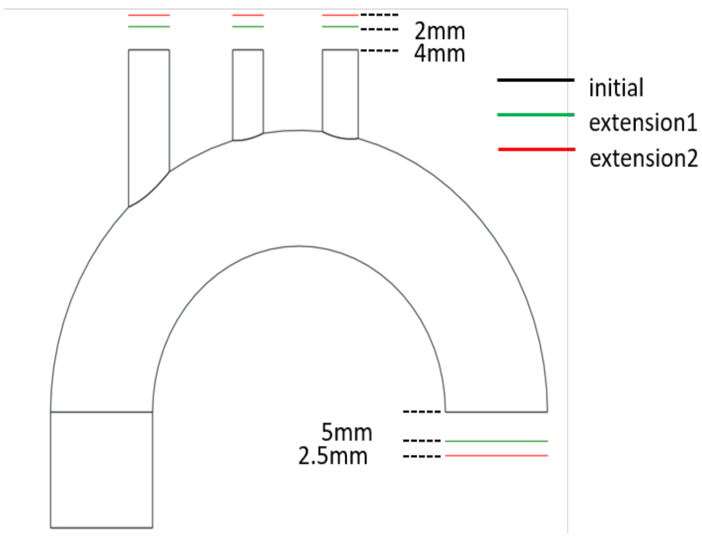

Figure 4.7. The extension study for understanding the effect of support type.

Von-Mises Stress comparisons between fixed and displacement support for descending aorta, brachiocephalic artery, left common carotid artery, and left subclavian artery were illustrated in Figure 4.8, 4.9, 4.10, 4.11 respectively. As can be seen in Figure 4.8, percentage difference is about 1.5% for initial geometry whereas approximate percentage difference is 0.5% and 0.25% for extension1 and extension2, respectively. Furthermore, in brachiocephalic artery while average percentage difference in von-Mises stress is 3% for initial case, this difference is less than 1% for both extension1 and extension2. Similarly, extension cases have noticeably reduced difference in von-Misses stress for both left common carotid artery and left subclavian artery. It can be inferred that as the distance, where support condition is applied, is increased the effect of the support type on reference location is decreased. Therefore, in our computational model extension1 approach is chosen considering both numerical results for von-Mises stress and computational cost due to model size.

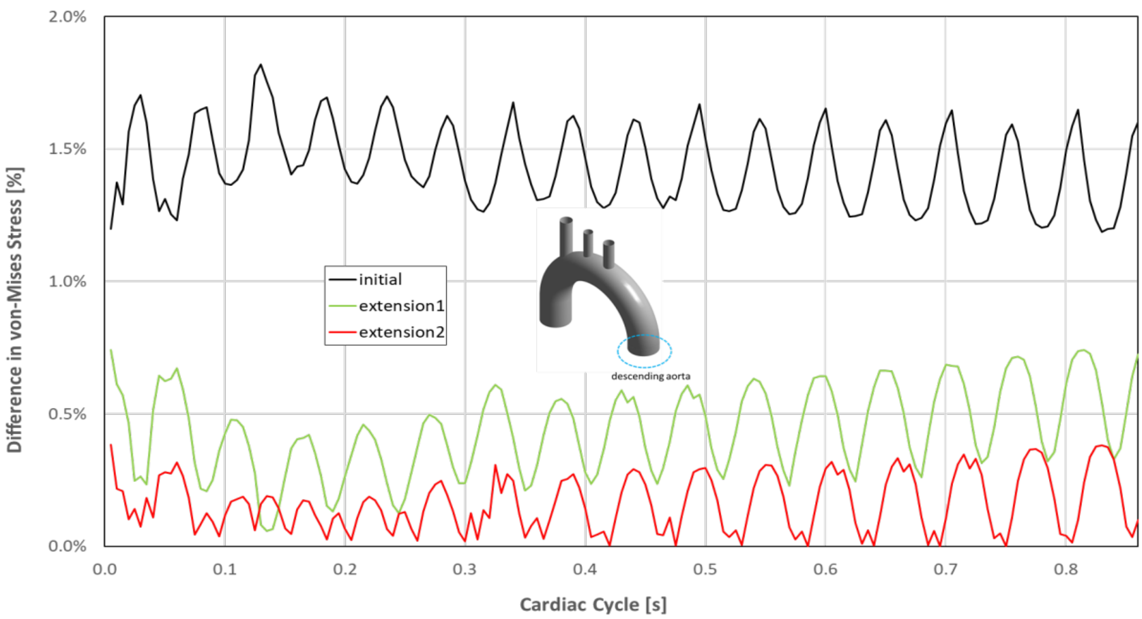

Figure 4.8. Von-Mises stress comparison between fixed and displacement support for descending aorta.

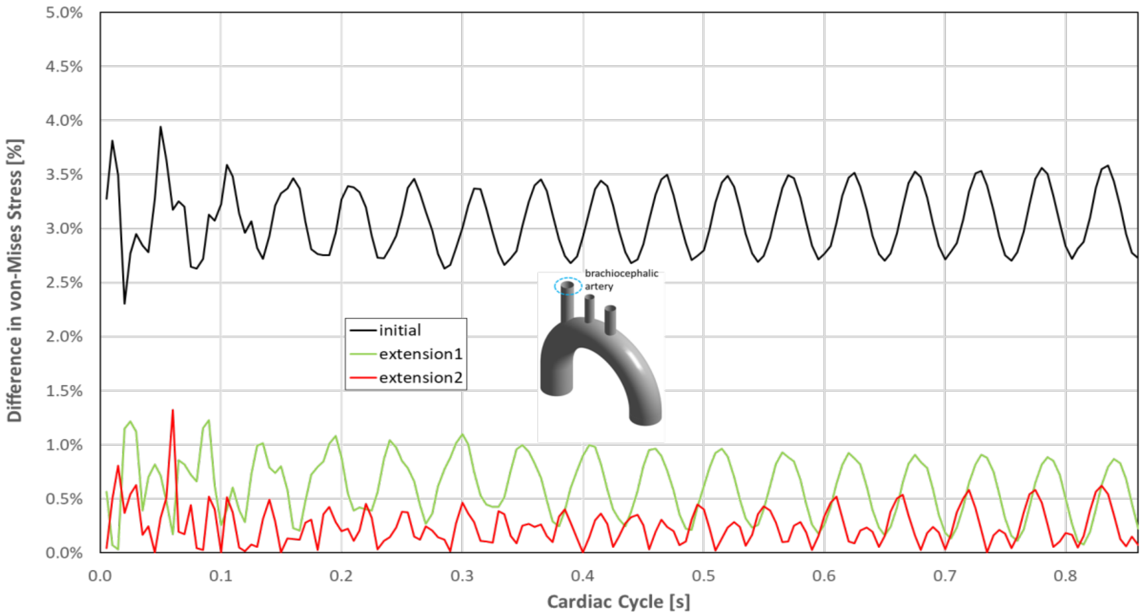

Figure 4.9. Von-Mises stress comparison between fixed and displacement support for brachiocephalic artery.

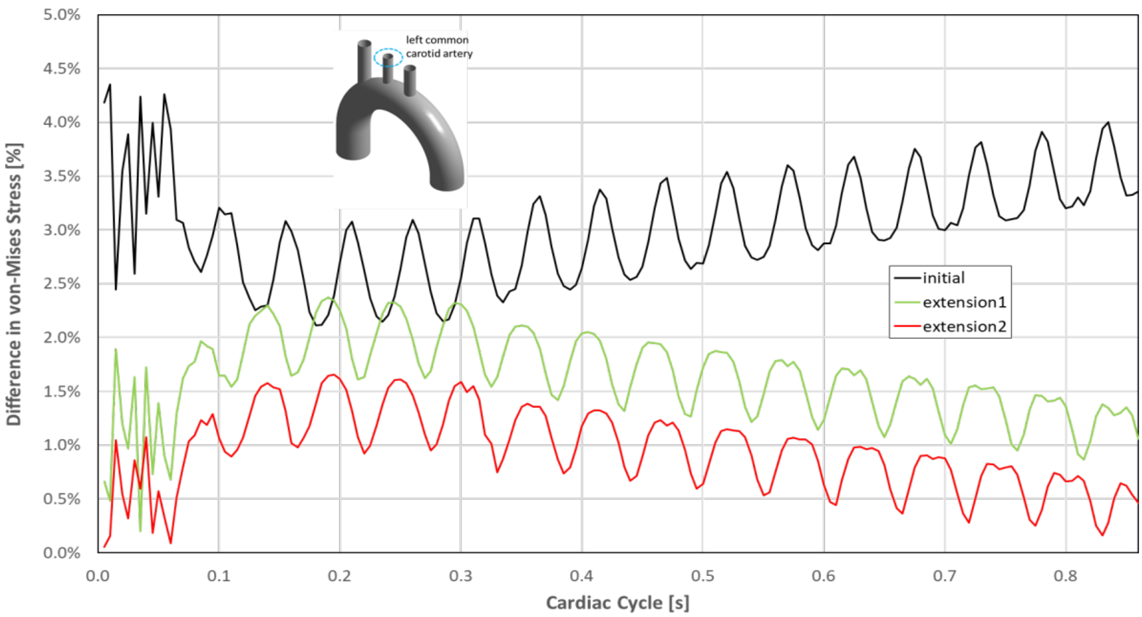

Figure 4.10. Von-Mises stress comparison between fixed and displacement support for left common carotid artery.

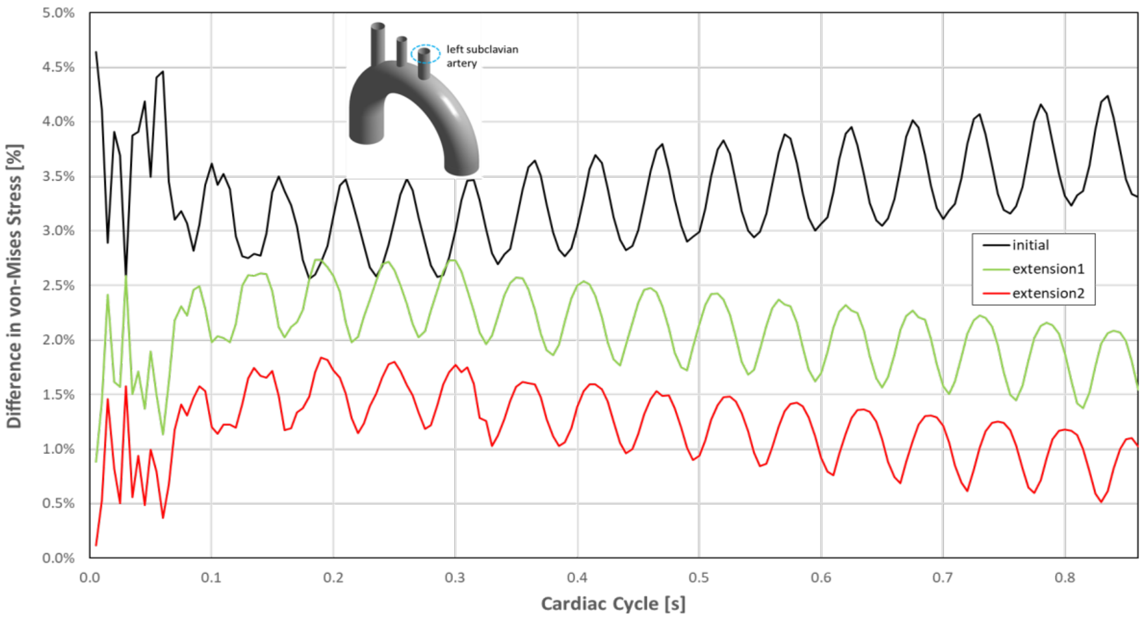

Figure 4.11. Von-Mises stress comparison between fixed and displacement support for left subclavian artery.

4.4. Validation Studies

4.4.1. Newtonian-Laminar Flow for Fluid Domain

In this thesis, several validation studies have been carried out that were determined according to related blood flow phenomena. Initially, the Newtonian model is compared with both the experimental and numerical results of Budwig et al. [13]. Furthermore, numerical results of Khanafer et al. [40] including similar geometry was considered for evaluation of result. Budwig et al. [13] have observed flow characteristics with particle image velocimetry by using a Newtonian fluid including silica beads in their experimental study. They have examined for abdominal aortic aneurysm for varied Reynolds number through both numerically and experimentally. In their model, D represents length a maximum dilated diameter,whereas d represents undilated aortic diameter. The generic aneurysm model which was handled in this study is illustrated in Figure 4.12. This benchmark study was performed in case the reference diameter of the aorta is d=8 mm and Reynolds number is Re=400 then average blood properties were assumed as Newtonian with reference viscosity is 0.00345 N.s/m^2 and blood density is 1050 kg/m^3. The entrance length and outlet length were taken as 6D and 15D, respectively. Besides, Khanafer et al. have defined the geometry of the aneurysms using a sine function as

$$f(z) \; = \frac{D-d}{4}\left[1 + sin(\frac{2\pi z}{L} \; - \frac{\pi}{2})\right] \; + \frac{d}{2}f \; or \; 0 \leq z \leq L. \tag{4.2}$$

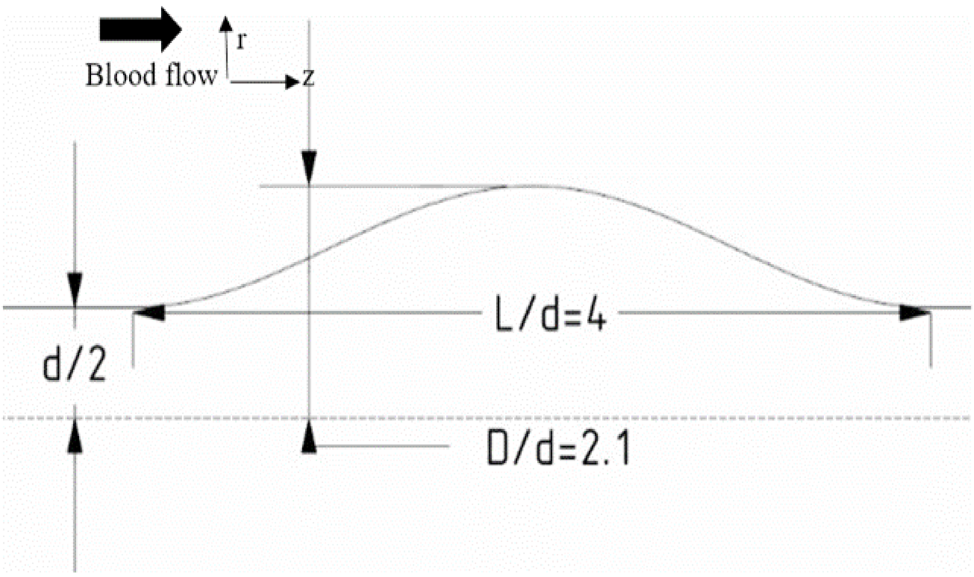

Figure 4.12. Aneurysm model in 2D-axisymmetric [13].

CFD analyses were performed in the 2D, axi-symmetry, steady-state, incompressible flow condition and 1 atm atmospheric condition. Solution method settings are identical to mentioned in Section 3.2. Because steady-state solution is performed the pseudo transient option enables the pseudo transient algorithm in the coupled pressure-based solver. This algorithm effectively adds an unsteady term to the solution equations to improve stability and convergence behaviour. Under-relaxation factors of this model is well set as default for steady-state cases in the software used. Through the numerical calculation, convergence control was controlled via continuity, momentum, and turbulence equations. At the end of the analysis, it is ensured that mass conservation was achieved.

Comparison of the axial velocity profile at the centre of the aneurysms with both experimental and numerical study of Budwig et al. was given in Figure 4.13. This figure shows an excellent agreement between results. Maximum error between the present numerical study and the experimental study is about 9% which is occurred at r/d ≈0.37.

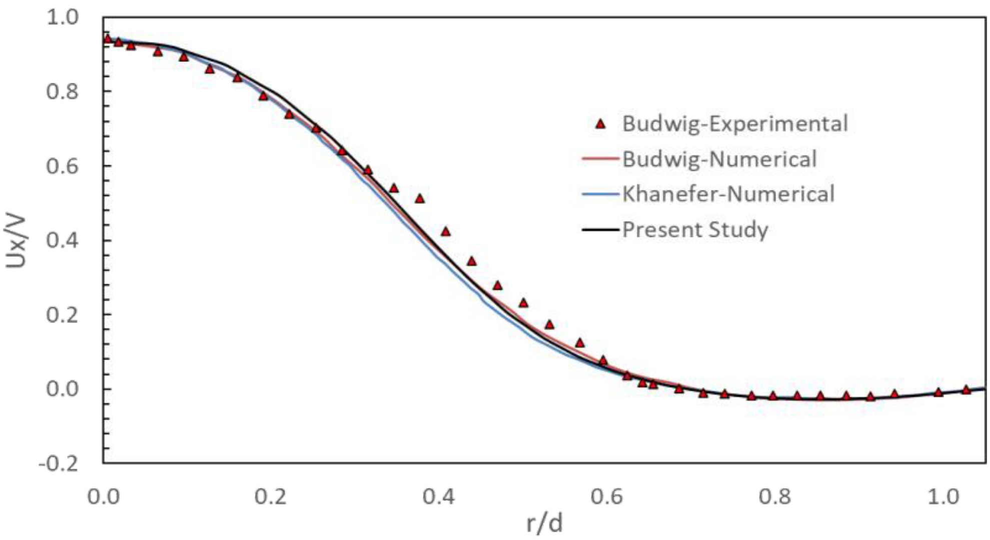

Figure 4.13. Comparison of steady newtonian profile across the center of the aneurysms.

4.4.2. Newtonian-Turbulent Flow for Fluid Domain

Another benchmark study was carried out for geometry given by the interlaboratory study of Stewart et al [41] which is illustrated in Figure 4.14. The main objective of this study to provide valuable benchmark database, to support develop improved modelling techniques and to emphasize best practice for using CFD in medical sector. In accordance with this purpose, they carried out experimental study at different Reynolds number. Besides, 28 group from various reserach center submitted their CFD results including different solution technique, turbulence modelling. It can be deduced that there is no single turbulence model is superior considering this problem.

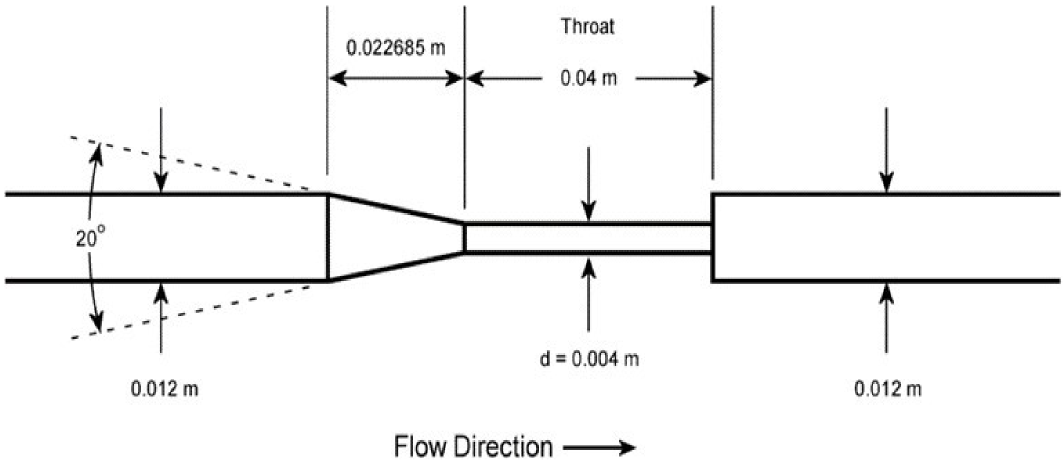

Figure 4.14. Geometric specifications for the interlaboratory study of Stewart et al. [41].

Their validation model including both accelerating and decelerating flow, consists of a small nozzle which involves a radial step, sharp edges, and a cross-sectional stenosis. This validation study was performed for the throat Reynolds number is 6500 and average blood properties were assumed as Newtonian reference viscosity is 0.0035 N.s/m^2 and blood density is 1056 kg/m^3. The entrance length and outlet length were taken as three times of throat length and six times of throat length, respectively. Numerical computations were handled in the 2D, axi-symmetry, steady-state, incompressible flow condition and 1 atm atmospheric condition with turbulence due to high Reynolds number. Here turbulence was modelled using Shear Stress Transport (SST) k- model turbulence model with dimensionless wall distance, y$^+$, is equal to 1. Solution method settings are identical to mentioned in Section 3.2. and Section 4.3.1.

Comparing of the axial velocity distributions along nozzle centerline and at z=8mm with both experimentally and numerically of Stewart et al. were given in Figure 4.15 and in Figure 4.16 respectively. These figures illustrate that there is good agreement between the experimental and numerical results and present study. For comparison of the axial velocity along nozzle centerline, which is in given in Figure 4.15, the maximum error between experimental study and present study have been found about 8.5%. Similarly, the maximum error was calculated as 9.1% for the comparison of the axial velocity at axial location, which is in given in Figure 4.16.

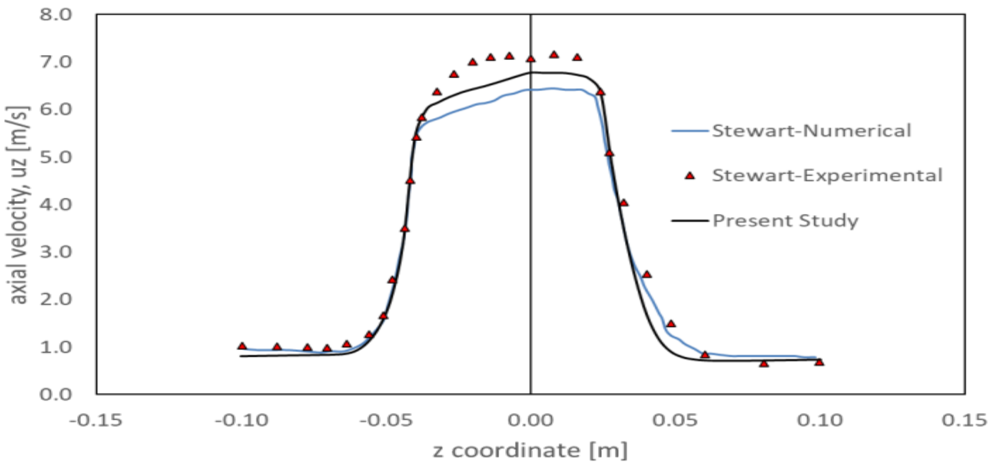

Figure 4.15. Comparison of the axial velocity along nozzle centerline with study of Stewart et al. [41].

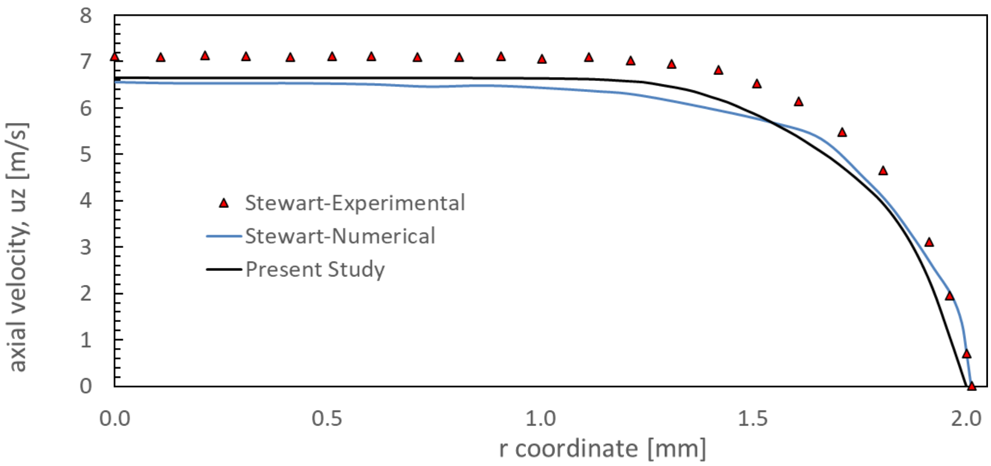

Figure 4.16. Comparison of the axial velocity distribution at z=8mm with study of Stewart et al. [41].

5. RESULTS AND DISCUSSION

The results of turbulence modelling effect for pulsatile blood flow in selected 3-D aorta geometry are covered in Section 5.1., and effects of solid domain parameters on hemodynamic characteristics are given in Section 5.2. and Section 5.3. viscous characteristics are investigated.

5.1. Investigations of Turbulence Modelling Effects

In this section, turbulence modelling effects on hemodynamic characteristics are evaluated by performing numerical analyses with twelve different turbulent model. As mentioned previously since Reynolds number can reach 6000 for the proposed geometry and imposed conditions, determining the correct turbulence model is very crucial. Description of both modelled cases and reference sections for assessment of results are shown in the Section 5.1.1. While differences in the hemodynamic risk indicator such as OSI and HOLMES are discussed in Section 5.1.2., comparison of the velocity characteristics are handled in Section 5.1.3. Besides, results involving displacement and von Mises stress are given in Section 5.1.4.

5.1.1. Definitions of handled cases and reference sections

In this thesis analyses including twelve different turbulence model are which are given in Table 5.1 employed. These turbulence models mainly consist of κ-ϵ and κ-ω RANS based models which are solved time-averaged Navier-Stokes equations.

Table 5.1. Turbulence model cases.

Case	**Turbulence Model**	**Sub-Model**	**Near Wall Treatment**	**Number of Equations**
Case1	k-epsilon	Standard	Standard Wall Function	2
Case2	k-epsilon	Standard	Enhanced Wall Treatment	2
Case3	Spalart-Almaras	Vorticity-based	-	1
Case4	k-epsilon	RNG	Standard Wall Function	2
Case5	k-epsilon	RNG	Enhanced Wall Treatment	2
Case6	k-epsilon	Realizable	Standard Wall Function	2
Case7	k-epsilon	Realizable	Enhanced Wall Treatment	2
Case8	k-omega	Standard with low-Re corrections	-	2
Case9	k-omega	SST with low-Re corrections	-	2
Case10	k-omega	Standard Transition	-	3
Case11	k-omega	SST Transition	-	4
Case12	Reynolds stress	Linear Pressure Strain	-	7

Since Hemodynamic risk indicators based on wall shear stress in each direction are calculated time-averaged during cardiac cycle, these values are obtained along the vessel wall without needing specific both instance of time and locations. On the other side, definite reference location and time intervals must be specified for other variables. As it can be noticed in Figure 5.1 peak velocity of the cardiac cycle, which is t≈0.12s, and starting time of the diastole, which is t≈0.35s, are determined as time intervals for the evaluation of the velocity characteristics.

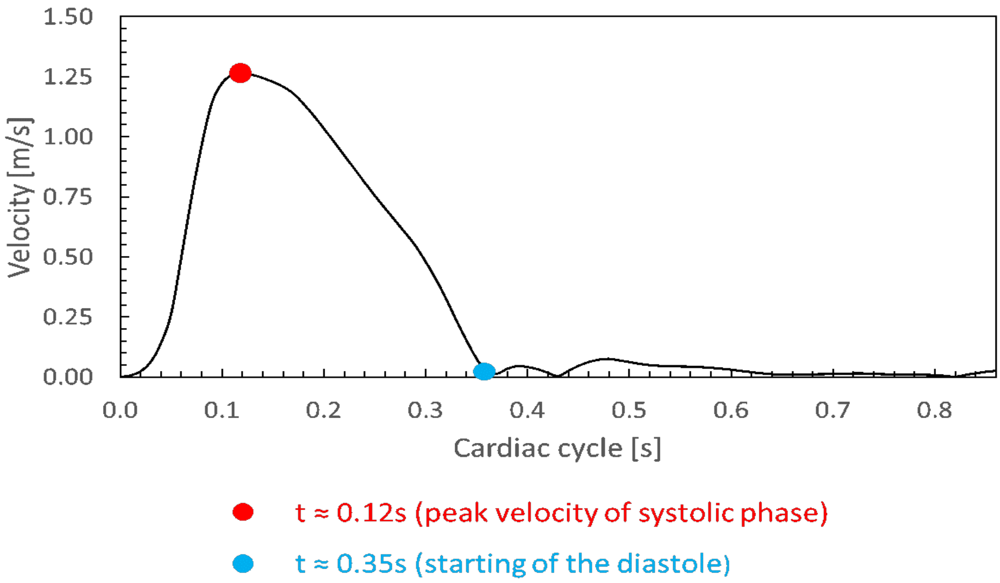

Figure 5.1. Instance of times for results.

Furthermore, reference sections are shown in Figure 5.2 including all used planes and lines. Section plane from the midsection which means Z=0 is generated to observe velocity distribution along the whole domain clearly. This is illustrated as Plane1 in Figure 5.2. Plane2 and Plane3 are the transverse sections that are generated over brachiocephalic artery, left common carotid artery, and left subclavian artery. It can be deduced from the Figure 5.2, whereas Plane2 is located near the junction side, Plane3 is close outlet side. Besides to focus velocity profile on the brachiocephalic artery, left common carotid artery, and left subclavian artery; Line1, Line2 and Line3 are respectively created on the Plane1.

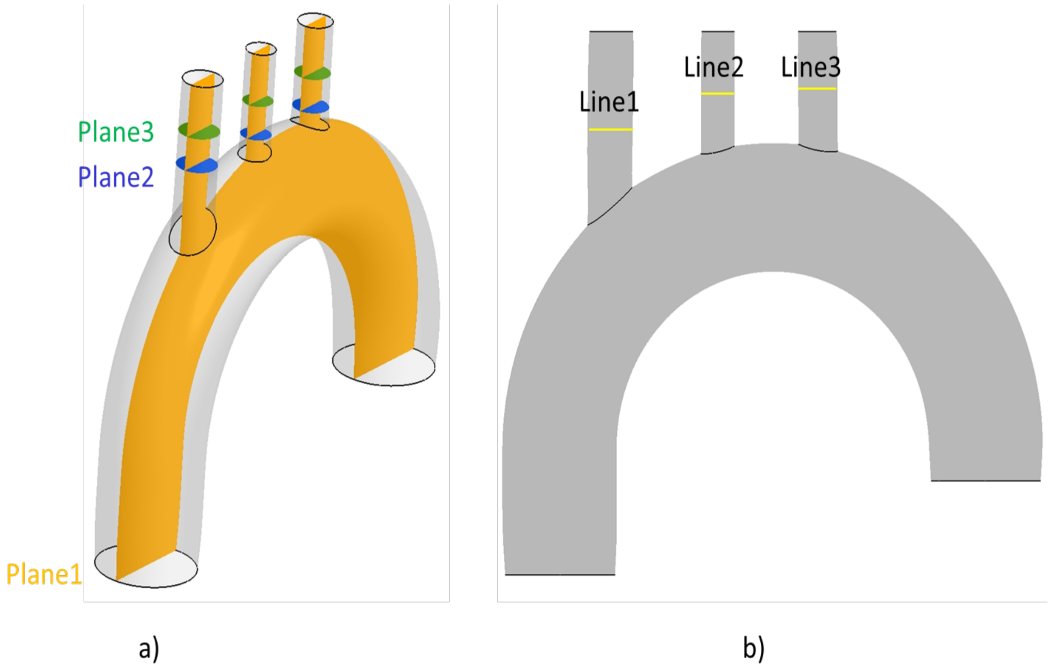

Figure 5.2. Reference sections, (a) Location of Planes, (b) Location of Lines.

5.1.2. Hemodynamic Risk Indicators

Because of phenomena of pulsatile flow, the pressure oscillation at the inlet can be observed that causes periodic oscillations in the direction of wall shear stress. The oscillatory shear index (OSI) represents a numerical parameter for the wall shear stress that is defined as

$$OSI_x = \frac{1}{2}\left(1 - \frac{|\int_0^T WSSdt|}{\int_0^T |WSS|dt}\right). \tag{5.1}$$

OSI is the one of the most used indices in hemodynamic that is useful to determine the temporal oscillations in the immediate wall shear stress vector along the cardiac cycle [60]. Here T denotes the period of the cardiac cycle which is fixed as T = 0.86 s in this study. The OSI value range starts from 0 and goes up to 0.5. Whereas OSI=0 means there is no change in the direction of the vector, OSI=0.5 indicates the 180-degree deviation from the average direction. Another important hemodynamic risk indicator which is used in this study is Highly Oscillatory and Low Magnitude Shear (HOLMES). The HOLMES indicator is the modified version of Time-Averaged Wall

Shear Stress (TAWSS) and calculated as

$$HOLMES = TAWSS(0.5 - OSI). \tag{5.2}$$

In order to observe effects of shear characteristics, HOLMES provides alternative assessment that combine OSI and TAWSS by one expression. The distribution of average OSI value and HOLMES value are shown in Figure 5.3, Figure 5.4, respectively for each case. The slight differences are observed between cases as expected since turbulence models give similar results for global variables when they correctly modelled. Average OSI value for aort geometry along the cardiac cycle is calculated about 0.16. Pirola et al. performed computational study for aorta geometry with pulsatile blood flow which its maximum value is about 0.82 m/s. They calculated average OSI value between 0.12-0.14 for different cases. When this average OSI value is compared to this study considering maximum value of inlet velocity (0.82 m/s for Pirola et al. [61], 1.26 m/s for this study) it can be said that the results are compatible with each other. Case1, Case4 and Case6 which are employed k-epsilon turbulence model including standard wall treatment underestimated OSI value by up to about 5% compared to other cases. This model generally gives poor results for flows both involve separation region and curved geometry which leads large streamline and pressure gradient. As shown in Figure 5.4, similarly good agreement is observed between cases except Case1, Case4, Case6 and Case12 in terms of HOLMES indicator. These four cases overestimate the HOLMES value about 40% - 50% compared with other studies. From a quantitative point of view average HOLMES value is about 0.97 for Case1, Case4, Case6 and Case12, whereas it is approximate 1.42 for the remaining cases. Furthermore, OSI distribution for aorta domain is illustrated in Figure 5.5. Despite being close to each other for aortic arch, different characteristics can be observed at both brachiocephalic artery, left common carotid artery, and left subclavian artery branches and junction regions. To give an example OSI distribution is different along the left common carotid artery and left subclavian artery for Case2 - Case7 - Case10 and Case8 - Case9 - Case11. For both the left common carotid artery and left subclavian artery, although in Case8 - Case9 - Case11, high OSI region extend towards to outlet, high OSI region disappears at upstream side of outlet in Case2 - Case7 - Case10.

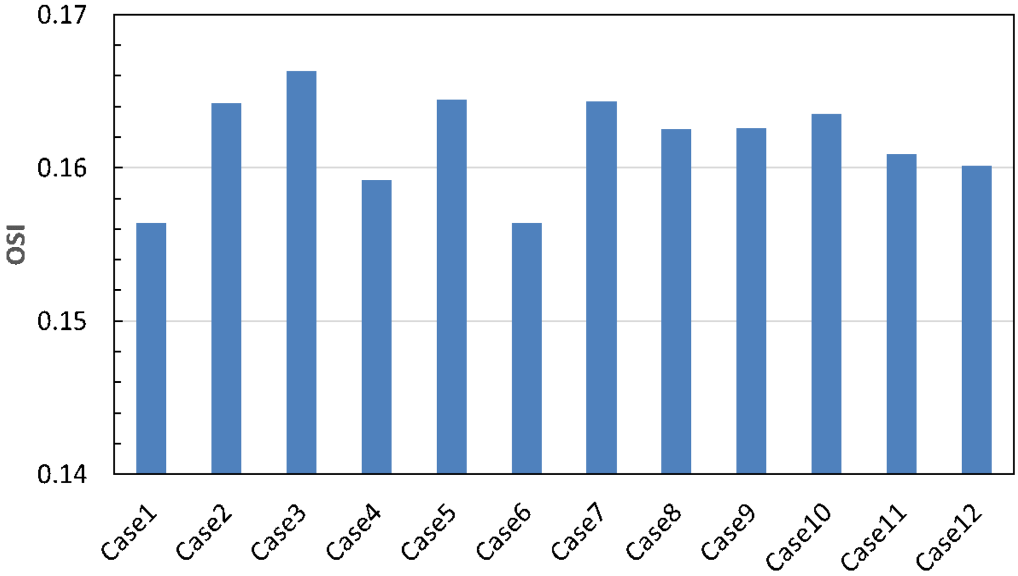

Figure 5.3. Distribution of the average OSI.

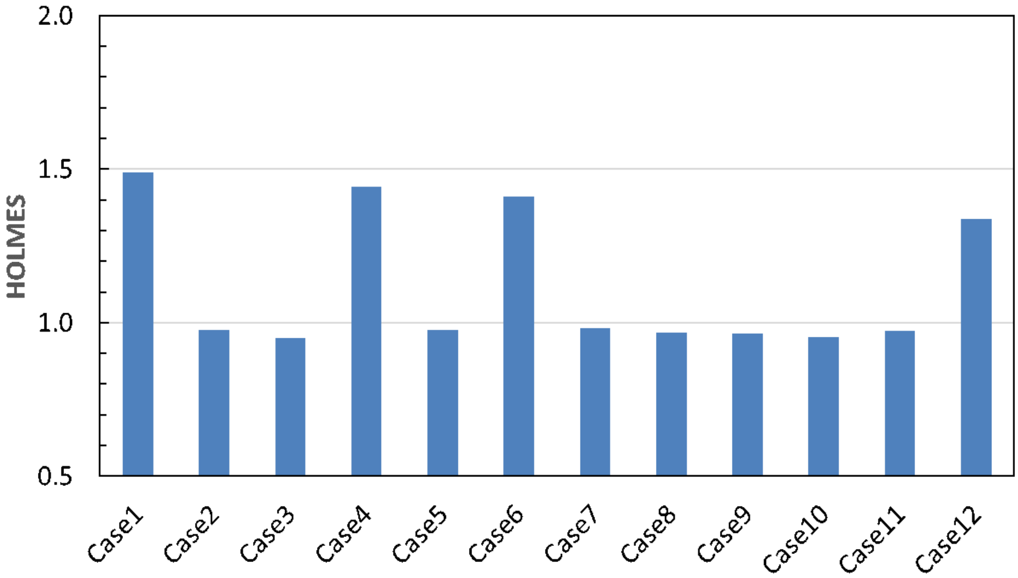

Figure 5.4. Distribution of the average HOLMES.

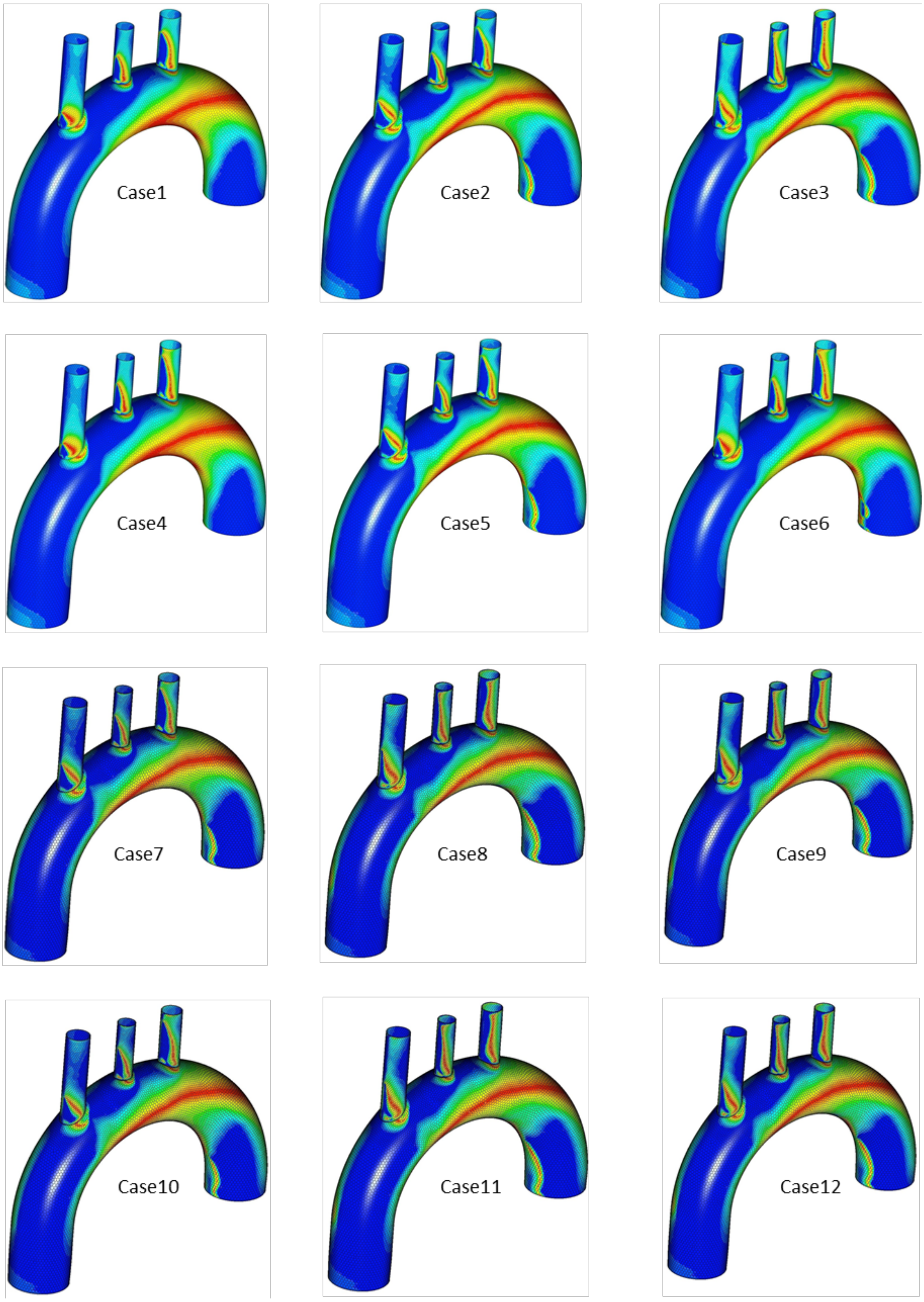

Figure 5.5. OSI distribution.

The threshold value for OSI is determined as 0.2 that represents as low oscillatory shear stresses for OSI < 0.2, and high oscillatory shear stresses for OSI > 0.2 [60]. Regions are involving high level of OSI (OSI > 0.2) have detrimental flow conditions and tend to vessel dysfunction. Obtained percentage of OSI distribution for threshold value is tabulated in Table 5.2 for each turbulence modelling. Six different turbulence models which are Case2, Case5, Case7, Case8, Case9 and Case10 give similar results 38.8% (± 0.2%) for percentage of the low oscillatory shear stress region. Case1, Case4, Case6, Case11 and Case12 underestimates percentage of low oscillatory shear stress region as 3.4%, 2.6%, 3.7%, 0.7% and 1.9%, respectively. Only Case3 overestimates this value about 0.9%. Besides clipped OSI Distribution for OSI > 0.2 is demonstrated in Figure 5.6. Chen et al. [62] have been carried out OSI evaluation by observing different rat groups. Similar to Chen's study, high values of OSI have been observed near the inner vascular wall for all cases. Furthermore, region behind left common carotid artery and left subclavian artery and junction locations can be categorised as the high-risk areas in terms of high oscillatory shear stresses.

Table 5.2. Percentage of OSI distribution for threshold value.

Case	**OSI > 0.2**	**OSI ≤ 0.2**
Case1	35.3%	64.7%
Case2	38.6%	61.4%
Case3	39.6%	60.4%
Case4	36.1%	63.9%
Case5	38.7%	61.3%
Case6	35.0%	65.0%
Case7	38.8%	61.2%
Case8	38.9%	61.1%
Case9	38.7%	61.3%
Case10	38.9%	61.1%
Case11	38.0%	62.0%
Case12	36.8%	63.2%

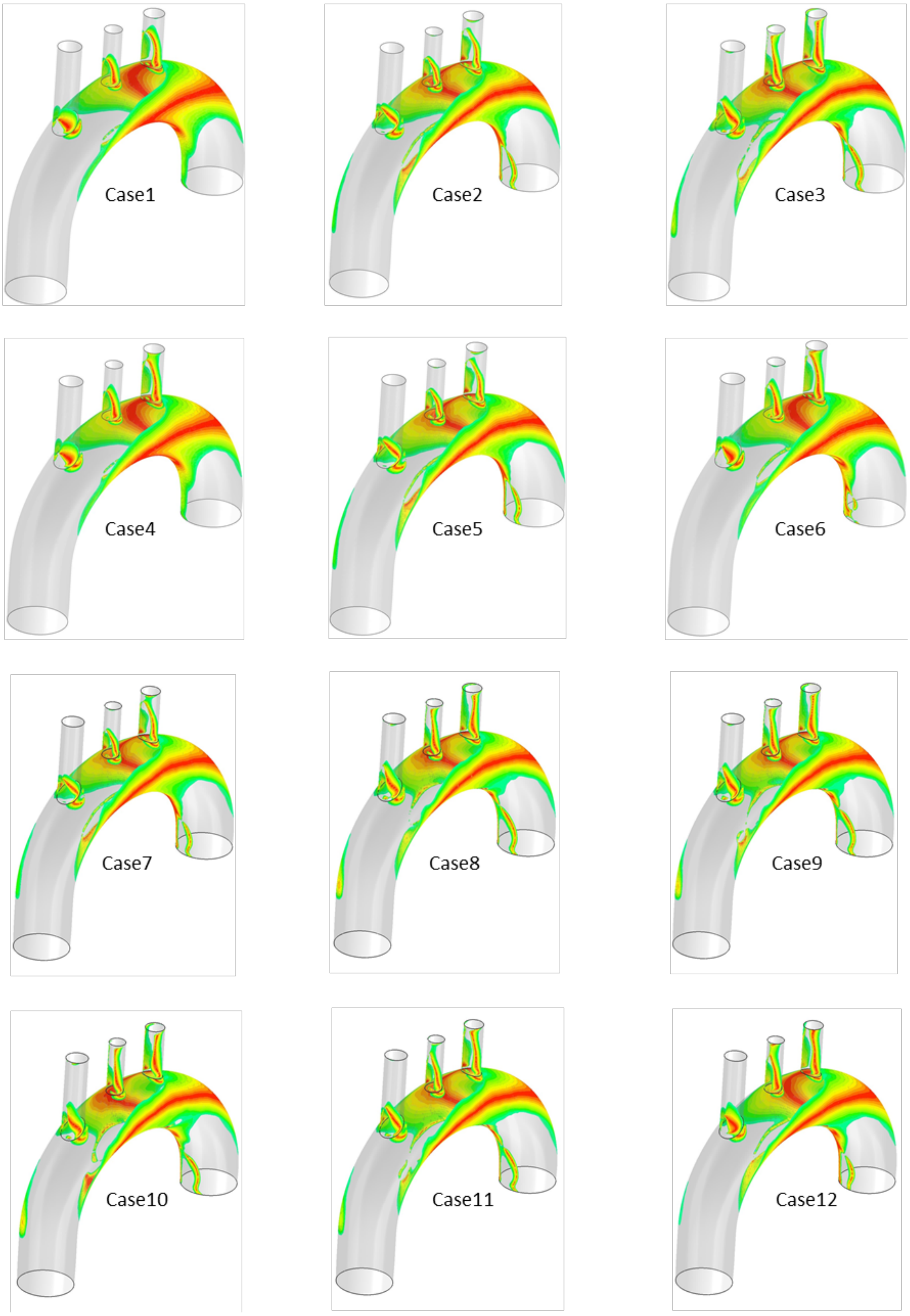

Figure 5.6. Clipped OSI distribution for OSI>0.2.

5.1.3. Velocity Characteristics

Initially, to ensure that results are acceptable velocity vectors at Plane1 have been compared with Afkari's study which is handled similar geometry and boundary conditions. As can be seen from Figure 5.7 the results of the thesis study are found to be in good agreement with the results in Afkari's study [3]. Both velocity distributions have similar flow pattern for whole domain and vortices structures in arteries. High velocity regions are similar for both cases and the size and shape of the vortices region in left subclavian artery so close each other.

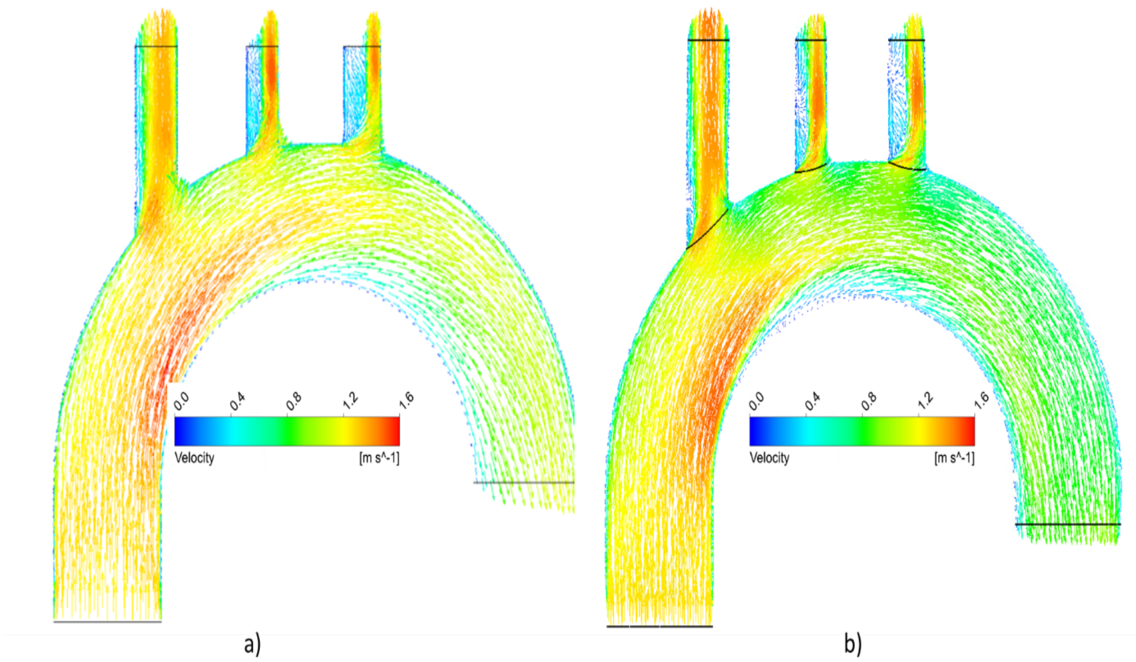

Figure 5.7. Comparison of the velocity vectors at plane1 with Afkari's study [3], (a) Afkari's Study, (b) This Study.

To compare effect of the turbulence modelling on the results, the velocity distribution at peak systole for Plane1 and Plane2 - Plane3 are shown in the Figure 5.8 and Figure 5.9 for all cases, respectively. The flow pattern from ascending to descending aorta show identical characteristic. However due to their complex structures differences flow pattern in three artery routes, which are brachiocephalic artery, left common carotid artery and left subclavian artery, are noticeable. Since brachiocephalic artery have the highest flow rate the peak velocity is observed here according to other arteries.

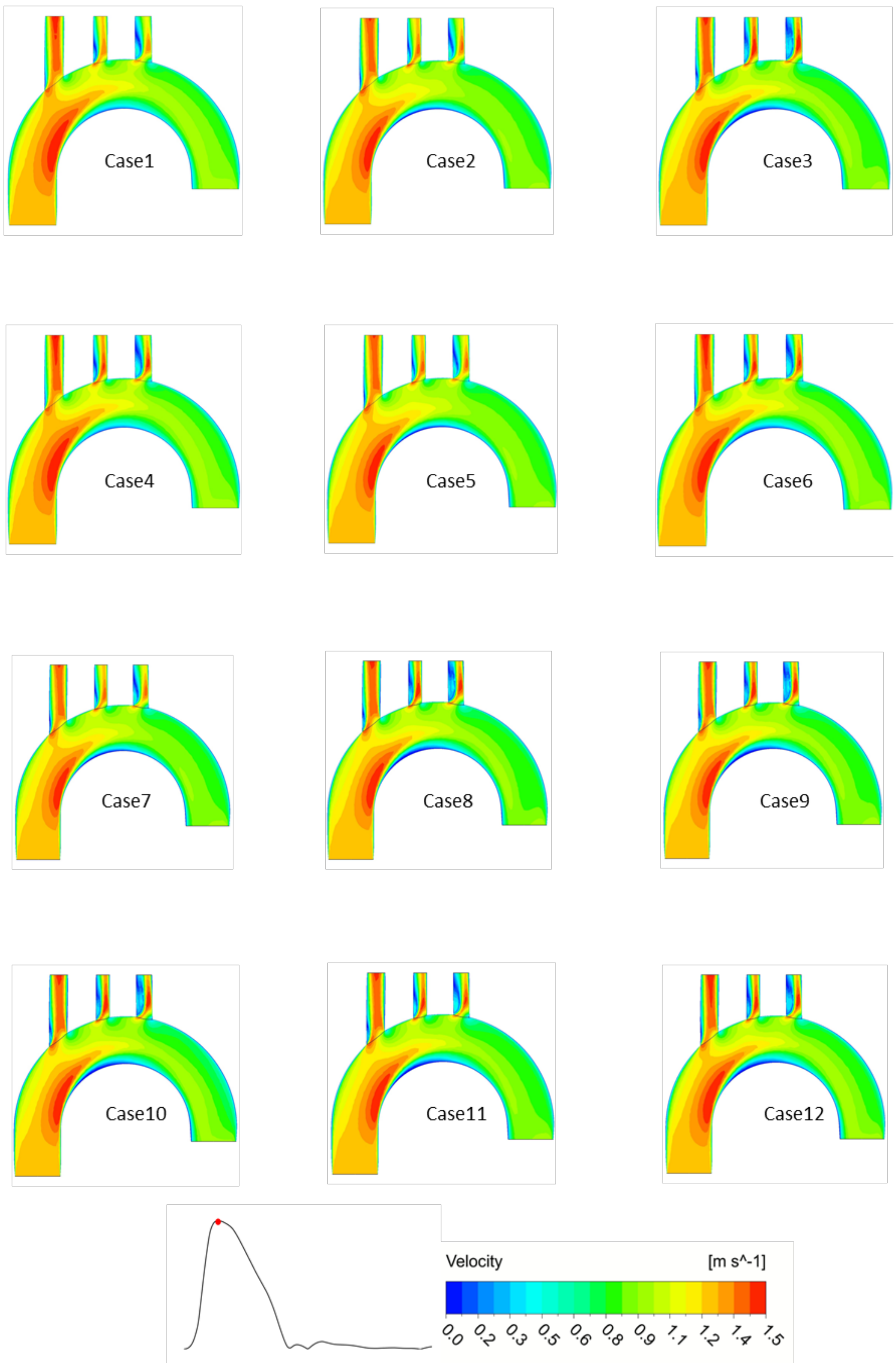

Figure 5.8. Velocity distribution at peak systole for Plane1.

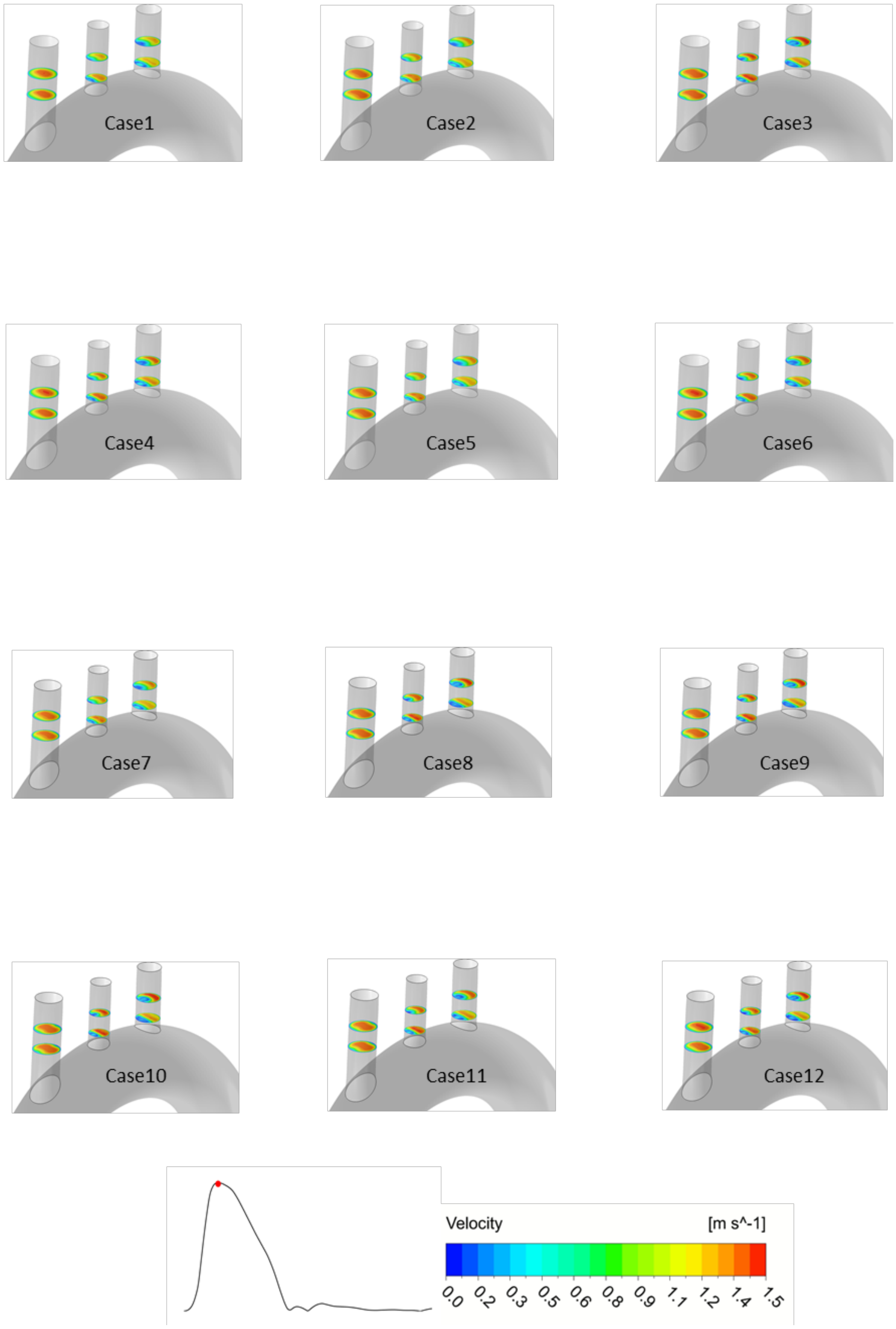

Figure 5.9. Velocity distribution at peak systole for both Plane2 and Plane3.

Comparison of the velocity profile along the Line1 at peak systole is shown in Figure 5.10. As it can be seen in the figure, there is no remarkable difference between velocity characteristics. However, it can be observed that velocities in Case1 and Case3 are different from each other about 5% at dimension distance is equal to 0.88.

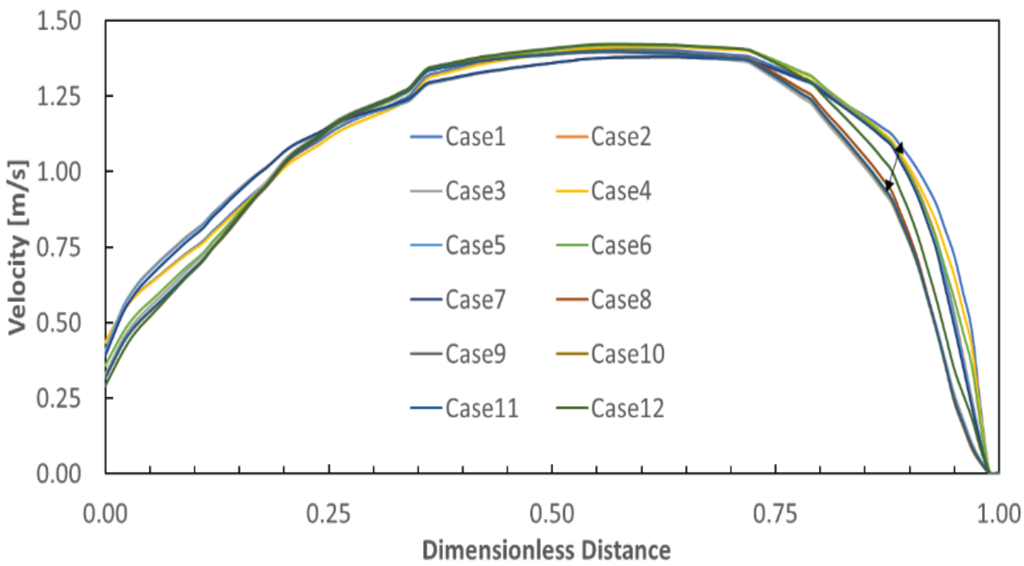

Figure 5.10. Comparison of the velocity-magnitude profile along the Line1 at peak systole.

Comparison of the velocity profile along the Line2 at peak systole is given in Figure 5.11. Results show a significant difference in velocity characteristics. To examine the velocity profiles in this region in more detail velocity in Y direction for k-epsilon turbulence models is displayed via Figure 5.12, for remaining turbulence models is shown in Figure 5.13. The main incompatibility between these two groups is capturing recirculation zone. On the one hand, in k-epsilon group turbulence models except Case6, recirculation characteristics in this region were not observed but on the other hand, both k-omega group and Spalart-Allmaras turbulence models are suitable for complex boundary layer flows under pressure gradient and separation [43]. Case3, Case8, Case9 and Case10 have captured recirculation characteristics identically.

Comparison of the velocity profile along the Line3 at peak systole is illustrated in Figure 5.14. Similarly for detailed evaluation, velocity in Y direction for k-epsilon turbulence models is displayed via Figure 5.15, for remaining turbulence models is shown in Figure 5.16. Turbulence models of k-epsilon group underestimate recirculation zone characteristics in comparisons with k-omega group and Spalart-Allmaras turbulence models along the Line3. Length of the recirculation zone from wall can be calculated as approximate 15%, 17%, 18% and 18% of the dimensionless distance for Case1, Case2, Case5 and Case7, respectively. This parameter for Case4 and Case6 is about 31% and 32%. On the other side, a huge recirculation zone is observed along the Line3 for k-omega group and Spalart-Allmaras turbulence models. Whereas Case11 involve recirculation length parameter from wall as about 31%, this distance in remaining models is nearby 41%.

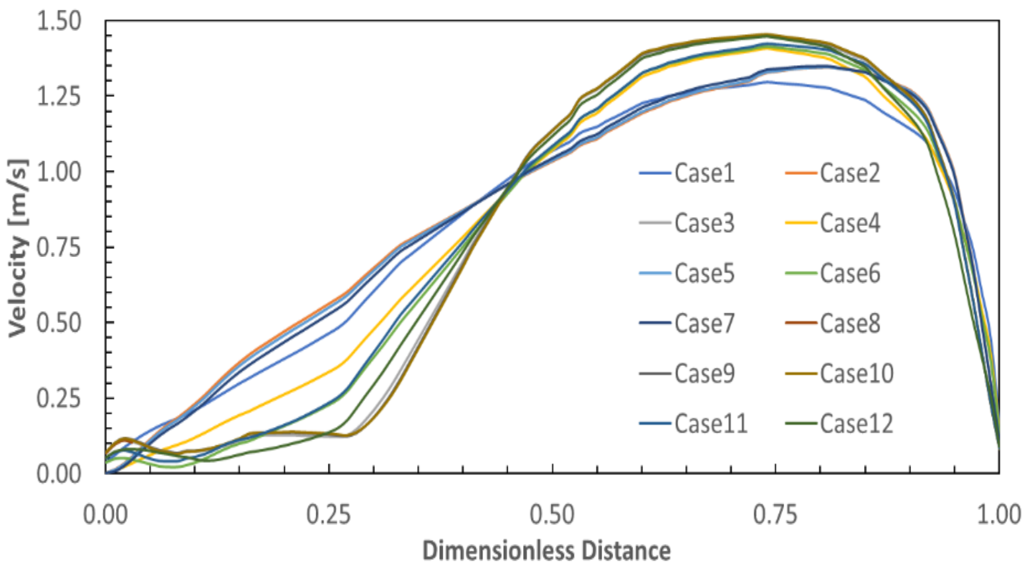

Figure 5.11. Comparison of the velocity-magnitude profile along the Line2 at peak systole.

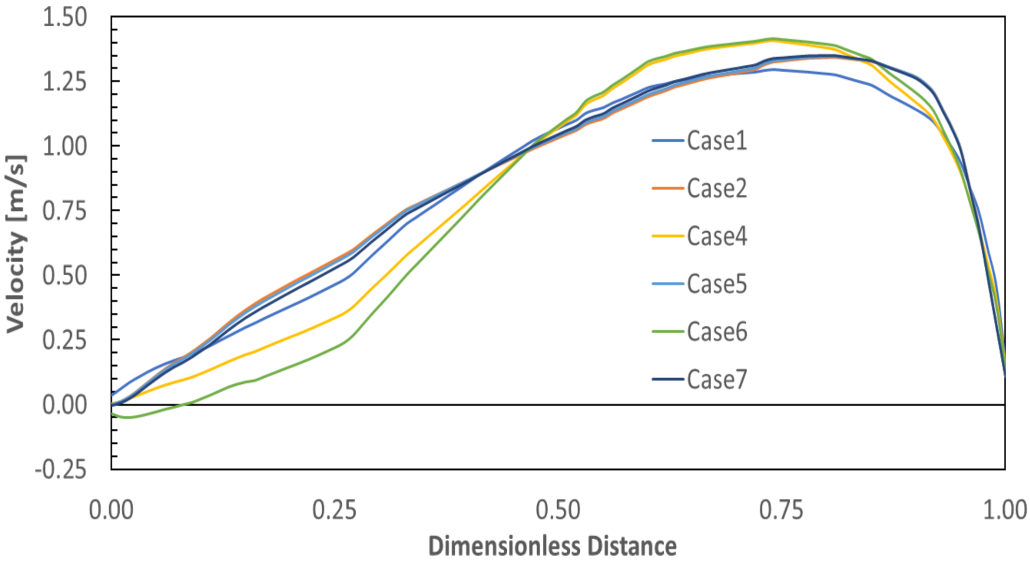

Figure 5.12. Comparison of the velocity-V profile along the Line2 at peak systole for k-epsilon turbulence models.

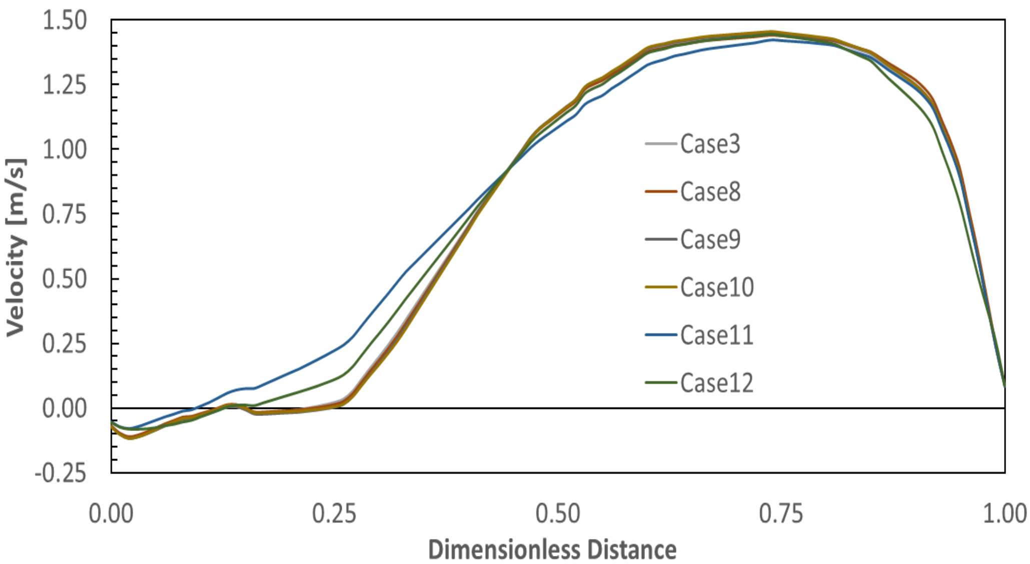

Figure 5.13. Comparison of the velocity-V profile along the Line2 at peak systole for other turbulence models except k-epsilon group.

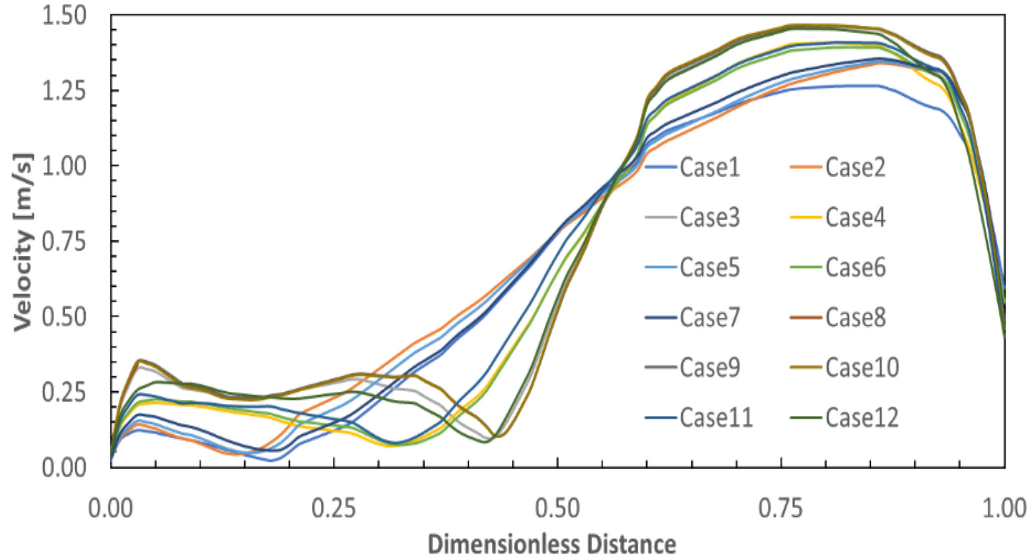

Figure 5.14. Comparison of the velocity-magnitude profile along the Line3 at peak systole.

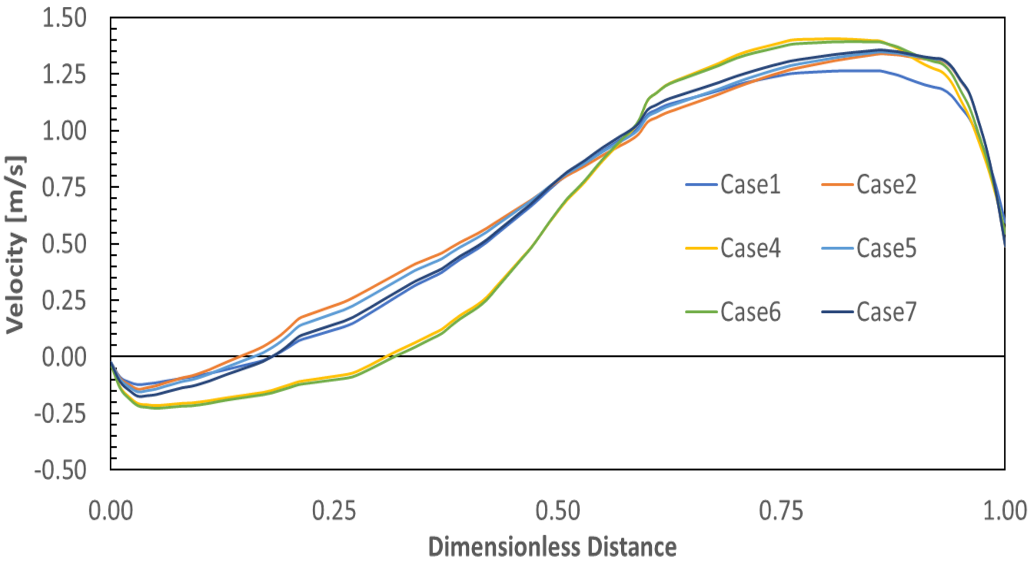

Figure 5.15. Comparison of the velocity-V profile along the Line3 at peak systole for k-epsilon turbulence models.

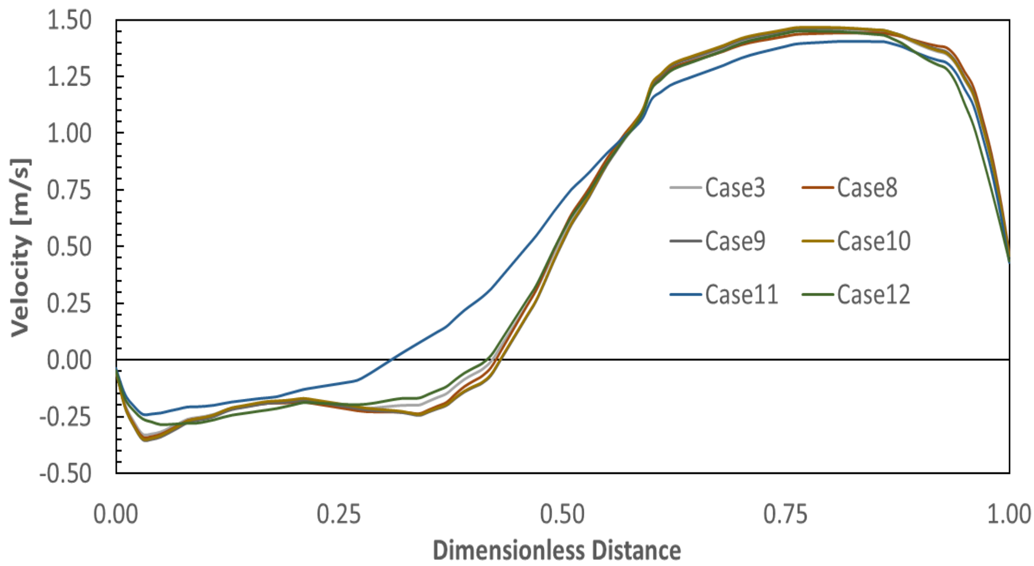

Figure 5.16. Comparison of the velocity-V profile along the Line3 at peak systole for other turbulence models except k-epsilon group.

5.1.4. Displacement and von-Mises Stress

The maximum value of both total displacement and equivalent stress are calculated and tabulated in Table 5.3. Since the maximum variation between cases become about 1.1%, as expected, effect of turbulence models on solid domain parameters are negligible. To support this idea, displacement and von-Mises stress distribution through the cardiac cycle for selected cases are illustrated in Figure 5.17 and Figure 5.18, respectively. As can be seen from the images, the distributions overlap exactly.

Table 5.3. Comparison of the displacement and Von-Mises stress.

Case	**Max Displacement [mm]**	**Max Equivalent (von-Mises) Stress [kPa]**
Case1	1.130	167.85
Case2	1.120	166.53
Case3	1.119	166.18
Case4	1.127	167.68
Case5	1.120	166.53
Case6	1.127	166.53
Case7	1.119	166.51
Case8	1.119	166.23
Case9	1.118	166.09
Case10	1.118	166.02
Case11	1.118	166.02
Case12	1.118	166.02

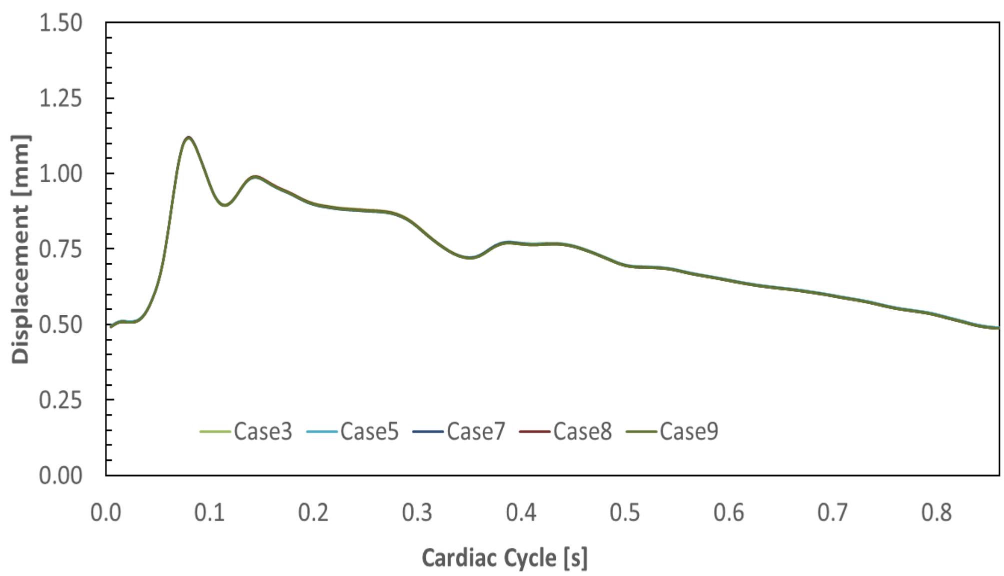

Figure 5.17. Displacement distribution through the cardiac cycle for selected cases.

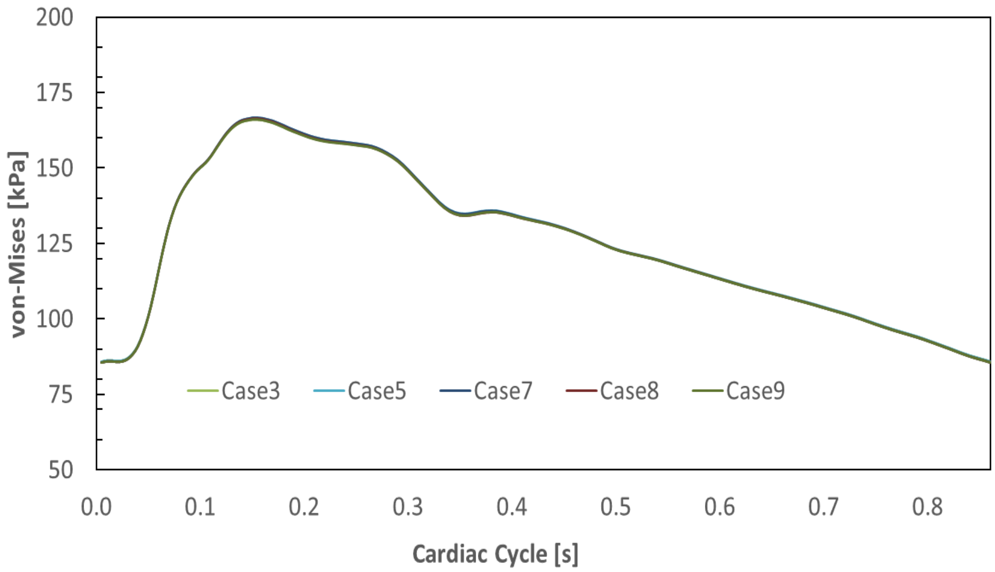

Figure 5.18. Von-Mises stress distribution through the cardiac cycle for selected cases.

5.1.5. Determination of the Proper Turbulence Model

In this study, twelve different turbulence models have been employed and results were compared in terms of hemodynamic risk indicator, velocity characteristics and solid domain parameters. All results are tabulated in Table 5.4 according to their convenient criteria. The results demonstrated that k-epsilon turbulence models with standard wall functions is not a suitable model in terms of hemodynamic indices. Considering the velocity characteristics, Spalart-Allmaras, standard k-omega, SST k-omega and Transitional k-omega with 3 equations have the most sensible results related complex blood flow phenomenon. Furthermore, solid domain parameters such as displacement and von-Mises Stress were revealed to be independent of turbulence modelling. To determine the proper turbulence model literature data was used since Spalart-Allmaras, Standard k-omega, SST k-omega and Transitional k-omega turbulence model was found produce meaningful and acceptable results. Tan et al. have emphasized that transitional k-omega turbulence model gives in closer agreement with magnetic-resonance images [28]. Varghese and Frankel have highlighted that k-omega turbulence model including low Re corrections gives more correct results with experimental measurements than k-epsilon turbulence model family [35]. Based on study of Banks and Breslof [32], Through the recirculation zone in blood flow the transitional k-omega turbulence provides better agreement in comparison with experimental results. All these findings in the literature are consistent with the results of the thesis. SST k-omega with low-Re corrections is determined as preferred turbulence model in all following analyses due to its advantage in both computational time and enabling to capture complex flow structure such as aorta geometry.

Table 5.4. Turbulence model convenient table.

Case	**TurbulenceModel**	**Hemodynamic Risk Indicator**	**Velocity Characteristics**	**Solid Domain Parameters**
Case1	k-epsilon Standard SWT	×	×	✓
Case2	k-epsilon Standard EWT	✓	×	✓
Case3	Spalart-Almaras	✓	✓	✓
Case4	k-epsilon RNG SWT	×	×	✓
Case5	k-epsilon RNG SWT	✓	×	✓
Case6	k-epsilon RNG SWT	×	×	✓
Case7	k-epsilon RNG SWT	✓	×	✓
Case8	Standard k-omega	✓	✓	✓
Case9	SST k-omega	✓	✓	✓
Case10	3 eqn k-omega	✓	✓	✓
Case11	4 eqn k-omega	✓	×	✓
Case12	Reynolds stress	×	×	✓

5.2. Investigations of Solid Domain Parameters

In this section, solid domain parameter effects on hemodynamic characteristics are evaluated by performing numerical analyses. To initial, in accordance with this purpose three different cases were handled which are 5% thickness increased case, nominal case, 5% thickness decreased case. All results parameter mentioned before are tabulated in Table 5.5 From the table it can be observed that there is no remarkable difference for hemodynamic parameter such as OSI, HOLMES and Percentage of OSI ¿0.2. However, the maximum values of both total displacement and equivalent (von-Mises) stress have severely changed. In case 5% thickness decreased case, max displacement is increased by nearly 10% from 1.118 to 1.228 while max von-Mises is risen by about 7% from 166 to 177. In case 5% thickness increased case, max displacement is declined by nearly 3% from 1.118 to 1.083 while max von-Mises decreased by about 5% from 166 to 158. Briefly it can be deduced from results that solid risk parameters are decreases as thickness increased.

Table 5.5. Results of the vessel thickness effects.

	5% decreased	**nominal**	**5% increased**	**10% increased**
OSI	0.1629	0.1626	0.1624	0.1619
HOLMES	0.9536	0.9635	0.9671	0.9671
Percentage of OSI 0.2	39.37	38.71	39.24	39.34
Max Displacement [mm]	1.228	1.118	1.083	0.991
Max Equivalent (von-Mises) Stress [kPa]	177	166	158	149

Beside relation between vessel thickness and solid parameters can be described as third-degree polynomial equation. As it is seen in Table 5.6; when max displacement can be expressed as $-42.969x^3 + 212.11x^2 - 349.38x + 193.13$ where x is the average thickness value of the vessels, maximum error between calculated and estimated values becomes smaller than 0.5%.

Table 5.6. Comparison of the calculated and estimated max displacement value.

	Average thickness	**Calculated max displacement**	**Estimated max displacement**	**Error**
5% decreased	0.1629	0.1626	0.1624	0.08%
nominal	1.6	166.1	165.9	0.09%
5% increased	1.68	158	157.8	0.10%
10% increased	1.76	149	148.8	0.12%

In a similar way, when max stress can be stated as $-1214.2x^3+6048.4x^2-10141x+5881$ the almost perfect match was observed that is tabulated in Table 5.7. Furthermore, effect of the vessel thickness on displacement distribution and stress distribution are shown in Figure 5.19 Figure 5.20 respectively. It can be concluded that there is a reverse relation between vessel thickness and value of solid parameters through cardiac cycle.

Table 5.7. Comparison of the calculated and estimated max stress value.

	Average thickness	**Calculated max stress**	**Estimated max stress**	**Error**
5% decreased	1.52	177	176.9	0.08%
nominal	1.6	166.1	165.9	0.09%
5% increased	1.68	158	157.8	0.10%
10% increased	1.76	149	148.8	0.12%

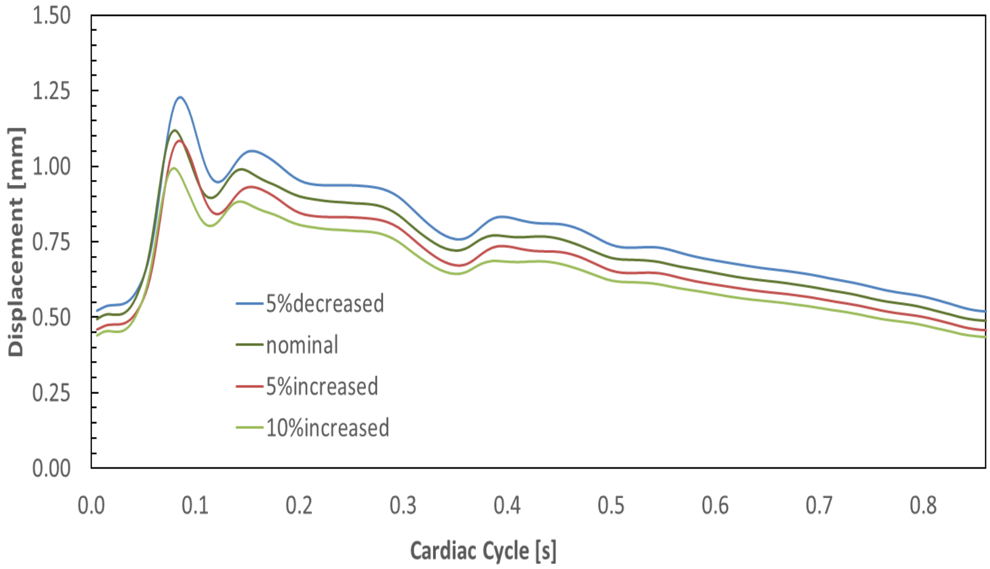

Figure 5.19. Effect of the vessel thickness on displacement distribution.

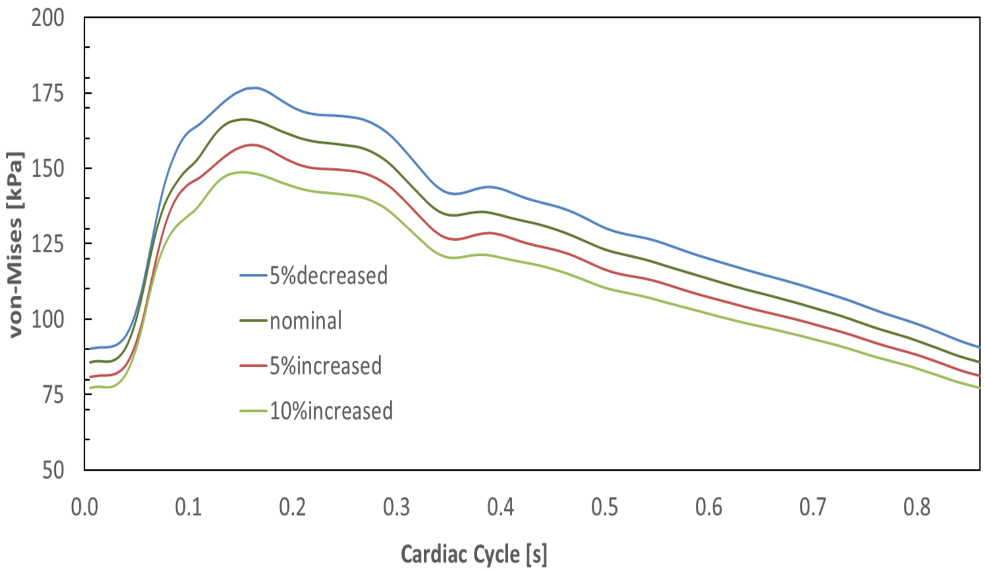

Figure 5.20. Effect of the vessel thickness on stress distribution.

In addition to the vessel thickness modelling effects, different elastic modulus and Poisson's ratio parameters were handled. To evaluate elastic modulus the study of MacSweeey et al. were considered [63]. In this study, 10 young people from 21 to 29 with median age 25, 11 middle-aged people from 41 to 64 with median age 55, and 13 elderly people from 65 to 91 with median age 71.5 years were investigated. The results for Young's modulus illustrated that in the middle-aged controls was more than double that in the younger controls. In the elderly controls was over three times that of the younger controls [63]. In this study, while Young's modulus is chosen as 1 Mpa. To investigate elder and young people this value were given as 1.10 Mpa and 0.95 Mpa, respectively. Furthermore, the different value of Poisson's ratio which is 0.441 were also evaluated while reference value is 0.49 for this study.

The distribution of average OSI value and HOLMES value are shown in Figure 5.21 and Figure 5.22, respectively for each case. It might be concluded that there is no remarkable difference for these indicators among the solid parameters.

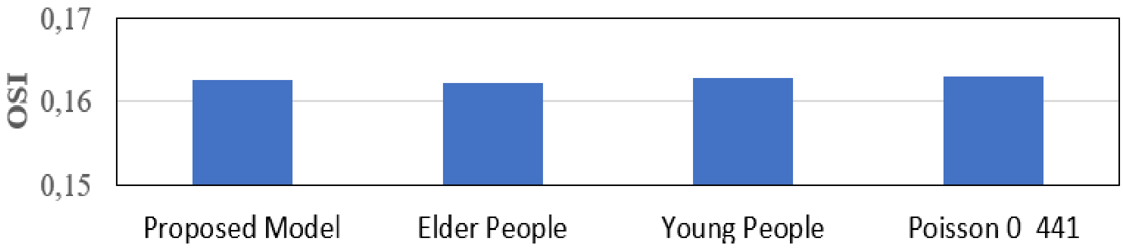

Figure 5.21. Distribution of the average OSI for solid parameters.

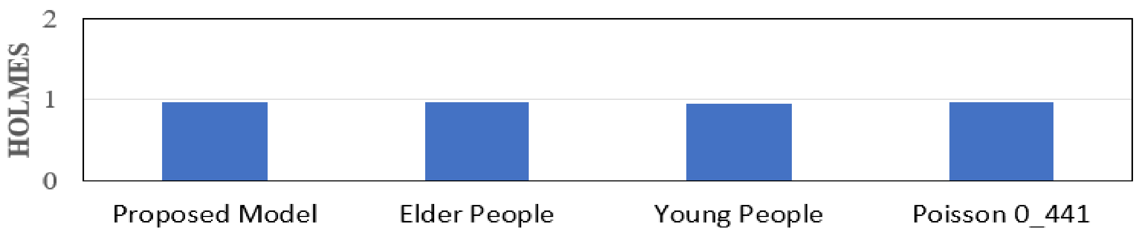

Figure 5.22. Distribution of the average HOLMES for solid parameters.

To compare effect of the solid parameters on the results, comparison of the velocity profile along the Line1, Line2 and Line3 at peak systole are shown in Figure 5.23., Figure 5.24. and Figure 5.25. respectively. All models show similar characteristics for velocity distribution.

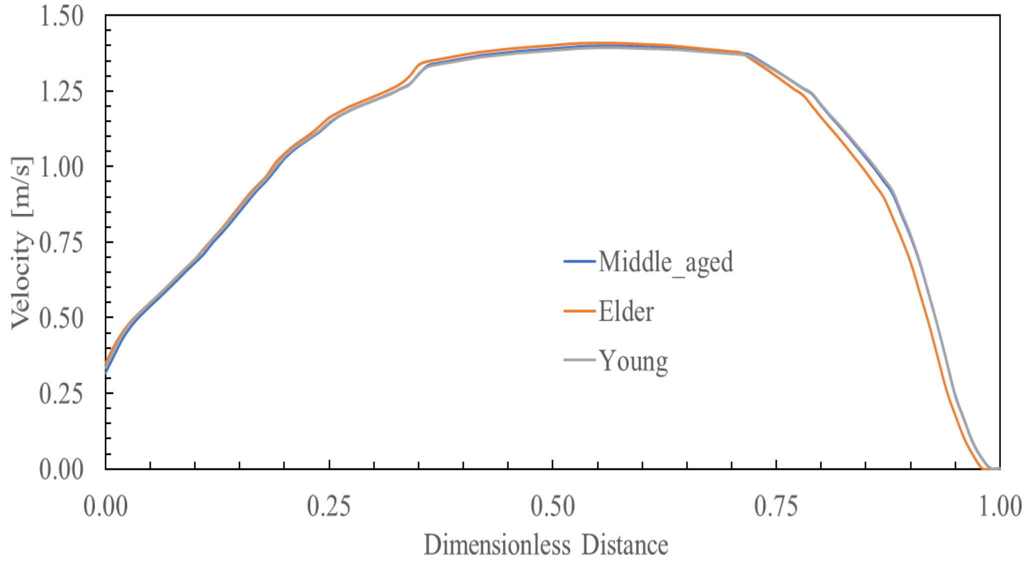

Figure 5.23. Comparison of the velocity-magnitude profile along the Line1 at peak systole for solid domain parameters.

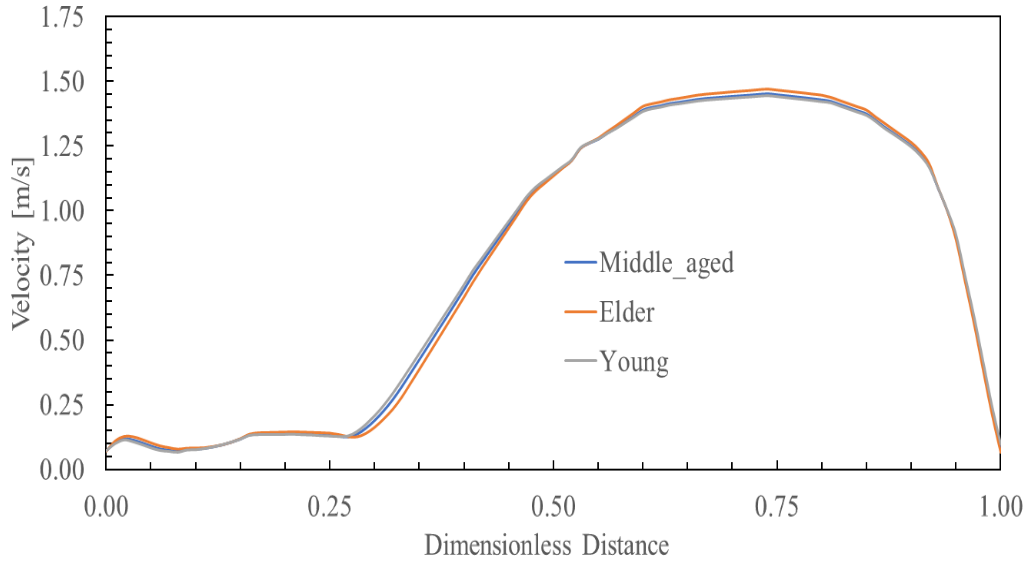

Figure 5.24. Comparison of the velocity-magnitude profile along the Line2 at peak systole for solid domain parameters.

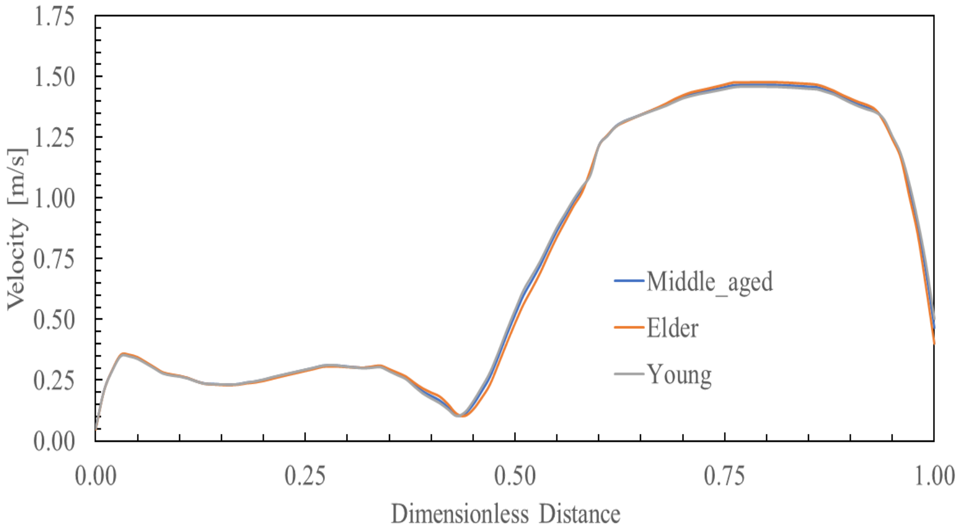

Figure 5.25. Comparison of the velocity-magnitude profile along the Line3 at peak systole for solid domain parameters.

The maximum value of both total displacement and equivalent (von-Mises) stress are calculated and tabulated in Table 5.8. In a similar way both risk indicator and velocity distribution results, middle aged, young, and elder people have similar values in terms of von-Mises Stress. However, max displacement is decreased by nearly 10% from 1.118 to 1.007 for older people, while increased by nearly 6% for young people.

Table 5.8. Comparison of the displacement and Von-Mises stress for solid domain parameters.

Case	**Max Displacement [mm]**	**von-Mises Stress [kPa]**
Proposed Model (middle aged)	1.118	166.090
Elder	1.007	166.220
Young	1.183	166.140

Furthermore, displacement distribution through the cardiac cycle is illustrated in Figure 5.26. As can be seen in graph, max deformation is observed in young people while the lowest deformation value is in elder people with respect to the reference value which belongs to middle aged people.

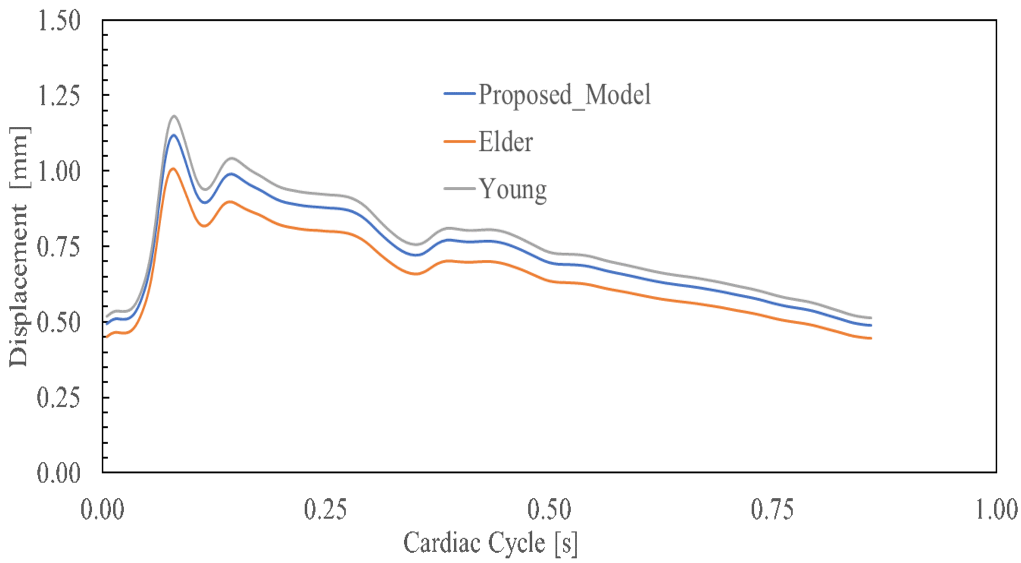

Figure 5.26. Displacement distribution through the cardiac cycle for solid domain parameters.

5.3. Investigations of Viscous Characteristics

In this section, viscous effects on hemodynamic characteristics are evaluated by performing numerical analyses with different models. As mentioned before that blood flow can be modelled as Newtonian fluid in case it flows in tubes which have at least 1 mm diameter. The proposed geometry diameter is greater than 1 mm (20mm). Moreover, the viscosity of blood is approximately constant when rate of shearing strain is greater than 100 s^{-1}. Hence, it is permissible to use a Newtonian material model if it is certain that there are no regions with a small shear rate. The flow in veins and small arteries particularly have a very small shear rate. Because of that, non-Newtonian models are needed. On the other hand, Newtonian assumption is quite adequate for large arteries. Therefore, remarkable difference is not expected between the Newtonian and Non-Newtonian cases. To observe this situation two different Non-Newtonian models which are Power Law and Carreau have been handled. Characteristics of these models were given in Figure 5.27 [64].

Non-Newtonian Power Law	
Consistency Index [kg-s^n-2/m]	0.0148
Power-Law Index	0.775
Minimum Viscosity Limit [kg/m-s)	0.056
Maximum Viscosity Limit [kg/m-s)	0.00345
Non-Newtonian Carreau	
Time constant, Lambda [s]	3.313
Power-Law Index	0.3568
Zero Shear Viscosity [kg/m-s)	0.056
Infinite Shear Viscosity [kg/m-s)	0.00345

Figure 5.27. Rheological models for blood, with constant density.

The distribution of average OSI value and HOLMES value are shown in Figure 5.28 and Figure 5.29, respectively for each case. The slight differences are observed between cases as expected. However, Non-Newtonian Power Law model underestimated OSI value by up to about 6% compared to other cases while overestimated the HOLMES value about higher than five times compared with other studies. It can be concluded that Power Law does not behave well for these models.

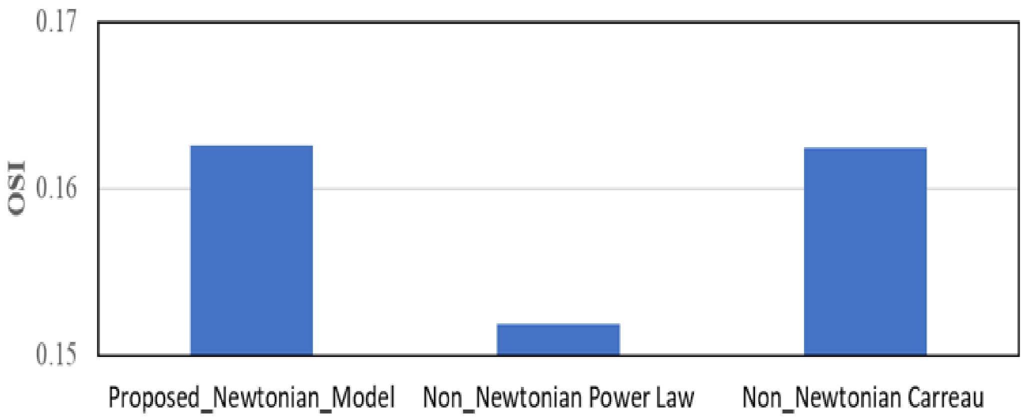

Figure 5.28. Distribution of the average OSI for viscous characteristics.

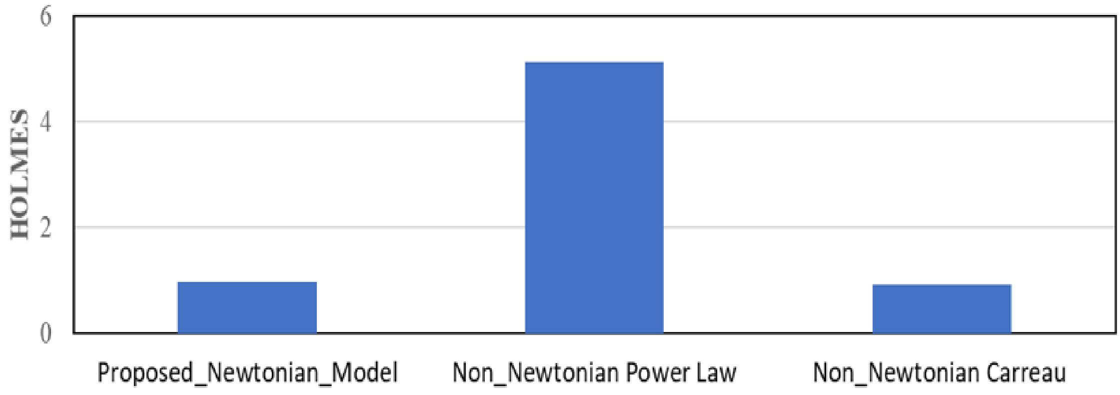

Figure 5.29. Distribution of the average HOLMES for viscous characteristics.

To compare effect of the viscous modelling on the results, comparison of the velocity profile along the Line1, Line2 and Line3 at peak systole are shown in Figure 5.30, Figure 5.31, and Figure 5.32 respectively. Non-Newtonian Power Law model represents different characteristics according to Newtonian and Carreau model for each velocity distribution. However, Newtonain model and Non-Newtonian Carreau model shows similar behaviour.

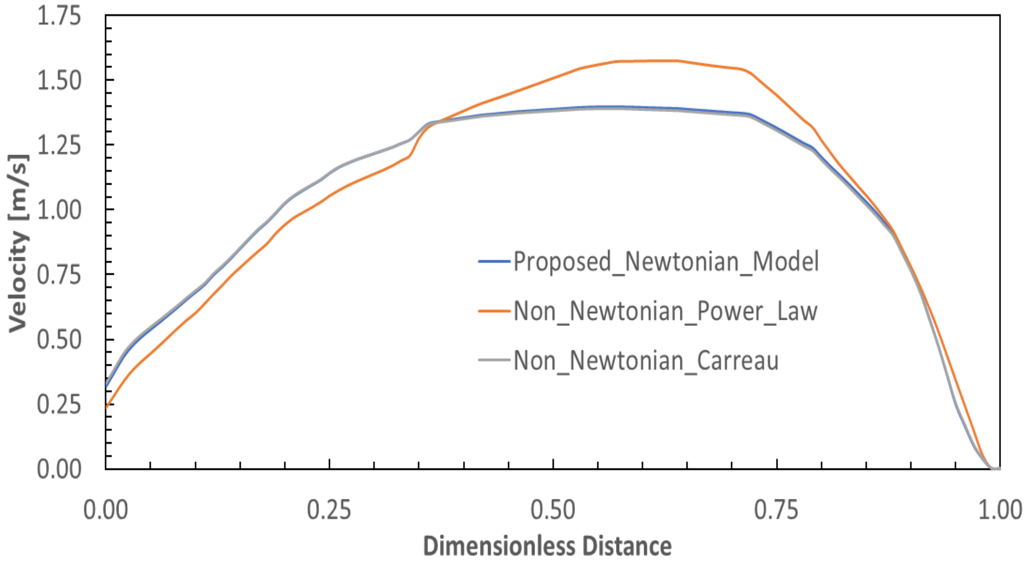

Figure 5.30. Comparison of the velocity-magnitude profile along the Line1 at peak systole for viscous effects.

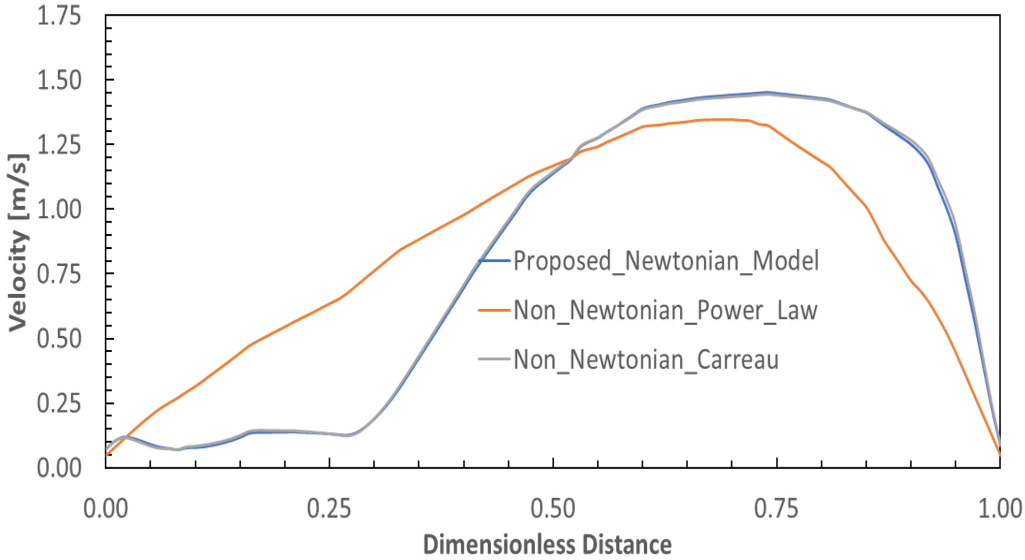

Figure 5.31. Comparison of the velocity-magnitude profile along the Line2 at peak systole for viscous effects.

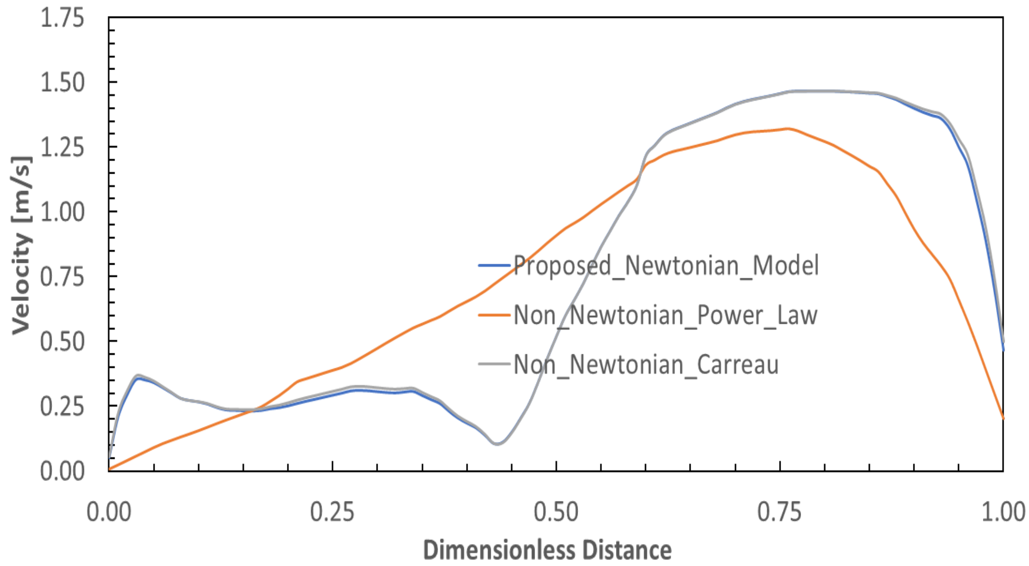

Figure 5.32. Comparison of the velocity-magnitude profile along the Line3 at peak systole for viscous effects.

The maximum value of both total displacement and equivalent (von-Mises) stress are calculated and tabulated in Table 5.9 In a similar way both risk indicator and velocity distribution results, Newtonian and Non-Newtonian Carreau model have similar values in terms of solid domain parameters. However, Non-Newtonian Power Law model overestimates both max displacement and von-Mises stress as ≈5% and ≈6% respectively.

Table 5.9. Comparison of the displacement and Von-Mises stress for viscous effects.

Case	**Max Displacement [mm]**	**von-Mises Stress [kPa]**
Proposed Newtonian Model)	1.118	166.090
Non Newtonian Power Law	1.192	175.500
Non Newtonian Carreau Law	1.117	165.990

Furthermore, displacement and von-Mises stress distribution through the cardiac cycle are illustrated in Figure 5.33, and Figure 5.34, respectively. Almost perfect match was observed between Newtonian and Carreau Model, while Non-Newtonian Power Law model shown different trend.

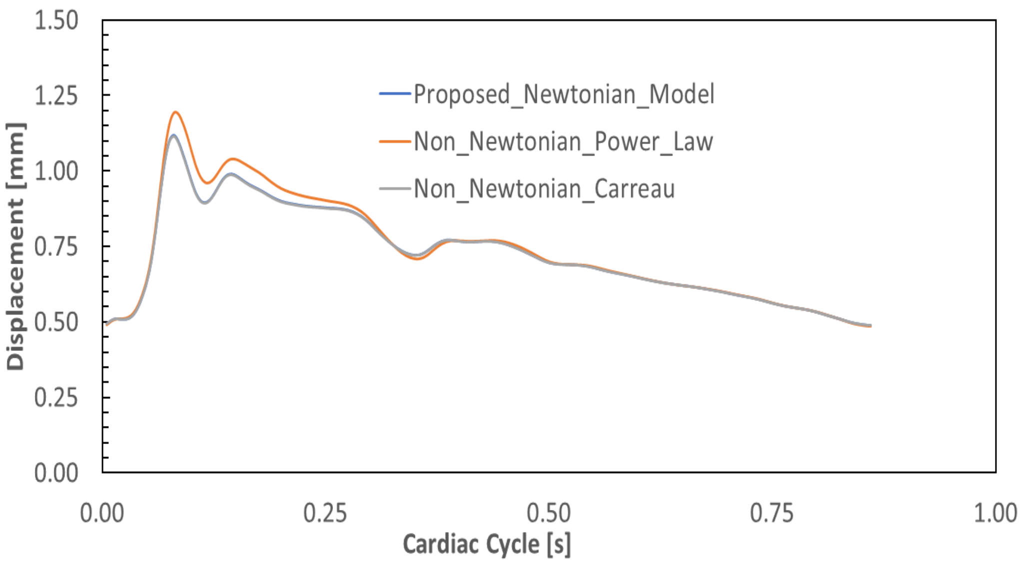

Figure 5.33. Displacement distribution through the cardiac cycle for viscous effects.

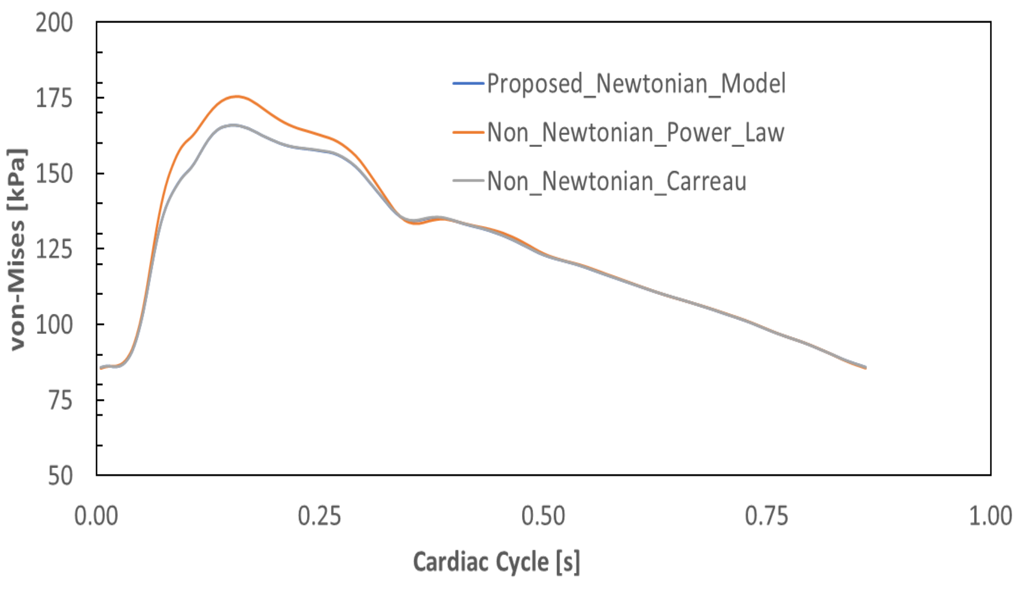

Figure 5.34. Von-Mises stress distribution through the cardiac cycle for viscous effects.

6. CONCLUSION

There is a great focus on numerical simulations in biomedical research especially, studying the blood flow in the cardiovascular system to evaluate understanding the hemodynamic phenomena of blood. In line with this objective, CFD application in biomedical is one of the promising research topics with the purpose of the diagnosing and treating the diseases. The main objective of this thesis is to express the differences in blood blow and vessel wall characteristics including hemodynamic risk indicators in case of different numerical aspects are used in combination for the analyses. Therefore, the effects of using different numerical modelling parameter on turbulent pulsatile blood flow through the idealised aorta geometry and boundary conditions are investigated.

In the first part of the thesis results, turbulence modelling effects on aorta numerical modelling are investigated. Blood can be assumed as Newtonian whereas its vessels are modelled as elastic walls.Twelve different turbulence models consisting mostly of models from k-epsilon and k-omega groups are considered. It is shown in the presented results that a remarkable difference exists in different turbulent models especially for hemodynamic parameters and velocity characteristics. OSI values are underestimated by up to about 5% in case of k-epsilon turbulence models including standard wall treatment. For both OSI threshold value and HOLMES indicators just six models among twelve turbulence models shows similar behaviour. Furthermore, several recirculation regions especially in left subclavian artery are captured. Comparing the results, the velocity distribution from ascending to descending aorta at peak systole are similar for all cases. However, it is seen that remarkable differences occur between turbulence models for flow pattern in three artery routes, which are brachiocephalic artery, left common carotid artery and left subclavian artery. Even the difference between location of vortices can be reached up to %26 according to turbulence models. The results of the solid parameters show that turbulence model does not affect considerably on numerical modelling of blood flow in terms of maximum value of the both displacement and von-Mises stress. Taking into account all the results and literature data, SST k-omega with low-Re corrections has been determined as recommended turbulence model.

In the second part of thesis results, solid domain parameters effects on aorta numerical modelling are investigated by using different values. Comparing the results of both hemodynamic parameter such as OSI, HOLMES and Percentage of OSI ¿ 0.2 and velocity characteristics it is found that negligible difference occurs nominal, decreased and increased thickness cases for vessel thickness effect. On the other side, the results show that when thickness of vessel is increased both displacement and stress characteristics is decreased. In fact, this reverse relation can be converted to the polynomial equation. The obtained equations give results with an error of less than 0.5% for maximum value of both displacement and stress.Furthermore two different elastic modulus which which represent elder and young people are evaluated. It might be concluded that there is no remarkable difference for both risk indicators and velocity characteristics among the solid parameters. On the other hand, differences in maximum deformation are observed between young and older people.

In the last of thesis results, two different Non-Newtonian models which are Power Law and Carreau have been handled. Power Law model demonstrates different characteristics while Newtonain model and Non-Newtonian Carreau model shows similar behaviour in terms of risk indicator and velocity distributions. In a similar way, almost perfect match was observed between Newtonian and Carreau Model, while Non-Newtonian Power Law model was shown different trend for displacement and von-Mises stress distribution through the cardiac cycle.

REFERENCES

1. Waite, L. and J. Fine, *Applied Biofluid Mechanics*, The McGraw-Hill, New York, 2007.

2. Bilgi, C., *Numerical Investigation of Blood Rheology and Vessel Elasticity Effects on Hemodynamics in Arteries with Aneurysm*, M.S. thesis, Boğaziçi University, 2016.

3. Afkari, D., *Pulsatile Blood Flow Interaction with Arterial Walls of Aorta: Autoregulation and Impedance Pressure Boundary Condition and Its Biomedical Applications*, Ph.D. Thesis, Universidad Politécnica de Madrid, 2015.

4. Kimball, J., *Biology*, Tufts University and Harvard University, Boston & Cambridge, 2019.

5. Organization, W. H., *Prevention of Cardiovascular Disease: Guidelines for Assessment and Management of Cardiovascular Risk*, Geneva, 2007.

6. Organization, W. H., *Hearts: Technical Package for Cardiovascular Disease Management in Primary Health Care*, Geneva, 2016.

7. Wilkins, E., L. Wilson, K. Wickramasinghe, P. Bhatnagar, J. Leal, R. Luengo-Fernandez, R.and Burns, M. Rayner and N. Townsend, *European Cardiovascular Disease Statistics 2017*, Brussels, 2017.

8. Virani, S., A. Alonso, H. Aparicio, E. Benjamin, M. Bittencourt, C. Callaway, A. Carson, A. Chamberlain, S. Cheng, F. Delling, M. Elkind, K. Evenson, J. Ferguson, D. Gupta, S. Khan, S. Kissela, K. Knutson, C. Lee, T. Lewis, J. Liu, M. Loop and P. Lutsey, *European Cardiovascular Disease Statistics 2017*, Dallas, 2017.

9. Morris, P. D., A. Narracott, H. Tengg-Kobligk, D. A. S. Soto, S. Hsiao, A. Lungu, P. Evans, N. W. Bressloff, P. V. Lawford, D. R. Hose and J. P. Gunn, "Computational Fluid Dynamics Modelling in Cardiovascular Medicine", *Heart*, Vol. 102, pp. 18–28, 2015.

10. Bazilevs, Y., K. Takizawau and T. E. Tezduyar, *Computational Fluid–Structure Interaction Methods and Applications*, John Wiley & Sons Ltd, West Sussex, 2013.

11. Jensen, J. A., *Estimation of Blood Velocities Using Ultrasound with A Signal Processing Approach*, Cambridge University Press, United Kingdom, 1996.

12. Perktold, K., R. O. Peter, M. Resch and G. Langs, "Pulsatile Non-Newtonian Blood Flow in Three-Dimensional Carotid Bifurcation Models: A Numerical Study of Flow Phenomena Under Different Bifurcation Angles", *Journal of Biomedical Engineering*, Vol. 13, pp. 507–515, 1991.

13. Budwig, R., D. Elger, H. Hooper and J. Slippy, "Steady Flow in Abdominal Aortic Aneurysm Models", *Journal of Biomechanical Engineering*, Vol. 115, pp. 418–23, 1992.

14. Taylor, C. A., T. J. Hughes and C. K. Zarins, "Finite Element Modeling of Three-Dimensional Pulsatile Flow in The Abdominal Aorta: Relevance To Atherosclerosis", *Annals of Biomedical Engineering*, Vol. 26, pp. 975–87, 1998.

15. Vlachopoulos, C., M. O'Rourke and W. W. Nichols, *McDonald's Blood Flow in Arteries Theoretical, Experimental and Clinical Principles*, CRC Press London, 2012.

16. Leuprecht, A., S. Kozerke, P. Boesiger and K. Perktold, "Blood Flow in The Human Ascending Aorta: A Combined MRI and CFD Study", *Journal of Engineering Mathematics*, Vol. 47, pp. 387–404, 2003.

17. Scotti, C. and E. A. Finol, "Compliant Biomechanics of Abdominal Aortic

Aneurysms: A Fluid-Structure Interaction Study", *Computers and Structures*, Vol. 85, pp. 1097–1113, 2003.

18. Shahcheraghi, N., H. A. Dwyer, C. A.Y., A. Barakat and T. Rutaganira, "Unsteady and Three-Dimensional Simulation of Blood Flow in the Human Aortic Arch", *Journal of Biomechanical Engineering*, Vol. 124, pp. 378–87, 2002.

19. Tokuda, Y., M. Song, U. Y., A. Usui, T. Akita, S. Yoneyama and S. Maruyama, "Three-Dimensional Numerical Simulation of Blood Flow in The Aortic Arch During Cardiopulmonary Bypass", *European Journal of Cardio-thoracic Surgery : Official Journal of the European Association for Cardio-thoracic Surgery*, Vol. 33, pp. 164–7, 2008.

20. Zhao, S. Z., X. Y. Xu, H. A. D., S. A. Thom, A. V. Stanton, B. Ariff and Q. Long, "Blood Flow and Vessel Mechanics in A Physiologically Realistic Model of A Human Carotid Arterial Bifurcation", *Journal of Biomechanics*, Vol. 33, pp. 975–984, 2000.

21. Gerbeau, J. F., M. Vidrascu and F. P., "Fluid-Structure Interaction in Blood Flows on Geometries Coming From Medical Imaging", *Computers Structures*, Vol. 83, pp. 155–165, 2005.

22. Gao, F., Z. Guo, M. Sakamoto and T. Matsuzawa, "Fluid-Structure Interaction within a Layered Aortic Arch Model", *Journal of Biological Physics*, Vol. 32, pp. 435–54, 2006.

23. LI, Z. and C. Kleinstreuer, "Effects of Blood Flow and Vessel Geometry on Wall Stress and Rupture Risk of Abdominal Aortic Aneurysms", *Journal of Medical Engineering Technology*, Vol. 30, pp. 282–297, 2006.

24. Khanafer, K. M., J. L. Bull and R. Berguer, "Fluid–Structure Interaction of Turbulent Pulsatile Flow Within A Flexible Wall Axisymmetric Aortic Aneurysm Model", *European Journal of Mechanics - B/Fluids*, Vol. 28, pp. 88–102, 2009.

25. McGurk, K. A., B. Owen, W. D. Watson, H. J. F. M. Nethononda, R. M.and Cordell and H. R. A. K. B. D. Rider, O. J.and Watkins, "Heritability of haemodynamics in the ascending aorta", *Scientific Reports*, Vol. 10, pp. 143–153, 2020.

26. Reynolds, O., "On The Dynamical Theory of Incompressible Viscous Fluids and the Determination of The Criterion", *The Royal Society*, Vol. 56, pp. 40–45, 1894.

27. Khanafer, K. M., J. L. Bull, U. G. R. and R. Berguer, "Turbulence Significantly Increases Pressure and Fluid Shear Stress in An Aortic Aneurysm Model Under Resting and Exercise Flow Conditions", *Annals of Vascular Surgery*, Vol. 21, pp. 67–74, 2007.

28. Tan, F. P. P., A. Borghi, M. R. H., N. B. Wood, S. Thom and X. Y. Xu, "Analysis of Flow Patterns in A Patient-Specific Thoracic Aortic Aneurysm Model", *Computers and Structures*, Vol. 87, pp. 680–690, 2009.

29. Liao, W., T. S. Lee and H. T. Low, "Numerical Studies of Physiological Pulsatile Flow Through Constricted Tube", *International Journal of Numerical Methods for Heat Fluid Flow*, Vol. 14, pp. 689–713, 2004.

30. Mittal, R. C., S. P. Simmons and H. S. Udaykumar, "Application of Large-Eddy Simulation To The Study Of Pulsatile Flow in A Modeled Arterial Stenosis", *Journal of Biomechanical Engineering*, Vol. 123, pp. 325–32, 2001.

31. Ahmed, S. A. and D. P. Giddens, "Pulsatile Poststenotic Flow Studies With Laser Doppler Anemometry", *Journal of Biomechanical Engineering*, Vol. 17, pp. 695–705, 1984.

32. Banks, J. A. and N. W. Bressloff, "Turbulence Modeling in Three-Dimensional Stenosed Arterial Bifurcationsy", *Journal of Biomechanical Engineering*, Vol. 129, pp. 40–50, 2007.

33. Jahangiri, M., M. Saghafian and M. R. Sadeghi, "Numerical Study of Turbulent Pulsatile Blood Flow through Stenosed Artery Using Fluid-Solid Interaction", *Computational and Mathematical Methods in Medicine*, Vol. 2015, pp. 515–525, 2015.

34. Ryval, J., A. G. Straatman and D. A. Steinman, "Two-Equation Turbulence Modeling of Pulsatile Flow in A Stenosed Tube", *Journal of Biomechanical Engineering*, Vol. 126, pp. 625–35, 2004.

35. Varghese, S. and S. H. Frankel, "Numerical Modeling of Pulsatile Turbulent Flow in Stenotic Vessels", *Journal of Biomechanical Engineering*, Vol. 125, pp. 445–60, 2003.

36. Xiao, B. and Y. Zhang, "Numerical Simulation of Pulsatile Turbulent Flow in Tapering Stenosed Arteries", *Journal of Biomechanical Engineering*, Vol. 19, pp. 561–573, 2009.

37. Conti, M., C. Long, M. Marconi, R. Berchiolli, Y. Bazilevs and a. Reali, "Carotid Artery Hemodynamics Before and After Stenting: A Patient Specific CFD Study", *Computers and Fluids*, Vol. 141, pp. 62–74, 2016.

38. Mendez, V., M. D. Giuseppe and S. Pasta, "Comparison of Hemodynamic and Structural Indices of Ascending Thoracic Aortic Aneurysm as Predicted By 2-Way FSI, CFD Rigid Wall Simulation and Patient-Specific Displacement-Based FEA", *Computers in Biology and Medicine*, Vol. 100, pp. 221–229, 2018.

39. Martino, E. S. D., G. Guadagni, A. Fumero, G. Ballerini, R. Spirito, P. Biglioli and A. Redaelli, "Fluid–structure Interaction within Realistic Three-dimensional Models of the Aneurysmatic Aorta as a Guidance to Assess the Risk of Rupture of the Aneurysm", *Medical Engineering Physics*, Vol. 23, p. 647–655, 2001.

40. Khanafer, K. M., P. Gadhoke, R. Berguer and J. L. Bull, "Modeling Pulsatile Flow in Aortic Aneurysms: Effect of Non-Newtonian Properties of Blood", *Biorheologys*,

Vol. 43, pp. 661–679, 2006.

41. Stewart, S., E. Paterson, G. Burgreen, P. Hariharan, M. Giarra, V. Reddy, S. Day, K. Manning, S. Deutsch, M. Berman, M. Myers and R. Malinauskas, "Assessment of CFD Performance in Simulations of an Idealized Medical Device: Results of FDA's First Computational Interlaboratory Study", *Cardiovascular Engineering and Technology*, Vol. 3, pp. 139–160, 2012.

42. Landau, L. D. and E. M. Lifshitz, *Fluid Mechanics*, Elsevier, Oxford, 1987.

43. Ansys, *Ansys Fluent Theory Guide, Release 2021 R2*, Ansys Drive, Canonsburg, 2021.

44. Hart, J., "Comparison of Turbulence Modeling Approaches to the Simulation of a Dimpled Sphere", *Procedia Engineering*, Vol. 147, pp. 68–73, 2016.

45. Standring, S., *Gray's Anatomy The Anatomical Basis of Clinical Practice*, Elsevier, London, 2016.

46. Crosetto, P., P. Reymond, S. Deparis, D. Kontaxakis, N. Stergiopulos and A. Quarteroni, "Fluid–structure Interaction Simulation of Aortic Blood Flow", *Computers Fluids*, Vol. 43, pp. 46–57, 2011.

47. Afkari, D. and F. Gabaldón, "Fluid-Solid Interaction in Arteries Incorporating The Autoregulation Concept in Boundary Conditions", *Computer Methods in Biomechanics and Biomedical Engineerings*, Vol. 19, pp. 985–1001, 2015.

48. Burnett, B., *Coupled Fluid-Structure Interaction Modeling of a Parafoil*, M.S. thesis, Embry-Riddle Aeronautical University, 2016.

49. Khader, S. M. A., N. Kumar and R. Pai, *Fluid Structure Interaction Study of Stenosed Carotid Artery Considering the Effects of Blood Pressure and Altered Gravity, Finite Element Methods and Their Applications, Mahboub Baccouch*, Manipal Institute of Technology, Manipal, 2020.

50. Kruchten, T. V., *CFD Modeling of Abdominal Aortic Aneurysms*, M.S. thesis, Delft University of Technology, 2015.

51. Karnam, Y., *Multiscale Fluid-Structure Interaction Models Development and Applications to the 3D Elements of a Human Cardiovascular System*, M.S. thesis, Rochester Institute of Technology, 2019.

52. Versteeg, H. K. and W. Malalasekera, *An introduction to Computational Fluid Dynamics*, Addison Wesley Longman, London, 1995.

53. Rapp, B. A., *Microfluidics: Modeling, Mechanics, And Mathematics*, Elsevier, Oxford, 2017.

54. Akgül, M., *Static Aeroelastic Analysis Of A Generic Slender Missile Using A Loosely Coupled Fluid Structure Interaction Method*, M.S. thesis, Middle East Technical University, 2012.

55. Ansys, *Ansys Mechanical Element Reference, Release 2021 R2*, Ansys Drive, Canonsburg, 2021.

56. Ansys, *Ansys Mechanical Theory Reference, Release 2021 R2*, Ansys Drive, Canonsburg, 2021.

57. Guess, W. P., B. D. Reddy, A. McBride, B. Spottiswoode, J. Downs and T. Franz, "Fluid-Structure Interaction Modelling And Stabilisation Of A Patient-Specific Arteriovenous Access Fistula", *Biorheologys*, pp. 479–497, 2017.

58. Deep, D., *A Study of Blood Flow in Normal and Diseased Aorta*, M.S. thesis, Purdue University, 2013.

59. Celik, I., U. Ghia, P. Roache, C. Freitas, H. Coloman and P. Raad, "Procedure of Estimation and Reporting of Uncertainty Due to Discretization in CFD Applications", *Journal of Fluids Engineering*, Vol. 130, p. 078001, 2008.

60. Bilgi, C. and K. Atalik, “Vascular Remodelling Relates to an Elevated Oscillatory Shear Index and Relative Residence Time in Spontaneously Hypertensive Rats”, *Biorheology*, Vol. 56, pp. 51–71, 2019.

61. Pirola, S., D. O’Regan, O. A. Jarral and G. Asimakopoulos, “Computational Study of Aortic Hemodynamics for Patients With an Abnormal Aortic Valve: The Importance of Secondary Flow at The Ascending Aorta Inlet”, *APL Bioengineering*, Vol. 2, pp. 647–655, 2018.

62. Chen, Z., H. Yu, Y. Shi, M. Zhu, Y. Wang, X. Hu, Y. Zhang, Y. Chang, M. Xu and W. Gao, “Vascular Remodelling Relates to an Elevated Oscillatory Shear Index and Relative Residence Time in Spontaneously Hypertensive Rats”, *Scientific Reports*, Vol. 7, 2007.

63. MacSweeney, S. T. R., G. Young, R. M. Greenhalgh and J. T. Powell, “Mechanical Properties of The Aneurysmal Aorta”, *Surgical Research Society*, Vol. 79, pp. 1281–1284, 1992.

64. Caballero, A. D. and S. Lain, “Numerical Simulation of Non-Newtonian Blood Flow Dynamics in Human Thoracic Aorta”, *Computer Methods in Biomechanics and Biomedical Engineering*, Vol. 18, 2014.

APPENDIX A: PERMISSIONS FOR REUSE

Applied Biofluid Mechanics

Lee Waite, Ph.D., P.E.
Jerry Fine, Ph.D.

TERMS OF USE

Figure A.1. Permission for reuse of Figure 1.1. and Figure 1.8.

John W. Kimball
Tufts University & Harvard

This text is disseminated via the Open Education Resource (OER) LibreTexts Project (https://LibreTexts.org) and like the hundreds of other texts available within this powerful platform, it is freely available for reading, printing and "consuming." Most, but not all, pages in the library have licenses that may allow individuals to make changes, save, and print this book. Carefully consult the applicable license(s) before pursuing such effects.

Instructors can adopt existing LibreTexts texts or Remix them to quickly build course-specific resources to meet the needs of their students. Unlike traditional textbooks, LibreTexts' web based origins allow powerful integration of advanced features and new technologies to support learning.

Figure A.2. Permission for reuse of Figure 1.2.

Re: Letter for permission
Gönderen **Coşkun Bilgi** Tarih **2022-11-21 00:04**

Hello Ahmet,

Of course! You can reproduce any image/table from my Master's thesis.

Best,
Coskun Bilgi

Figure A.3. Permission for reuse of Figure 1.6. and Figure 1.7.

Re: Letter for permission
Gönderen **damon afkari** Tarih **2022-11-20 14:23**

Hi Ahmet,

Thanks for your interest in my thesis. There is no problem using the images in your thesis. But please consider that except the first image, the rest of the images are taken form other references and I think I have mentioned them in the thesis. The second image is a general anatomy of the heart which you can find from other sources even with better quality, in case of that you don`t know the exact original source. And for the third image, it is a combination of all models done by several references whose works are mentioned in the thesis.

Good luck and let me have a copy of your final work! I travel frequently to Istanbul and we may meet someday.

Regards,
Damon

Figure A.4. Permission for reuse of Figure 2.1., Figure 2.2. and Figure 2.3.